Gas Tightness Measurements for CBM-TRD Modules

Master's Thesis in Physics

Institut für Kernphysik
WWU Münster

Ruben Weber

supervised by

Anton Andronic

and

Christian Klein-Bösing

January 4, 2023

First referee: Prof. Dr. Anton Andronic

Second referee: Apl. Prof. Dr. Christian Klein-Bösing

Contents

1 Preface – Erratum

The first version of this thesis had an error in the random number based volume determination method described in section 3.12.

The error lead to significant changes in measurement results and was discovered by me shortly after the submission of the thesis. An erratum was issued, correcting the faulty passages of the thesis.

In this version, these errors are already fixed. However, the passages and values where changes had to be made are highlighted in red. Graphics, where the error lead to a change are superseded by corrected versions. This is noted in the captions of the affected figures.

2 Introduction

Quark Gluon Plasma (QGP) is a state of matter believed to have been present in the early universe, fractions of seconds after the big bang [Dem14, p.393, Abb.12.11]. In that state quarks are not confined within hadrons but instead are able to move freely in the high temperature and density regime of the QGP [Pov+14, p.390].

High energy collisions are generated at accelerator facilities and studied using the data obtained, to learn about this state. One of these facilities is the *Facility for Antiproton and Ion Research* (FAIR) in Darmstadt, currently under construction. The *Compressed Baryonic Matter* (CBM) experiment is located at this accelerator complex and investigates, among other things, the *Quantum Chromodynamics* (QCD) phase diagram at high net baryon densities and the transition into QGP [Heu09, sec.1].

Multiple detectors are used to characterize the particles produced in the collisions. One of these detectors is the Transition Radiation Detector (TRD).

The TRD is a Multi Wire Proportional Chamber (MWPC) based detector. Series production of these MWPCs is imminent as of the writing of this thesis.

Operation of the detector is dependent on an accurate gas mixture in the MWPCs. The gas used in the detector is a mixture of Xenon and Carbon dioxide. The need for a well-defined gas composition and the high cost of Xenon make the gas tightness of the constructed MWPCs essential for the success of the TRD.

In this thesis project, said gas tightness is investigated for a prototype constructed in 2016. This prototype shares production procedures with the final module. Leakages in this prototype therefore reflect on deficits in the building process relevant for series production. Adjustments to the construction process of the modules can be made based on the findings for this prototype.

A setup for overpressure decay measurements is designed, commissioned and characterized. Leakages are located.

Based on these findings, adjustments to the production procedure are made.

3 Background Information

3.1 The CBM Experiment
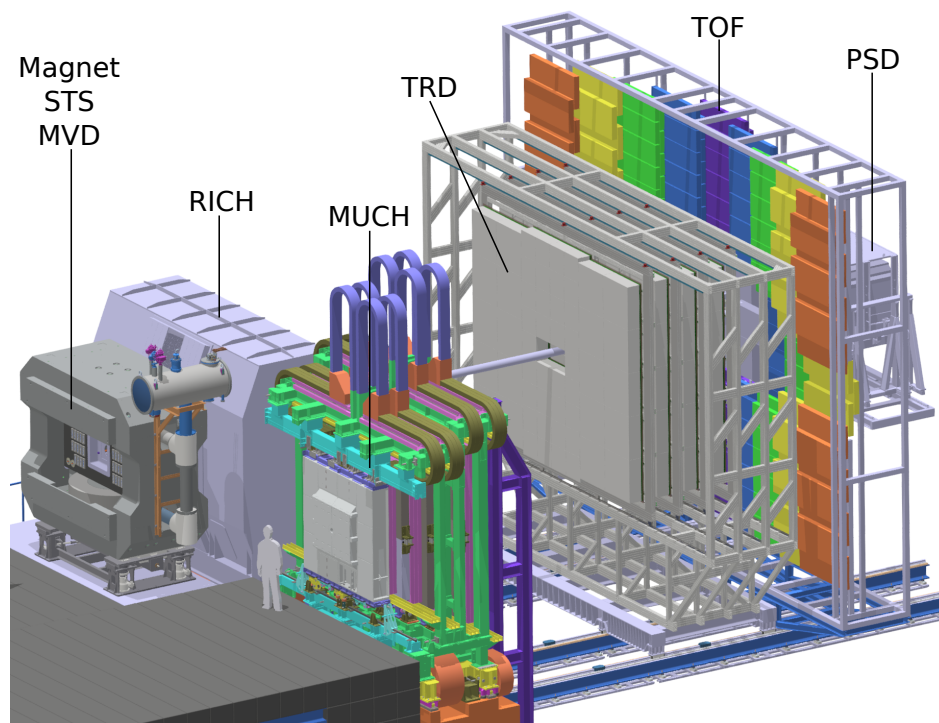
Figure 3.1: A render of the CBM experiment with labeled subdetectors. Beam direction is from left to right.

The CBM experiment is a high rate heavy ion experiment in fixed-target geometry. It is currently under construction at the FAIR at *GSI Helmholtzzentrum für Schwerionenforschung* (GSI).

The goal of this experiment is to explore hot and dense QCD matter, in particular the transition of this matter into a state called QGP. The exploration of the QGP includes the sampling of rare probes, the measurement of statistically significant amounts of which requires a lot of data. To acquire significant amounts of data in reasonable

time, the CBM experiment is operated at high interaction rates. Therefore, each detector of the CBM experiment is designed to measure particles created at event rates of up to 10 MHz at beam energies of up to 29 GeV for protons, up to 11 AGeV for Au and up to 14 AGeV for nuclei with $Z/A = 0.5$ [BBE18, p.11, sec.1.4].

Starting at the target, the detectors of the CBM experiment, shown in fig. 3.1, are [BBE18, p.12f.]:

The **Micro-Vertex Detector (MVD)** is a low material budget, high position resolution monolithic active pixel sensor 5 cm to 20 cm downstream of the target inside the vacuum. It resolves the position of secondary vertices with an accuracy of 50 µm to 100 µm along the beam axis.

The **Silicon Tracking System (STS)** is the main tracking detector for charged particles, providing track and momentum information, the latter with a resolution of about $\Delta p/p = 1.5\,\%$. This silicon strip detector is located 30 cm to 100 cm downstream of the target.

The **Ring Imaging Cherenkov Detector (RICH)** allows electron identification using Cherenkov radiation, directed by arrays of mirrors and detected by photon detectors. It is set up 1.6 m downstream of the target.

The **Muon Chamber System (MUCH)** tracks particles through a hadron absorber, performing a momentum dependent muon identification using the data obtained. The RICH and the MUCH are interchangeable, depending on the current CBM setup.

The **TRD** is discussed in detail in section 3.2 and section 3.7. It consists of four layers, each consisting of Transition Radiation (TR) radiators and MWPCs. It provides tracking and pion suppression capabilities at higher particle momenta.

The **Time-of-Flight System (TOF)** identifies hadrons using its exceptional time resolution of 80 ps, by combining the obtained velocity-data with the momentum determined by the STS.

The **Projectile Spectator Detector (PSD)** is a lead-scintillator calorimeter with a uniform energy resolution. It measures the non-interacting nucleons to determine the collision centrality.

All of these detectors are connected to an online event selection system, integrated into the data acquisition system.

3.2 General Structure of the CBM-TRD
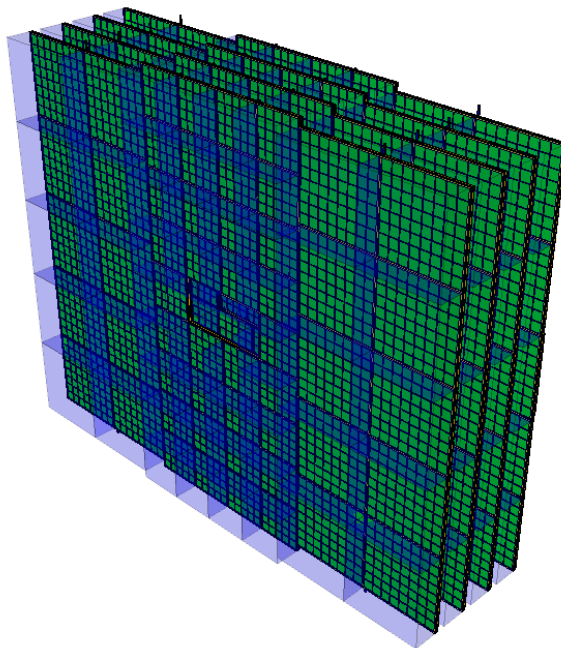
Figure 3.2: A rendering of the TRD, as implemented in a software framework [BBE18, p.36, fig.4.2]. The blue transparent boxes are radiators, the green layers represent the MWPCs.

The CBM-TRD targets a pion suppression of about 20 at an electron efficiency of 90 % [BBE18, p.16, sec.2.2]. Interaction rates of up to 10 MHz with an average hit rate of 100 kHz per pad must be processed by the detector. Further requirements for the design include an energy loss resolution better than 30 % above $p = 1\,\mathrm{GeV}/c$, with a position resolution of about 300 µm, specified in [BBE18, p.16ff., sec.2.2].

The detector wall of 6.3 m width and 5.1 m height will consist of four layers and is shown in fig. 3.2. The layers themselves are composed of 54 MWPC detector modules. Each module consists of the MWPC and the radiator. They are of two different sizes and four different types, which are described in section 3.7.

3.3 Interaction of Particles with Matter

Since the interaction of particles with matter is of key interest in detector physics, the interactions relevant for the TRD are briefly summed up in the following subsections.

3.3.1 Heavy Charged Particles

The interactions of heavy charged particles, referring here to everything heavier than an electron, is momentum dependent. For common momenta of particles produced in collisions at particle accelerators ($0.1 \lesssim \beta\gamma \lesssim 1000$), a major part of interactions take place between the projectile and electron shells of the atoms in the traversed medium. The atoms are left ionized or excited by these interactions. These processes in the momentum range mentioned above are described by the Bethe-Bloch formula [Tan+18, p.447, eq.33.5]:

$$\left\langle -\frac{\mathrm{d}E}{\mathrm{d}x} \right\rangle = Kz^2 \frac{Z}{A} \frac{1}{\beta^2} \left[\frac{1}{2} \ln \frac{2m_e c^2 \beta^2 \gamma^2 W_{\max}}{I^2} - \beta^2 - \frac{\delta(\beta\gamma)}{2} \right] \tag{3.1}$$

with

$$K = 4\pi N_A r_e^2 m_e c^2 = 0.307\,075 \, \frac{\mathrm{MeVcm}^2}{\mathrm{mol}}$$

$$\beta = \frac{v}{c}, \qquad \gamma = \frac{1}{\sqrt{1-\beta^2}}, \qquad W_{\max} = \frac{2m_e c^2 \beta^2 \gamma^2}{1 + 2\gamma m_e/M + (m_e/M)^2}$$

being the maximum energy transferred to a particle of mass M in a single collision, z being the charge number of the projectile, Z and A being the atomic number and atomic mass of the absorber, I being the mean excitation energy in eV and $\delta(\beta\gamma)$ being a density effect correction to ionization energy loss. Note that the Bethe-Bloch formula only applies for intermediate Z materials. An exemplary plot of the Bethe-Bloch formula is shown in fig. 3.3 for Copper.
A detailed discussion of this formula can be found in [Tan+18, p.447ff., sec.33.2.].

3.3.2 Electrons

Electrons' interaction with matter is dominated by ionizing losses for low energies and bremsstrahlung for medium and higher energies (see fig. 3.4). Bremsstrahlung can be classically understood as the electron changing its flight direction in the electric field
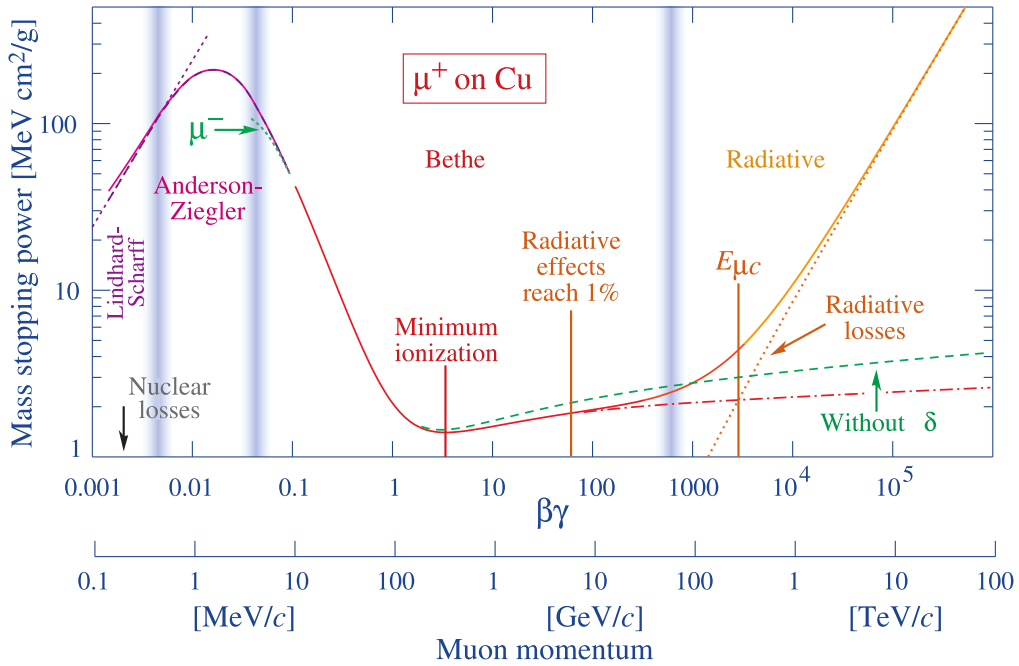
Figure 3.3: The mean energy loss $\langle -\mathrm{d}E/\mathrm{d}x \rangle$ (mass stopping power) of muons in copper as a function of $\beta\gamma$ [Tan+18, p.447, fig.33.1]. The central part labeled 'Bethe' is described by eq. (3.1). For higher momenta radiation losses become the dominant particle interaction. The 'Anderson-Ziegler' regime is described by an empirical fit to data. The 'Linhard-Scharff' region for very low momenta is based off theoretical considerations yielding an energy loss proportional to β [Her16, p.68, fig.3.25]. For even lower momenta non ionizing elastic scattering becomes the dominant interaction.
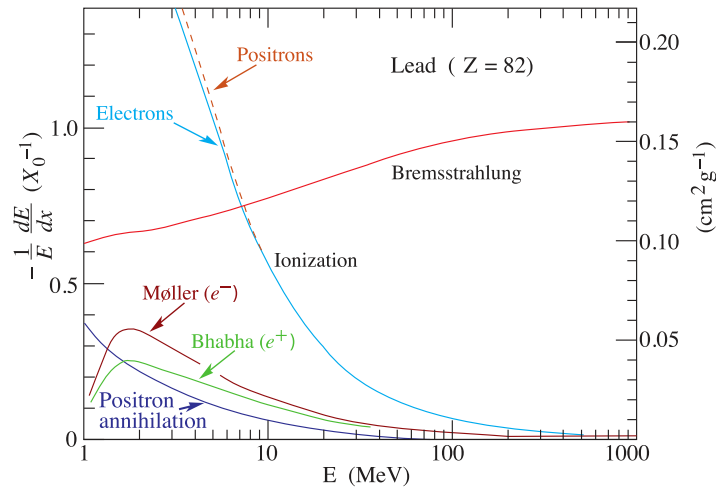
Figure 3.4: Fractional energy loss of electrons or positrons in lead as a function of particle energy[Tan+18, p.453, fig.33.11]. For low energies ionizing scattering is the predominant particle interaction. Interactions with an energy loss above $0.255\,\mathrm{MeV}$ per collision contribute to Bhabha and Møller scattering. Positron annihilation also contributes at lower energies. Above about $7\,\mathrm{MeV}$, bremsstrahlung becomes the dominant interaction.

of a nearby nucleus [Dem14, p.86, sec.4.2.2]. The change in trajectory results in the emitting of a bremsstrahlung photon.

To compare between different materials' stopping power, the material property called radiation length X_0 is defined. For high energy electrons this length defines the distance an electron travels, until it loses all but $\frac{1}{e}$ of its energy due to bremsstrahlung. The values of X_0 can be calculated using [Tan+18, p.452, eq.33.26]. Since the mathematical description is of no importance to this thesis, the details are sparred here.

3.3.3 Photons

The interactions of photons with matter are dominated by three types in the energy regime of interest: Photoelectric effect, Compton effect and pair production (see fig. 3.5).
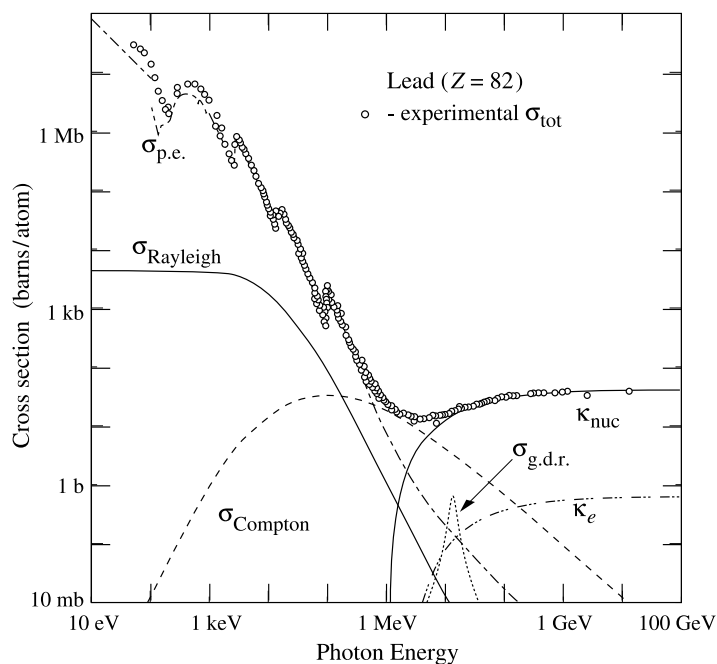
Figure 3.5: The measured cross-section of photon interactions with lead, dependent on the photon energy [Tan+18, p.454, fig.33.15]. The calculated different contributions to the cross-section are shown separately. See text for naming scheme of contributions.

Kolanoski, Wermes 2015
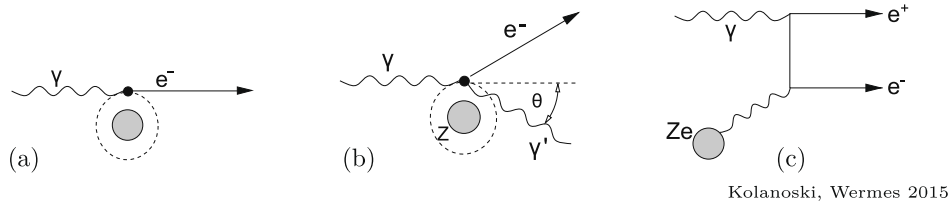
Figure 3.6: A schematic representation of photons interacting with atoms [Her16, p.74, fig.3.31]. The photoelectric effect is shown in (a), the Compton effect in (b) and pair production in (c).

Figure 3.5 shows the different contributions to the total cross-sections for photons of different energies. The abbreviations used in fig. 3.5 stand for:

$$\sigma_{\mathrm{p.e.}} = \text{Atomic photoelectric effect}$$

$$\sigma_{\mathrm{Rayleigh}} = \text{Rayleigh scattering}$$

$$\sigma_{\mathrm{Compton}} = \text{Compton scattering}$$

$$\sigma_{\mathrm{g.d.r.}} = \text{Photonuclear interactions, mostly Giant Dipole Resonance}$$

$$\kappa_{\mathrm{nuc}} = \text{Pair production, nuclear field}$$

$$\kappa_{e} = \text{Pair production, electron field}$$

Visual representations of the three greatest contributors to the cross-section, the photoelectric effect, Compton scattering and pair production, are shown in fig. 3.6. The **photoelectric effect** describes an interaction, where a photon transfers all its energy to an electron previously bound in an atom, ionizing the latter in the process. Threshold energy for this interaction is the binding energy of the loosest bound electron. Excess energy after the ionization of the atom is transformed into kinetic energy of the electron [Dem14, p.87f., sec.4.2.3]. Different peaks occur in the cross-section for the photoelectric effect because stronger bound electrons become accessible to the photons with increasing energy. The effect scales with the number of available electrons in an atom and therefore with the atomic number Z of the absorber. More precisely the photoelectric effect scales with Z^n with $n = 4 - 5$ [Her16, p.78].

Compton scattering is a process of elastic scattering, where the photon interacts with an electron of the outer shell of an atom. The direction and energy of the photon after the interaction is changed. The absorbed energy and momentum is transferred to the atom [Dem16, p.80, sec.3.1.6]. The effect scales with Z for energies above the

binding energy of the electrons. For smaller energies the effect scales with Z^2 [Her16, p.83].

Pair production is a process in which a photon is completely converted into an electron-positron-pair. The threshold energy for this process is the resting mass of the created electron and positron at about $1022\,$keV. Excess energy is transformed into kinetic energy of the electron-proton-pair. A nearby nucleus absorbs the recoil, ensuring conservation of energy and momentum [Dem14, p.88f., sec.4.2.3]. The process scales with Z^2 [Her16, p.87].

3.4 Transition Radiation

TR is an effect on passage of highly relativistic charged particles through material borders, in which photons are created due to experienced changes in plasma frequency in transition of material borders. The intensity of this radiation strongly depends on the Lorentz factor $\gamma = \frac{E}{mc^2}$. This scaling with γ makes transition radiation a suitable tool to distinguish between particles of equal charge and momentum but different masses, for example electrons and pions in collider experiments.

For a single material transition, the differential TR intensity is given by [AYM75, eq. 3.6f.]:

$$
\begin{aligned}
\left(\frac{\mathrm{d}W}{\mathrm{d}\omega}\right)_{\text{single surface}} &= \frac{\alpha}{\pi}\left(\frac{\xi_1^2 + \xi_2^2 + 2\gamma^{-2}}{\xi_1^2 - \xi_2^2}\ln\frac{\gamma^{-2} + \xi_1^2}{\gamma^{-2} + \xi_2^2} - 2\right) \\
&= \frac{\alpha}{\pi}\left(\frac{1 + r + 2\eta^2}{1 - r}\ln\frac{\eta^2 + 1}{\eta^2 + r} - 2\right)
\end{aligned}
\tag{3.2}
$$

with

$$
\xi_{1/2} = \frac{\omega_{P1/2}}{\omega}, \qquad r = \frac{\xi_2^2}{\xi_1^2} = \frac{\omega_{P2}^2}{\omega_{P1}^2}, \qquad \eta = \frac{\omega}{\gamma\omega_{P1}}
$$

and $\omega_{P1/2}$ as the plasma frequencies of the different materials.

The spectral range of transition radiation depends on the specific transition and the Lorentz factor. Further discussion of eq. (3.2) can be found in [AYM75]. Since the mathematical description of the transition radiation is not of major interest for this thesis, this reference shall suffice here.

Utilizing TR for the aforementioned particle identification includes detecting both, charged particles as well as their respective transition radiation.

3.5 Radiator

The particle identification possibilities facilitating TR described in section 3.4 require transition radiation to be generated. *Radiators* maximize TR generation by designed exposition of multiple material transitions. A key design parameter for radiators is the ratio of plasma frequencies of the materials r (see eq. (3.2)). Ideally, these materials have a low material budget and would be transparent for the produced TR, making the TR-yield positively correlated with the thickness of the radiator (compare [AW12, p.125, sec.3.3.1]). Since the TR needs to be measured in order to use it for particle identification, the radiators and detectors of TRDs need to be matched. The detector should be sufficiently sensitive for photons produced in the radiator (in case of MWPCs by choosing a suitable gas). Furthermore, all the TR would ideally reach the sensitive detector parts (unscattered), limiting the range of materials suitable to be between radiator and active detector volume. Besides the outer dimension of the radiator, another spatial consideration is of importance for radiator design: the arrangement of the material transitions. Two major types of radiator can be distinguished from one another by that parameter: regular and irregular radiators [AW12, p.135, sec.3.3.1].
Regular radiators are stacks of parallel oriented layers of material. In irregular radiators, the material transitions are, as the name suggests, irregularly arranged and are characterized by mean length values for the two materials involved. This is typically accomplished by utilizing plastic foams and fibers.
The advantage of irregular radiators is the lower manufacturing effort. Since the material transitions are randomly arranged regardless of the orientation of the foils, the production of these radiators is feasible for large scale detectors. In general, this is not the case for regular radiators[18, p. 92, sec. 2.2.]. One advantage of regular radiators is a higher TR yield when normalized to a constant thickness in radiation lengths compared to irregular radiators [OBr+93, p. 6], [AW12, p. 135, sec. 3.3.1].

3.6 Multi Wire Proportional Chamber

MWPCs are gas-based particle detectors commonly used in accelerator experiments. Depending on the design chosen for a specific MWPC, these detectors can measure the energy deposition of ionizing radiation and charged particles at a limited ($\propto 100\,\mu m$) spatial resolution [Mas17, s. 52].

The principle of operation is based on the ionization of a gas within an electric field. The ionized gas atoms and electrons are accelerated by the field enabling them to further ionize the gas. The subsequently created ions and electrons get accelerated towards the electrodes again and so on, creating an avalanche of charge collected at the latter [Mas17, s.39]. The collected charge is proportional to the energy deposited by the ionizing radiation into the detector gas.
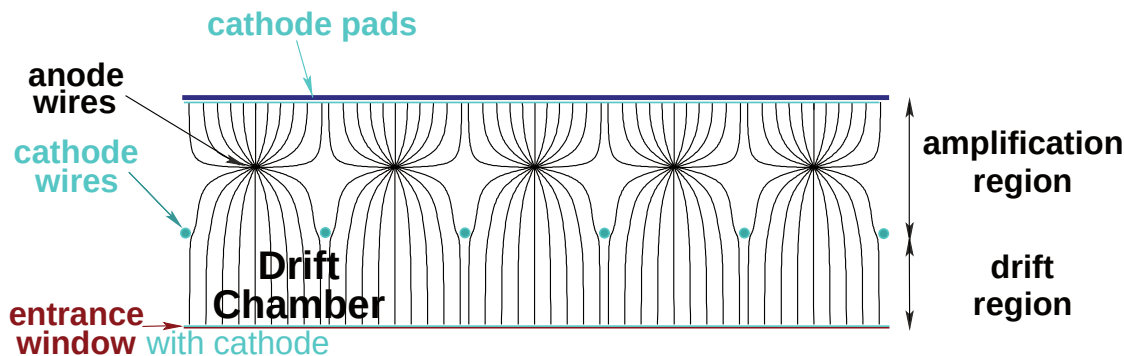
Figure 3.7: A schematic illustration of an MWPC [BBE18, p.35, fig.4.1., modified].

The aforementioned electric field is generated between anode and cathode wires and, for the TRD-MWPCs, planar cathodes at one side of the gas volume. A schematic drawing of an exemplary field is shown in fig. 3.7. In some MWPCs, the electric field is not limited to an amplification region where the previously described avalanche takes place. Often a region of smaller electric field precedes the amplification region (as shown in fig. 3.7). This drift region can ensure a sufficiently high interaction probability of the particles with the detector gas (see for example [BBE18, p.63]). Depending on the specific MWPC design other positive effects might be gained from adding a drift region. In case of the CBM-TRD for example, readout chamber stabilization under external pressure variations and reduction of charge cluster size are targeted by adding a drift region [BBE18, p.63].

The charge collected at the anode wires can be read out directly as a current [Her16, p.220ff.]. However, this method is uncommon in detector operation. Instead, the back panels of such chambers are typically covered in cathode pads [Mas17, s.52] [Her16, p.222]. The charge assembled at the anode wires is mirrored in the cathode pads, measurable by suitable readout electronics. The analysis of relative charge proportion of neighboring pads allows a spatial resolution above the geometrical shape of these pads [Her16, p.222].

The gas choice for an MWPC depends on the specific demands for the detector. Typically, the gas consists mostly of an inert noble gas, often Argon or Xenon, and a quencher gas. Criteria for the former include a high ionization density, proportionality between signal and ionization, small diffusion, suitable drift velocity, low production of space charge and radiation hardness (see [Her16, p.198]). The quencher gas is introduced to absorb stray photons originating in the ionization and discharge processes, preventing them from starting a new delayed avalanche distant from the primary ionisation [Lui08, p.128], [Her16, p.199]. Typical gases for this function are carbon dioxide and methane[Her16, p.199f.]. Since the gas composition is of such great importance for detector operation, great consideration is put into MWPCs gas tightness. The entry of impurities might negatively impact detector performance and has to be compensated, adding cost.
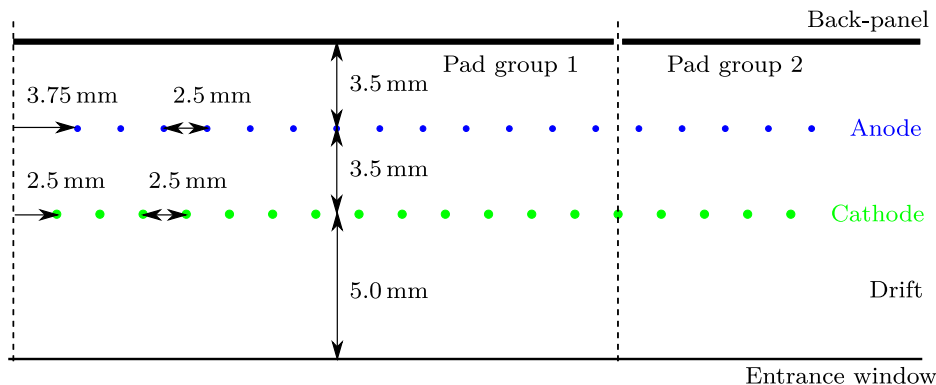
3.7 TRD Modules of the CBM Experiment

The design goals discussed in section 3.2 are met by a rectangular pad based MWPC-design with a symmetrical $3.5\,\text{mm} + 3.5\,\text{mm}$ amplification and a $5\,\text{mm}$ drift region [BBE18, p. 18, tab. 2.1].
The wire geometry of the modules is shown in fig. 3.8. In the middle of the amplification region, $3.5\,\text{mm}$ from the back panel, the anode wire layer is located. The wire next to the frame of the gas volume is located $3.75\,\text{mm}$ from the inner wall. The wire gap within a layer is $2.5\,\text{mm}$.
The cathode wire layer marks the end of the amplification and the beginning of the drift region at $7\,\text{mm}$ distance from the back panel. These wires are pitched by $1.25\,\text{mm}$ relative to the wires of the anode wire plane. The wire next to the inner wall of the gas volume is therefor at $2.5\,\text{mm}$ distance from said wall.
The entrance window limits the drift region and the gas volume and is located another $5\,\text{mm}$ away from the cathode wire plane, at $12\,\text{mm}$ distance form the back panel. A schematic drawing of the interior module dimensions is shown in fig. 3.8. The material and structural choices concerning gas tightness are discussed in section 3.8.

Figure 3.8: A schematic drawing of the inner dimensions of the MWPCs for the CBM experiment [BBE18, p.67, fig.5.13].

The drift region of the CBM TRD MWPCs of 5 mm is small compared to other MWPC-based TRDs, like the *A Large Ion Collider Experiment* (ALICE) TRD's 30 mm drift region [Cor01, p.23, fig.4.6]. The small drift region still enhances the photon absorption probability over the level of an otherwise identical MWPC without a drift region, while not extending the signal collection and readout time over the design goal of 300 ns [BBE18, p.61f. sec.5.3] [Käh21].

The attained gain depends on the voltages applied to the wires and the gas choice. For the detector operation in the CBM experiment Xe/CO_2 (85/15) is the gas of choice. The anode voltage for this gas mixture is 1850 V, while the drift voltage remains unchanged for the available options at -500 V [BBE18, p.58, tab.5.1].

A mixture of Xenon and CO_2 is chosen, as only Xenon ensures sufficient TR photon absorption.

While the wire spacing and dimensions along the beam axis are all the same for every module discussed in this thesis, the pad dimensions and sizes vary for different modules at different sections of the detector. In the inner regions of the detector, where the highest hit rate will occur, the pad size is the smallest, as shown in fig. 3.9 and table 3.1, since a hit rate of 100 kHz per pad must not be surpassed (see fig. 3.9). In the outer regions of the detector a bigger pad size is sufficient because the local hit rate is lower. This choice lowers the cost of the detector and limits the overall heat output and power consumption (compare [BBE18, p.73]).

The radiator for the CBM-TRD is a 30 cm thick irregular radiator consisting of Polyethylene (PE) foam mats stacked in a box made of *Rohacell HF71*. The *Rohacell* does not cover the site of the radiator facing the entrance window. The space withing
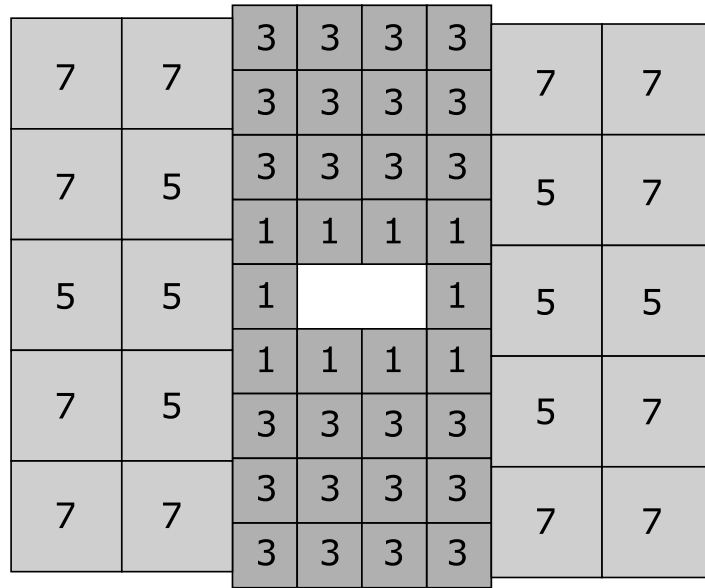
Figure 3.9: A sketch of one layer of the TRD detector wall, consisting of the different module types 1, 3, 5 and 7 [BBE18, p.104, Fig.8.2]. The different module types are of different dimensions and pad-sizes, as mentioned previously in section 3.7 and specified in table 3.1. The even numbered chamber types are prototypes not included in the final detector. The inner zone filled with module type 1 might be replaced by different MWPCs not discussed in this thesis.

Table 3.1: An overview of the different module types' (pad-) dimensions, highlighting the differences between them [BBE18, Tab.5.4, Sec.5.5.1, p.72].

Module type	Outer dimensions	Pad dimensions (H×W)
1	$57\,\text{cm} \times 57\,\text{cm}$	$1.75\,\text{cm} \times 0.68\,\text{cm}$
3	$57\,\text{cm} \times 57\,\text{cm}$	$6.75\,\text{cm} \times 0.68\,\text{cm}$
5	$99\,\text{cm} \times 99\,\text{cm}$	$4.00\,\text{cm} \times 0.67\,\text{cm}$
7	$99\,\text{cm} \times 99\,\text{cm}$	$12.00\,\text{cm} \times 0.67\,\text{cm}$

the carbon lattice mentioned in section 3.8 is filled in with the same PE mats to fully utilize the available space and ensure maximum TR yield [BBE18, p.84, sec. 6.3.2].

3.8 Chamber Structure regarding Gas Tightness
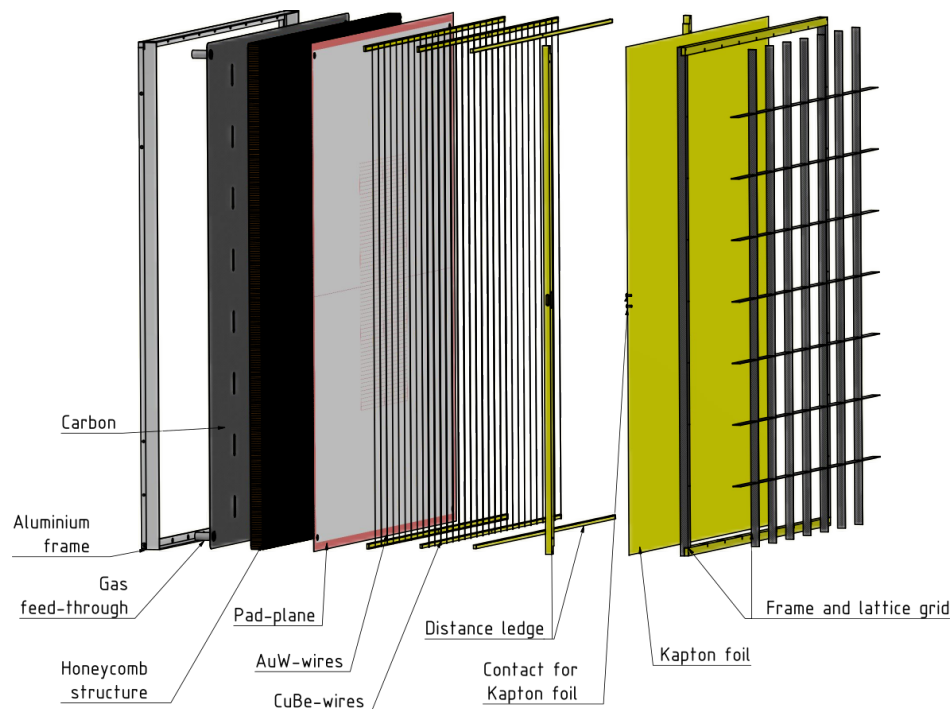
Figure 3.10: A schematic drawing of the different layers of a CBM-TRD module [BBE18, p.65, Figure 5.10]. The individual parts of the back panel, glued together to form one pad covered plane are not visible in this graphic.

Joins at material transitions are possible leak sites. Therefore, the mechanical structure of the TRD is of key importance for investigations towards gas leakage.

The TRD modules consist of several components, shown in fig. 3.10. A carbon lattice in a fiberglass frame supports the aluminum coated *Kapton* entrance window. The gas volume is upheld by fiberglass bars, clamping the glued in high voltage wires in between them. A Printed Circuit Board (PCB) back panel covered in copper pads encloses the back of the gas volume. Honeycomb and a carbon layer in an aluminum frame ensure structural integrity of the chamber. Preliminary gas connectors in all four corners of the chamber allow for the MWPC to be supplied with a suitable gas mixture. The different components are held together by epoxy resin. Of importance for the gas tightness, but not shown distinctly in fig. 3.10 is that the PCB back panel is not a continuous structure. It is, instead, composed of several PCBs, depending on the module size [BBE18, p.72, Sec.5.5.1]. The edges of these PCBs are grouted with additional glue at the segment edge to ensure tightness besides the composed nature of the backpanel.

Additional to the possible occurrence of leak sites, the mechanical structure limits the differential pressure the module can be operated under. The maximum overpressure applied to the entrance window is 1 mbar which results in a peak deformation of the window of 1 mm. This limit of acceptable deformation is based on simulations of the electric field within the TRD module [BBE18, p.107, sec.8.3].

3.8.1 The Investigated Prototype

The prototype investiagted in this thesis project is one of type 8/2015 completed in 2016. These prototypes are slightly smaller than the larger final modules, measuring 95 cm × 95 cm. The pad plane's segmentation and electrical connections are designed differently compared to the final chamber. The gas connectors are completely re-designed for the final module. Apart from these deviations, the components and their arrangement is as discussed.

This prototype in particular already was investigated towards its leak tightness after production. Some attempts were made to seal leaks found in the module, by adding epoxy glue covered and *Kapton* tape. Tape was applied while the glue was still liquid.

3.9 Equations of State

Equations of state describe relations between state variables. The two most common equations of state, the ideal gas equation and the Van der Waals equation, are described and compared in this section to motivate the use of the ideal gas equation in all further analyses.

3.9.1 Ideal Gas

The simplest equation of state is the ideal gas equation [Nol12, p.156, eqs.1.7, 1.10]:

$$pV = Nk_\mathrm{B}T = nRT \tag{3.3}$$

where p, V and T are pressure, volume and temperature of the gas and N is the number of gas particles within that volume. The number of moles n equals $\frac{N}{N_\mathrm{A}}$ [Nol12, p.156], where $N_\mathrm{A} = 6.022\,52 \cdot 10^{23}\,\mathrm{mol}^{-1}$ [Nol12, p.156, eq.1.8] is the Avogadro-constant. $k_B = 1.3805 \cdot 10^{-23}\,\frac{\mathrm{J}}{\mathrm{K}}$ [Nol12, p.155, eq.1.6] is the Boltzmann-constant, and R is the universal gas constant given by $k_\mathrm{B}N_\mathrm{A} = 8.3166\,\frac{\mathrm{J}}{\mathrm{molK}}$ [Nol12, p.156, eq.1.9].

Two conditions must be approximately fulfilled for a gas to be described by Equation (3.3) [Nol12, p.154, sec.1.4.1]:

1. The gas molecules do not have a volume in and of themselves.

2. There is no interaction between the particles.

In reality, these conditions are only completely fulfilled for infinitely diluted gases [Nol12, p.154, sec.1.4.1].

3.9.2 Van der Waals-Gas

The Van der Waals equation of state expands the ideal gas equation. It takes a minimum, nonzero volume of gas molecules into account and adds an internal pressure to the observed pressure p [Nol12, p.156f., sec.1.4.2]. The resulting Van der Waals equation [Nol12, p.157, eq.1.14] is:

$$\left(p + a\frac{n^2}{V^2} \right)(V - nb) = nRT. \tag{3.4}$$

The constants a and b are material dependent parameters.

In the derivation of this equation of state, it is implied that only one phase of matter is present[Nol12, p.159, sec.1.4.2, §3]. This is not always true. However, the gases of interest in this thesis are Argon and carbon dioxide. At atmospheric pressure ($101\,325\,\mathrm{Pa}$), the boiling point of Argon is $-185.87\,^{\circ}\mathrm{C}$ [Dea99, p.3.17]. Carbon dioxide sublimates at atmospheric pressure at a temperature of $-78.44\,^{\circ}\mathrm{C}$ [Dea99, p.3.23]. Room temperature is well above these temperatures. Therefore, a coexistence of phases of these gases is not expected.

3.9.3 Comparison: Ideal Gas and Van der Waals-Gas

In the context of this thesis, the usage of the ideal gas equation eases analysis and calculations. To justify this usage, a comparison between the ideal gas and the Van der Waals-Gas for the use case of this thesis is made.

Table 3.2: Van der Waals coefficients for Argon[Dea99, p.5.157], CO_2[Dea99, p.5.158] and Xenon[Dea99, p.5.168]. The greater the values for a and b, the bigger is the deviation from the ideal gas. This can be seen in eq. (3.4), where the ideal gas equation is reproduced for $a = b = 0$.

	a $[\frac{\mathrm{L^2 bar}}{\mathrm{mol^2}}]$	a $[\frac{\mathrm{m^6 Pa}}{\mathrm{mol^2}}]$	b $[\frac{\mathrm{L}}{\mathrm{mol}}]$	b $[\frac{\mathrm{m^3}}{\mathrm{mol}}]$
Argon	1.355	0.1355	$3.201 \cdot 10^{-2}$	$3.201 \cdot 10^{-5}$
CO_2	3.658	0.3658	$4.284 \cdot 10^{-2}$	$4.284 \cdot 10^{-5}$
Xenon	4.192	0.4192	$5.156 \cdot 10^{-2}$	$5.156 \cdot 10^{-5}$

The Van der Waals coefficients for Argon and CO_2 are denoted in table 3.2.

In the coming chapters the relations between volume V and particle number N are of interest. Equation (3.4) can be written as

$$pV + a\frac{n^2}{V} - n(pb + RT) - ab\frac{n^3}{V^2} = 0.$$

With $p_{\mathrm{max}} \approx 1014.25\,\mathrm{hPa} = 1\,\mathrm{atm} + 1\,\mathrm{mbar}$, $V = 0.011\,\mathrm{m^3}$, $T \approx 300\,\mathrm{K}$ and the Van der Waals coefficients for CO_2 from table 3.2 this equation yields a mole number of $n \approx 0.449$[1]. With the same parameters, the ideal gas equation, eq. (3.3), yields $n \approx 0.447$. For the worst case scenario, where all the gas in the setup is CO_2, the derivation from an ideal gas is still less than $1\,\%$ for the parameters in this setup. The use of the ideal gas equation for the analyses of the data obtained is therefore completely warranted.

[1]Numerically solved by the `fsolve` function of the `scipy` package for python 3.

3.10 Hagen-Poiseuille Equation

The Hagen-Poiseuille equation describes the laminar volume flow through a cylindrical pipe of length L and radius R. The flowing matter is an incompressible Newtonian fluid of viscosity η (compare [Dem15, p.219ff.]). The Hagen-Poiseuille law states [Dem15, p.223, eq.8.31]:

$$I_V = \frac{\pi R^4}{8\eta L}\Delta p$$

where I_V is the volume flow and Δp is the difference in pressure at both ends of the pipe.

This equation in and of itself is not of importance to the thesis. However, the observation that the volume outflow scales linear with the differential pressure applied is key to the conducted measurements and the data analyses. The applicability of this relation to chamber leakage is not obvious, but is supported by measurements conducted for a chamber prototype in [Fab21].
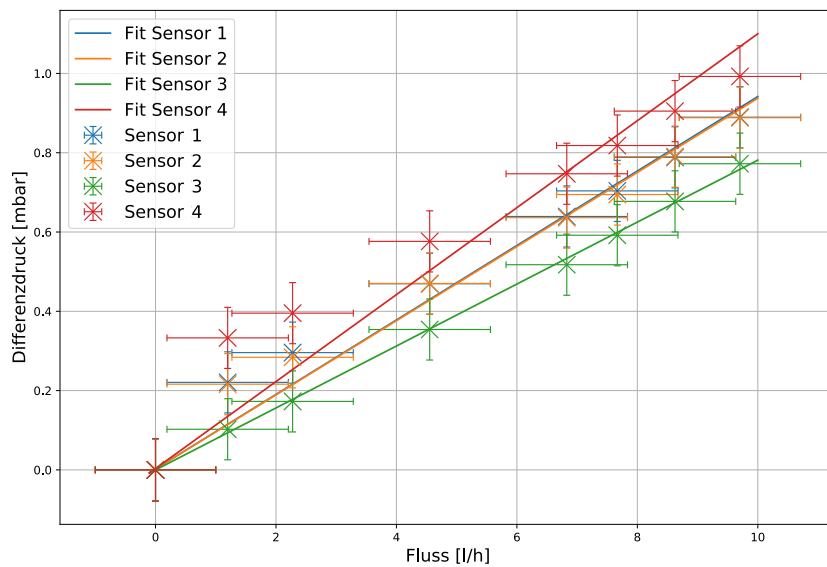
Figure 3.11: The relation between differential pressure and leakage flow[Fab21, p.69, fig.5.21, edited to fix key]. The fits for sensors 1 and 2 overlap and are therefore hard to differentiate.

Figure 3.11 shows the relation between differential pressure and the resulting leakage rates. At least for greater leakages, this linear relation is approximately true. This is expected, since the difference in pressure is the driving force behind the leakage volume flow.

3.11 Mathematical Description of the Pressure Decay

To describe the loss of differential pressure over time, several assumptions regarding the behavior of the system are made.

As discussed in section 3.10, the volume-outflow of gas is linearly related to the differential pressure Δp. This loss in gas volume translates directly to a loss in particle number, as can be seen in the ideal gas equation, eq. (3.3). A reduction of particle number results in a reduction of pressure. Thus, a reduction of the chamber volume also is a result of particles leaving the gas system, as further discussed in section 3.12. To disentangle these dependencies, the leakage of the gas system is described by an outflow of particles per unit of time:

$$N(t) = N_0 - \int_0^t F\Delta p(t')\mathrm{d}t' \tag{3.5}$$

where N_0 is the particle number at the beginning of the measurement ($t = 0$) and F is a constant outflow parameter.

For the volume, the pressure dependency is discussed in section 3.12. The pressure- and thereby time- dependent volume can be written as

$$V(t) = V_0 + B\Delta p(t). \tag{3.6}$$

The volume V_0 is the module volume at no overpressure given by its geometry. B is the additional volume due to deformation of the window and carbon grid, estimated to be $(0.577 \pm 0.087) \frac{\mathrm{L}}{\mathrm{mbar}}$ for the smaller prototypes. This value is derived in section 3.12. The ambient temperature T_{Amb} and pressure p_{Amb} are either assumed to be constant or time dependent. The case dependent implications for the equation at hand are discussed in the following subsections.

3.11.1 Constant Ambient Pressure and Temperature

The ambient temperature T_{Amb} is estimated to be constant over time and space. As is done for the ambient pressure p_{Amb}.

Inserting eq. (3.5) and eq. (3.6) into the ideal gas equation, eq. (3.3), yields the differential equation

$$p(t)(V_0 + B(p(t) - p_{\mathrm{Amb}})) = \left(N_0 - \int_0^t (p(t') - p_{\mathrm{Amb}})F\mathrm{d}t'\right)k_{\mathrm{B}}T_{\mathrm{Amb}}. \tag{3.7}$$

Differentiating and simplifying this equation yields

$$\dot{p}(t)(V_0 - p_{\mathrm{Amb}}B) + p(t)Fk_{\mathrm{B}}T_{\mathrm{Amb}} + 2p(t)\dot{p}(t)B - p_{\mathrm{Amb}}Fk_{\mathrm{B}}T_{\mathrm{Amb}} = 0. \tag{3.8}$$

This equation is solved in good approximation by an exponential decay of the pressure:

$$p(t) = \Delta p_0 e^{-\lambda t} + p_{\mathrm{Amb}} \qquad \dot{p}(t) = -\lambda \Delta p_0 e^{-\lambda t} \tag{3.9}$$

where Δp_0 is the overpressure at the beginning of the measurement and λ is a decay parameter.

Inserting this Ansatz into eq. (3.8) starts the following calculation:

$$-\Delta p_0 \lambda e^{-\lambda t}(V_0 - p_{\mathrm{Amb}}B) + \left(\Delta p_0 e^{-\lambda t} + p_{\mathrm{Amb}}\right) Fk_{\mathrm{B}}T_{\mathrm{Amb}}$$
$$+ 2\left(\Delta p_0 e^{-\lambda t} + p_{\mathrm{Amb}}\right)\left(-\lambda \Delta p_0 e^{-\lambda t}\right) B - p_{\mathrm{Amb}}Fk_{\mathrm{B}}T_{\mathrm{Amb}} = 0$$

$$\Leftrightarrow \Delta p_0 e^{-\lambda t}\left(-\lambda(V_0 - p_{\mathrm{Amb}}B) + Fk_{\mathrm{B}}T_{\mathrm{Amb}} - 2\Delta p_0 \lambda e^{-\lambda t}B - 2p_{\mathrm{Amb}}\lambda B\right) = 0$$

$$\Rightarrow -\lambda V_0 - p_{\mathrm{Amb}}\lambda B + Fk_{\mathrm{B}}T_{\mathrm{Amb}} - 2\Delta p_0 \lambda e^{-\lambda t}B = 0$$

$$\Leftrightarrow -\lambda\left(V_0 + B\left(p_{\mathrm{Amb}} + 2\Delta p_0 e^{-\lambda t}\right)\right) + Fk_{\mathrm{B}}T_{\mathrm{Amb}} = 0$$

$$\Leftrightarrow \lambda\left(V_0 + Bp_{\mathrm{Amb}} \underbrace{\left(1 + 2\frac{\Delta p_0}{p_{\mathrm{Amb}}}e^{-\lambda t}\right)}_{\approx 1,\text{ since } e^{-\lambda t} \le 1 \text{ and } \frac{\Delta p_0}{p_{\mathrm{Amb}}} \approx 0.001}\right) = Fk_{\mathrm{B}}T_{\mathrm{Amb}}$$

$$\Rightarrow F = \frac{\lambda(V_0 + Bp_{\mathrm{Amb}})}{k_{\mathrm{B}}T_{\mathrm{Amb}}} \tag{3.10}$$

By the means of this equation, the decay parameter λ can be translated into a particle number flow F. This particle flow can be calculated into a volume flow as mentioned in section 3.9. Using the ideal gas equation, eq. (3.3), an expression for the volume of N particles can be found:

$$V = \frac{Nk_{\mathrm{B}}T}{p}.$$

Substituting the N in this equation with F yields the volume flow

$$F_V = \lambda \left(\frac{V_0}{p_{\text{Amb}}} + B \right). \tag{3.11}$$

This expression allows to calculate the volume of leaked gas in the ambient atmosphere. To get this expression, the temperature of the gas is assumed to equal ambient temperature. Since the gas inside the system is expected to be the same temperature as the room, this should be an appropriate approximation. The loss of temperature due to decompression, since the module is at a small overpressure, is negligible because the over pressure is very small compared to ambient pressure.

3.11.2 Time Dependent Ambient Pressure

Especially for longer measurement cycles, the approximation of ambient pressure as constant becomes unreasonable.
Taking into account the time dependency of the ambient pressure in eq. (3.7), while still differentiating and simplifying, yields

$$\dot{p}(t)V_0 + 2p(t)\dot{p}(t)B - \dot{p}(t)p_{\text{Amb}}(t)B - p(t)\dot{p}_{\text{Amb}}(t)B$$
$$= -p(t)Fk_{\text{B}}T + p_{\text{Amb}}(t)Fk_{\text{B}}T. \tag{3.12}$$

This equation is far more complex than the time independent equation in eq. (3.8). An analytical solution is not found. Taking into account changes in ambient temperature would further complicate this equation.

3.12 Volume Estimation

The change in chamber volume as a function of pressure is of key importance for the calculation of the volume leakage rate based on the decay parameter λ determined by fits, as motivated in section 3.11.
As discussed in section 3.8, the volume of the chamber modules depends on the overpressure applied to them. The entrance window and the carbon grid across it are flexible and bend outwards if the overpressure rises.
Since the actual shape of the entrance window is fairly complicated, composed of the bending of the foil in each window subsection on top of the bending of the grid, it is

natural to separate these factors. Simplified models are motivated and compared to available data.

3.12.1 Added Volume of the Bending Foil

The bending of the foil is a process dominated by the flexibility of the foil and the pressure applied to it. Since the pressure inside the chamber bends the foil towards regions of lower pressure, the force applied to the foil is always orthogonal to its surface. Because the pressure across one window section is constant and the sections are quadratic, the bending of the foil will be symmetric.

As can be deduced from the ideal gas equation, eq. (3.3), the pressure is minimized if the volume is maximized. Since the elasticity of the foil is restricting the expansion of the volume, the length of the foil must stay minimal. This problem in the field of calculus of variations is sometimes called the 'problem of Dido'. The solution to the problem, maximizing the area while maintaining the circumference, is a circular arc[Ble19, p.99ff. 'Aufgabe 6'].

One can assign an osculating circle with radius r to every point within the window-section-square, characterizing the circular arc above it. The length r is calculated from the 'diameter' ϱ, and the maximum bulge b, as shown in fig. 3.12. ϱ is a straight line through the origin, meaning the center of the square, and the point $P(x_0|y_0)$ limited by the square of side length L, the borders formed by the carbon lattice. Figure 3.12 shows the named variables.
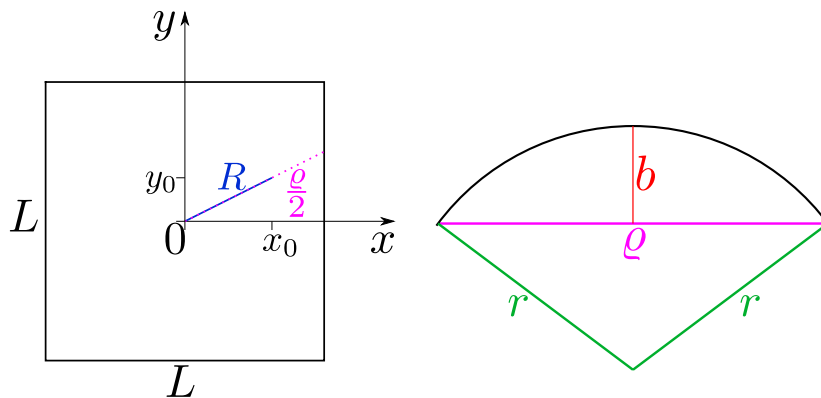
Figure 3.12: A sketch presenting the basic parameters of the model. One square section of the entrance window confined within the carbon lattice is shown on the left. The quantities R and ϱ are drawn for the point $P(x_0|y_0)$. On the right side of the sketch, the osculating circle-arc of radius r is shown in relation to the square-diameter ϱ and the bulge maximum b.

Geometrical considerations lead to expressions for the named quantities. R is determined by use of the pythagorean theorem:

$$R = \sqrt{x_0^2 + y_0^2}.$$

ϱ is derived by means of trigonometric functions. If α is the angle between R and the x-axis, $\sin(\alpha) = \frac{y_0}{R}$. As visible in fig. 3.12, $\varrho = \frac{L}{\sin(\alpha)}$ for $|x_0| < |y_0|$. Combining the two equations yields

$$\varrho = \begin{cases} \frac{LR}{y_0} & \text{for } |x_0| < |y_0| \\ \frac{LR}{x_0} & \text{for } |x_0| \geq |y_0| \end{cases}$$

The second equation for ϱ is derived similarly to the first one.

The radius of the osculating circle r can also be derived from the pythagorean theorem on the right side of fig. 3.12. The triangle of interest is the on defined by r as the hypotenuse and $\frac{\varrho}{2}$ and $r - b$ as legs. The resulting formula is

$$\left(\frac{\varrho}{2}\right)^2 + (r - b)^2 = r^2$$
$$\Leftrightarrow \frac{\varrho^2}{4} + r^2 - 2rb + b^2 = r^2$$
$$\Leftrightarrow \qquad r = \frac{\varrho^2}{8b} + \frac{b}{2}.$$

Finally, the height h of a given point along the square-diameter has to be determined. This is done by combining the basic proportionality theorem with trigonometric functions. The former is used to obtain the relation

$$\frac{R}{r - b + h} = \frac{R'}{r - b}.$$
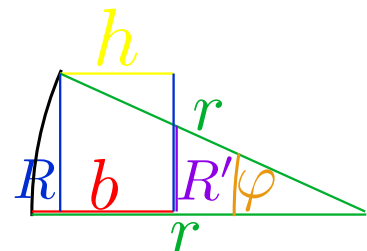
The sketch on the right side is rotated, but shares color-coding with fig. 3.12. The angle φ can be described by a trigonometric relation

$$\sin(\varphi) = \frac{R}{r} = \sin\left(\arctan\left(\frac{R'}{r-b}\right)\right) = \frac{\frac{R'}{r-b}}{\sqrt{\left(\frac{R'}{r-b}\right)^2 + 1}}.$$

The last step uses a trigonometric identity. This expression can be solved towards $\frac{R'}{r-b}$ and inserted into the first relation to obtain

$$h(R,r) = r\sqrt{1 - \left(\frac{R}{r}\right)^2} - r + b. \tag{3.13}$$

Plotting this model results in fig. 3.13. The shape in fig. 3.13 is not observed at the real window segments. Especially the sharp edges in the diagonals of the plot are not found in reality. Simulating the window expansion is complicated and this description matches the data available, as discussed later in this section. The model is therefore used as an approximation.
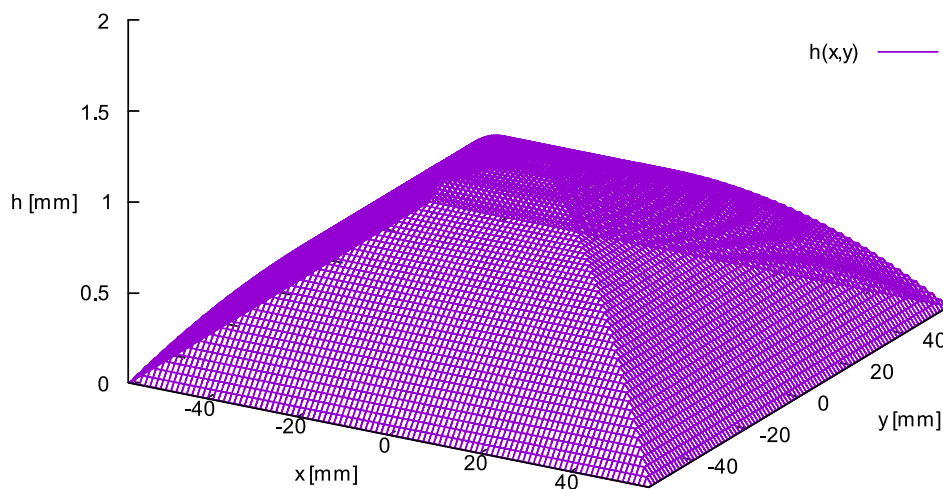
Figure 3.13: The shape resulting from assigning an osculating circle to every 'diameter' ϱ, as discussed in eq. (3.13) and the text. The h-axis is out of proportion to better display the bulge. The square-corners of each level visible in this plot are not observed in reality. The chosen display method highlights this flaw.

To determine the volume of the bulge displayed in fig. 3.13, a random number based method is chosen. Three random numbers are generated a million times for each bulge height b. Two of the numbers select a point within a subsection of the window-segment: x is chosen between $-\frac{L}{2}$ and $\frac{L}{2}$ and y is chosen between $-\frac{L}{2}$ and $\frac{L}{2}$. This corresponds to a random point within the limits of the shape depicted in fig. 3.12. For this random
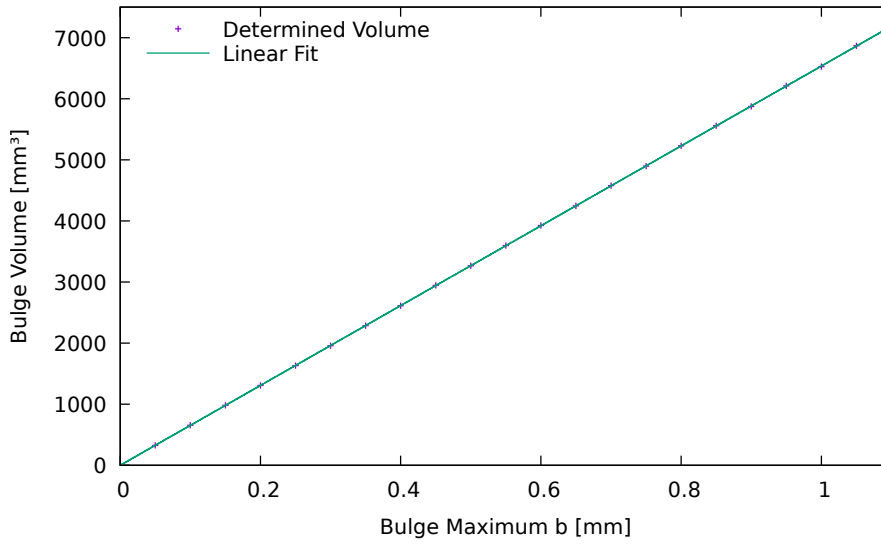
Figure 3.14: The bulge volume determined by the random number method with a linear function fitted to the data. The volume determined is for the earlier TRD prototype with a width of $95\,\text{cm}$. This figure changed due to the error discussed in chapter 1.

point the height $h(x, y)$ is calculated. The third random number z lays between zero and b. The instances N_{count}, where $z \leq h(x, y)$, are counted. The ratio between N_{count} and the total number of triplets $N_{\text{total}} = 1\,000\,000$ equals the ratio of the volume of the bulge V_b and the volume of the encasing cuboid V_C:

$$\frac{N_{\text{count}}}{N_{\text{total}}} = \frac{V_b}{V_C}$$

$$\Leftrightarrow \quad V_b = \frac{N_{\text{count}}}{N_{\text{total}}} V_C$$

$$\Leftrightarrow \quad V_b = \frac{N_{\text{count}}}{N_{\text{total}}} L^2 b \tag{3.14}$$

This method of volume determination is applied to bulge heights b between $0.05\,\text{mm}$ and $1.05\,\text{mm}$ in $0.05\,\text{mm}$-steps. The data shown in fig. 3.14 shows a very clear linear dependency of the bulge volume on the bulge height b. The linear fit applied in fig. 3.14 is based on the model

$$V_b(b) = m \cdot L^2 \cdot b.$$

The fit parameter m is determined to be $0.5002 \pm 0.0010 \approx \frac{1}{2}$. The total volume contribution from the bulges of the entrance window foil in each of the 64 window segments is therefore:

$$V_b = 32L^2 \cdot b \qquad (3.15)$$

For the real modules of width $99\,\mathrm{cm}$, the relation between applied differential pressure and bulge height b is known quantitatively. This is not the case for the prototype used in this setup.

The bigger window segments of the larger modules mean that the force applied to them, which is based on the pressure, is bigger by a factor of $(L_{\mathrm{larger}}/L_{\mathrm{smaller}})^2$. The force limiting the expansion of the foil is based on its elasticity. The more foil available for expansion, the lower the stress on each infinitesimal foil segment. Therefore, another factor of $\frac{L_{\mathrm{larger}}}{L_{\mathrm{smaller}}}$ is taken into account. Adjustments to this factor might be necessary. In [Fab21, p.43ff., sec.5.2] measurements towards the bulging of an entrance window segment are conducted. The obtained data are used to check the applicability of the model to the data. Both, the bulging of the foil and the bending of the lattice is measured separately in [Fab21]. For both measurements, a reference height is installed to a $99\,\mathrm{cm} \times 99\,\mathrm{cm}$ test module. The distance between the bending module components and the sturdy reference is measured. For detailed information about the procedures, see [Fab21].

Applying the model showcased in fig. 3.12 to the data acquired in [Fab21] leads to plots like fig. 3.15. As can be seen in fig. 3.15, the osculating circle describes the bulge of the entrance window well within the uncertainties of the measurement values.

This is not true for all measurements conducted in [Fab21]. Especially at low differential pressures, where the bulge is small, the measurement value spreading complicates the analysis. Still, the model is compatible with the data obtained in [Fab21] and describes the observed bulge within the uncertainties of the measurement points. Plots like fig. 3.15 for the other data obtained in [Fab21] are shown in appendix A.1.

The additional detector volume, added by the deformation of the entrance window foil, is described by eq. (3.15). The only unknown parameter in this equation is the bulge height b. In [Fab21], the relation between applied pressure and b is investigated. The results in [Fab21, p.57, tab.5.1, Mittelwert, Fenster 2] for a window segment in the
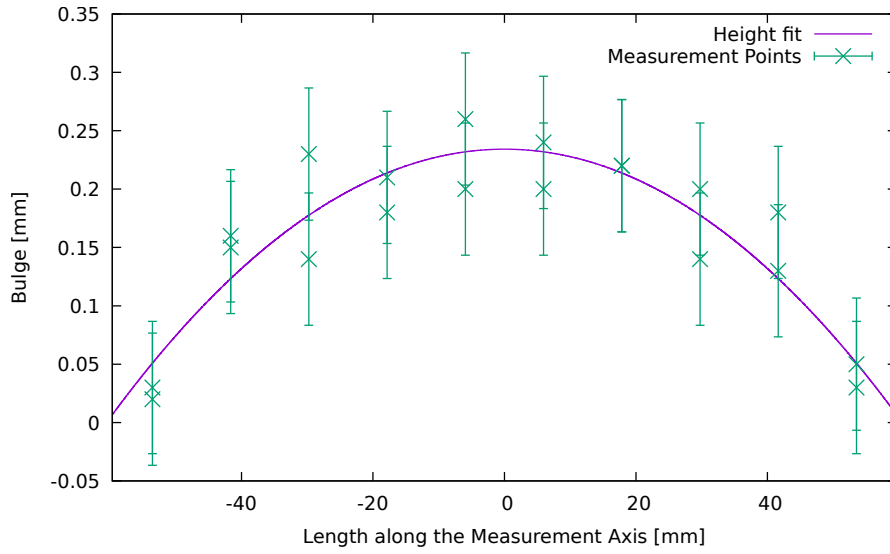
Figure 3.15: The height model described in eq. (3.13) applied to a measurement taken in [Fab21].

middle of the module are used. This leads to a pressure dependent volume contribution of

$$V_b(\Delta p) = 32 \cdot (114.3\,\mathrm{mm})^2 \cdot \left(\frac{114.3\,\mathrm{mm}}{119.3\,\mathrm{mm}}\right)^3 \cdot (0.421 \pm 0.004)\,\frac{\mathrm{mm}}{\mathrm{mbar}} \cdot \Delta p$$

$$\approx (154\,790 \pm 1471)\,\frac{\mathrm{mm}^3}{\mathrm{mbar}}\Delta p \approx (0.155 \pm 0.001)\,\frac{\mathrm{L}}{\mathrm{mbar}}\Delta p \qquad (3.16)$$

for the smaller prototypes of a width of 95 cm.

3.12.2 Added Volume by Deformation of the Grid

For the estimation of the volume that results from the carbon lattice flexing under the applied pressure, the previously discussed model can not be applied. Since the carbon ledges are stiff and connected rigidly to the fiberglass frame of the entrance window, it can not be expected that they behave like a parabola.

For a precise estimation, engineer's beam theory might be applied. However, since the application of beam theory to this two-dimensional problem with non-trivial load distribution is complicated, the shape of the grid distortion is instead estimated by a polynomial $\mathrm{Grid}(x, y)$ fitted to the data acquired in [Fab21, p.48, sec.5.2.1.4]. For the small bulges observed for the chambers, this Ansatz seems reasonable.

From the shape and symmetry of the entrance window several conditions for $\mathrm{Grid}(x, y)$ can be derived:

- The edges of the entrance window are by definition zero.

- Since the lattice is rigidly connected to the frame, the grid should be horizontal at the edges.

- The entrance window is mirror symmetric along the x- and y-axes. The polynomial $\mathrm{Grid}(x, y)$ must reflect this fact by sharing this property.

- The maximum of the grid-bulge g is expected in the center of the entrance window.

These conditions are trivially met in one dimension by a polynomial:

$$\mathrm{Grid_{1d}}(x) = \frac{16g}{W^4}x^4 - \frac{8g}{W^2}x^2 + g \tag{3.17}$$

where W is the width of the carbon grid. W can be calculated by subtracting $3\,\mathrm{cm}$ from the total width of a module.

To account for systematic uncertainties, this model is corrected by an offset g_{offset} and a tilt $m \cdot x$. This yields

$$\mathrm{Grid_{1dCorrected}}(x) = \frac{16g}{W^4}x^4 - \frac{8g}{W^2}x^2 + mx + g + g_{\mathrm{offset}}. \tag{3.18}$$

Figure 3.16a shows two data sets at different pressures from both conducted measurements with different reference-orientation, along the horizontal and vertical axes of the module. The model is in good agreement with the data. The plots are shown for all data in appendix A.2.

The applied tilt is mostly consistent for each measurement, as can be seen in fig. 3.16b. This suggests that the tilt is a real physical effect. The greatest deviation from this trend is seen for the first measurement points for each category, where the applied differential pressure is the lowest and the resulting bulge is the smallest.

The same is true for the applied offset g_{offset} shown in fig. 3.16c. The fitted constants are mostly within the error bars of the fit parameters obtained by applying eq. (3.18). Since eq. (3.18) describes the measured bulge well, eq. (3.17) can be used to further develop the volume estimation.

Expanding the model from eq. (3.17) to a two-dimensional $\mathrm{Grid}(x, y)$ could be done in different ways.

Equation (3.17) could be rotated along the z-axis and applied similar to eq. (3.13).
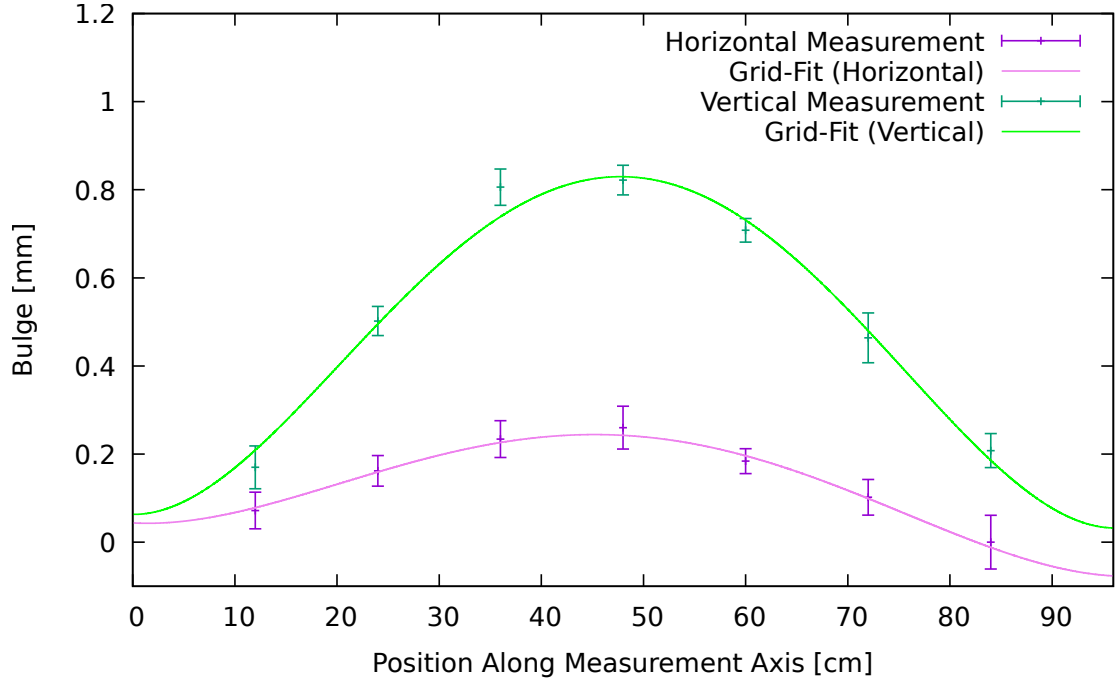
(a) The model given in eq. (3.18) applied to different data sets from [Fab21]. The differential pressure varies between the datasets. The impacts of the tilt m and the offset g_{offset} are visible in the deviation from zero at the limits of the shown range.
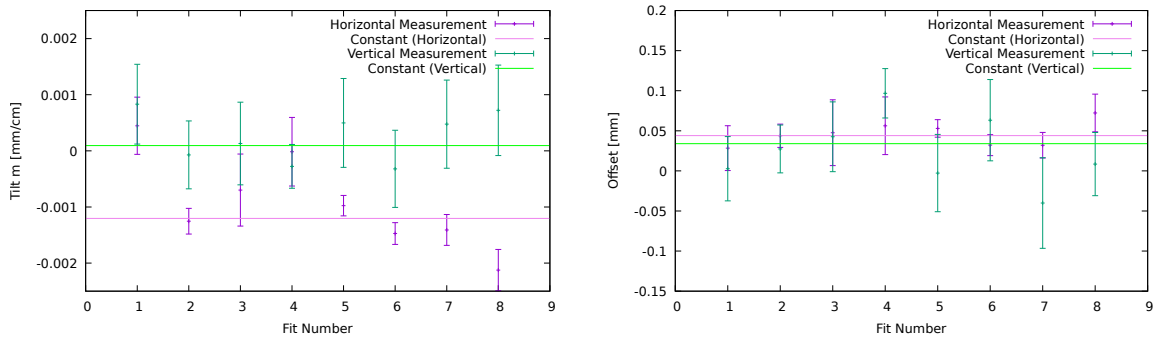
(b) The different tilts m for the available datasets. The error bars are the uncertainty of the fit parameter.

(c) The different offsets g_{offset} for the available datasets. The error bars are the uncertainty for the fit parameter.

Figure 3.16: Different plots showcasing the applicability of eq. (3.18) to the data acquired in [Fab21]. The tilt m should have been corrected by the offset measurement conducted in [Fab21]. But since sub-figure b shows consistency between different pressures for the same measurements, the tilt seems to have not been corrected completely. The same seems to apply to the offset g_{offset} shown in sub-figure c.
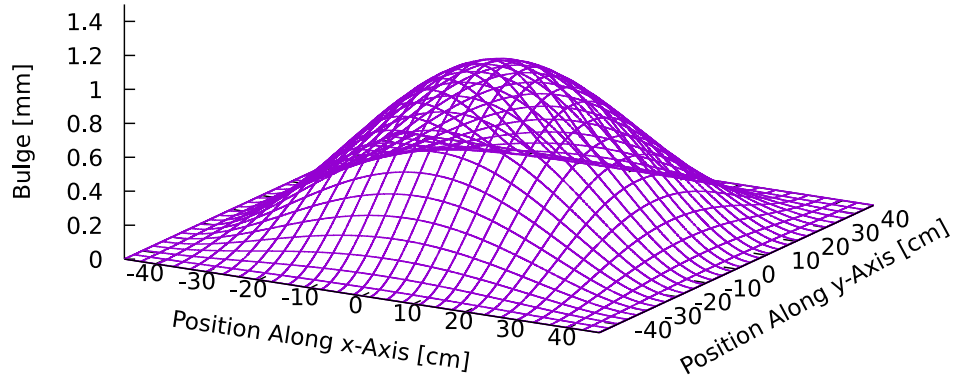
Figure 3.17: A plot of eq. (3.19) for $W = 92\,\text{cm}$ and $g = 1\,\text{mm}$. The z-axis is out of proportion, leading to the bulge being exaggerated.

However, this could violate the condition, that the incline of $\text{Grid}(x, y)$ must be zero at the edges of the grid. Additionally, since the grid is not connected in the corners of the entrance window, it must not meet the same conditions in the diagonal as it does in the horizontal and vertical direction. Instead, the expansion to a two-dimensional model is done by replacing g in eq. (3.17) with $Grid_{\text{1d}}(y)$. The resulting two-dimensional grid-model is given by

$$\text{Grid}(x, y) =$$
$$g \left(\frac{16}{W^4} \left(\frac{16x^4}{W^4} - \frac{8x^2}{W^2} + 1 \right) y^4 - \frac{8}{W^2} \left(\frac{16x^4}{W^4} - \frac{8x^2}{W^2} + 1 \right) y^2 + \frac{16x^4}{W^4} - \frac{8x^2}{W^2} + 1 \right).$$
$$(3.19)$$

The resulting shape is seen in figure fig. 3.17. The volume estimation is done similar to the previously discussed model, by utilizing random numbers. The resulting volume is shown in fig. 3.18. A linear connection between the bulge maximum g and the volume is found. The slope of the linear fit is determined to be $0.2845 \pm 0.0001 W^2$. The

uncertainty of this slope is negligible. This result matches the analytically calculated integral of eq. (3.19):

$$
\begin{aligned}
V_{\text{Grid}}(g) &= \int_{-\frac{W}{2}}^{\frac{W}{2}} \int_{-\frac{W}{2}}^{\frac{W}{2}} \text{Grid}(x,y)\mathrm{d}x\mathrm{d}y \\
&= \int_{-\frac{W}{2}}^{\frac{W}{2}} \int_{-\frac{W}{2}}^{\frac{W}{2}} g\left(\frac{16x^4}{W^4} - \frac{8x^2}{W^2} + 1\right)\left(\frac{16y^4}{W^4} - \frac{8y^2}{W^2} + 1\right)\mathrm{d}x\mathrm{d}y \\
&= \int_{-\frac{W}{2}}^{\frac{W}{2}} g\left(\frac{16y^4}{W^4} - \frac{8y^2}{W^2} + 1\right)\left[\frac{16x^5}{5W^4} - \frac{8x^3}{3W^2} + x\right]_{-\frac{W}{2}}^{\frac{W}{2}}\mathrm{d}y \\
&= \int_{-\frac{W}{2}}^{\frac{W}{2}} 2g\left(\frac{16y^4}{W^4} - \frac{8y^2}{W^2} + 1\right)\left[\frac{16x^5}{5W^4} - \frac{8x^3}{3W^2} + x\right]_{0}^{\frac{W}{2}}\mathrm{d}y \\
&= \int_{-\frac{W}{2}}^{\frac{W}{2}} 2g\left(\frac{16y^4}{W^4} - \frac{8y^2}{W^2} + 1\right)\left(\frac{16\frac{W^5}{32}}{5W^4} - \frac{8\frac{W^3}{8}}{3W^2} + \frac{W}{2}\right)\mathrm{d}y \\
&= \int_{-\frac{W}{2}}^{\frac{W}{2}} 2g\left(\frac{16y^4}{W^4} - \frac{8y^2}{W^2} + 1\right)\left(\frac{W}{10} - \frac{W}{3} + \frac{W}{2}\right)\mathrm{d}y \\
&= \int_{-\frac{W}{2}}^{\frac{W}{2}} 2g\left(\frac{16y^4}{W^4} - \frac{8y^2}{W^2} + 1\right)\left(\frac{4W}{15}\right)\mathrm{d}y \\
&= 4g\left(\frac{4W}{15}\right)^2 \\
&= \frac{64}{225}gW^2 \\
&= 0.28\bar{4}gW^2
\end{aligned}
$$

The volume of the grid bulge is therefore

$$
V_{\text{Grid}}(g) = \frac{64}{225}W^2 g. \tag{3.20}
$$

The relation between applied overpressure and measured g is discussed in [Fab21]. The function connecting overpressure in mbar to the grid bulge in mm is [Fab21, p.142, tab.B.47]:

$$
g(\Delta p) = (1.02 \pm 0.02)\,\frac{\text{mm}}{\text{mbar}} \cdot \Delta p - (0.01 \pm 0.01)\,\text{mm} \tag{3.21}
$$

For the purposes of estimating the volume, the offset is neglected.

Applying this relation to the smaller prototypes with $W = 92\,\text{cm}$, instead of the $96\,\text{cm}$ prototype used for the measurements in [Fab21], requires similar adjustments to the ones applied to b. Again, the applied force scales with W^2. The sturdiness of the
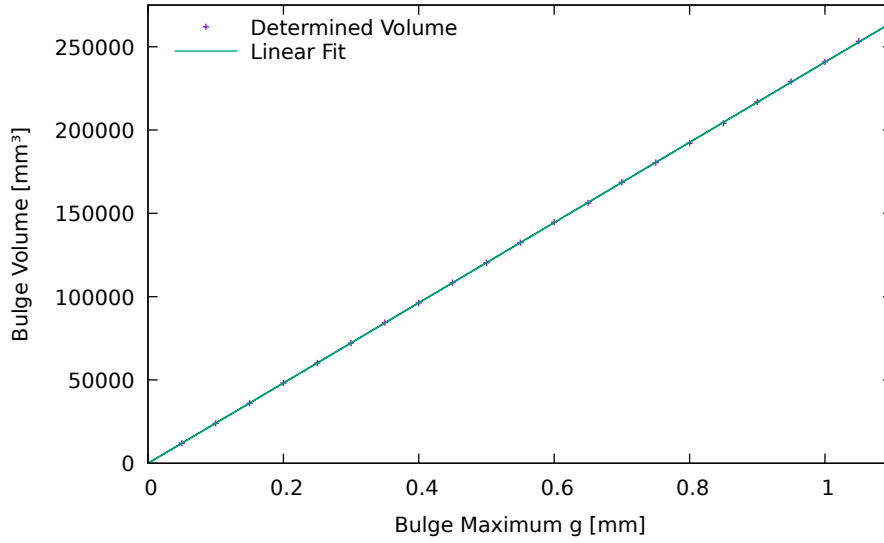
Figure 3.18: The volume determined by the random number method previously discussed. The volume increases linearly. The applied fit does not have an offset. The slope of the graph is determined to be $0.2845 \pm 0.0001 W^2$. This figure changed due to the error discussed in chapter 1.

carbon grid depends on the beam cross-section of the lattice. The increased length of the beams adds to the leverage the force has on the beams. The grid-bulge is therefor adjusted by a factor of $(92\,\mathrm{cm}/96\,\mathrm{cm})^3$.

The pressure dependent grid bulge is

$$V_g(\Delta p) = \frac{64}{225} \cdot (920\,\mathrm{mm})^2 \cdot (1.02 \pm 0.02)\,\frac{\mathrm{mm}}{\mathrm{mbar}} \cdot \left(\frac{92\,\mathrm{cm}}{96\,\mathrm{cm}}\right)^3 \Delta p$$

$$\approx (216\,134 \pm 4238)\,\frac{\mathrm{mm}^3}{\mathrm{mbar}}\Delta p \approx (0.216 \pm 0.004)\,\frac{\mathrm{L}}{\mathrm{mbar}}\Delta p \qquad (3.22)$$

Total Volume Added

The complete additional volume V_{add} is the sum of the bulge of the grid, eq. (3.22), and the bulge of the window sections, eq. (3.16):

$$V_{\mathrm{add}}(\Delta p) = V_b(\Delta p) + V_g(\Delta p) = (0.371 \pm 0.004)\,\frac{\mathrm{L}}{\mathrm{mbar}}\Delta p \qquad (3.23)$$

Since this result is based on simplified models and the data are scaled with crude scaling methods, an uncertainty of $15\,\%$ is assigned to this value. This results in the overpressure dependent added volume of

$$V_{\mathrm{add}}(\Delta p) = (0.371 \pm 0.056)\,\frac{\mathrm{L}}{\mathrm{mbar}}\Delta p. \tag{3.24}$$

The volume contribution of the bubbler is negligible compared to this volume increase due to bulging of the module.

3.13 Handling of Uncertainties of Averages

The averages in this document are weighted averages:

$$\bar{x}_{\mathrm{wtd}} = \frac{\sum_{i=1}^{n} w_i x_i}{\sum_{i=1}^{n} w_i} \tag{3.25}$$

where the weights w_i are the reciprocal uncertainties of the values x_i.

The variance of this average is described by [Kir06, p.1, eq.2]

$$\begin{aligned}
Var(x)_{\mathrm{wtd}} &= \frac{\sum_{i=1}^{n} w_i (x_i - \bar{x}_{\mathrm{wtd}})^2}{\sum_{i=1}^{n} w_i}\frac{n}{n-1}\\
&= \left(\frac{\sum_{i=1}^{n} w_i x_i^2}{\sum_{i=1}^{n} w_i} - (\bar{x}_{\mathrm{wtd}})^2\right)\frac{n}{n-1}.
\end{aligned} \tag{3.26}$$

The derived standard error of the mean $(s_{\bar{x}})_{\mathrm{wtd}}$ is then given by [Kir06, p.1, eq.3]

$$(s_{\bar{x}})_{\mathrm{wtd}} = \sqrt{\frac{Var(x)_{\mathrm{wtd}}}{n}} = \sqrt{\left(\frac{\sum_{i=1}^{n} w_i x_i^2}{\sum_{i=1}^{n} w_i} - (\bar{x}_{\mathrm{wtd}})^2\right)\frac{1}{n-1}}. \tag{3.27}$$

This statistical uncertainty is combined with the maximum systematic uncertainty $u_{\mathrm{max}}(\mathrm{Sensor})$ of each sensor in the averaging interval. The individual systematic uncertainties of the sensor outputs are discussed in section 4.3.

These considerations yield a total uncertainty of

$$u_{\mathrm{total}} = \sqrt{((s_{\bar{x}})_{\mathrm{wtd}})^2 + (u_{\mathrm{max}}(\mathrm{Sensor}))^2}. \tag{3.28}$$

In most plots of measurement data shown in this document, the displayed data are averaged over sixty measurement points unless otherwise specified. For all sensors

involved in the setup described in section 4.3 the systematic uncertainty outweighs the statistical uncertainty.

4 Gas Tightness of CBM-TRD Modules

## 4.1 Measurement of Leakage through the Entrance Window

The Aluminum coated *Kapton* foil used for the entrance window of the TRD-chambers is checked for its leak-tightness. The setup used employs Ultrahigh Vacuum (UHV) technics and mass spectrometry to measure the leakage rate of *Kapton* foil for Xenon. The measurements are crosschecked with a calibrated Helium leak tester to ensure the validity of the procedure. The experiment was designed, build, operated and partially analyzed by Daniel Bonaventura. The documentation of the measurement is based on [Bon21a]. The analyses are expended upon. Upper limits for gas leakages besides Xenon are determined. Furthermore, a relative pressure analysis substantiates the evidence for a minor leakage in the foil fixture.

4.1.1 Setup

This setup measures the leakage of the Aluminum coated *Kapton* membrane by subjecting it to a high vacuum at one side, and Xenon on the other. A mass spectrometer connected to the evacuated part of the setup measures the partial pressures of residue gases, resolved in their molar masses. The partial pressures in combination with the suction efficiency of the pump for the respective gases yield quantitative leakage rates for specific gases through the setup. Commented pictures of the setup are shown in fig. 4.1 and fig. 4.2.
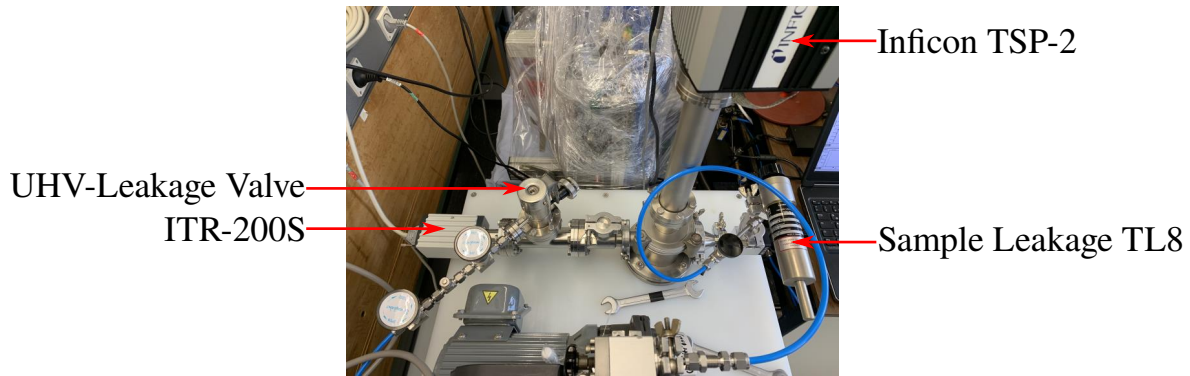
Figure 4.1: A photo of the setup, taken from a vantage point [Bon21a, p.3]. Visible from left to right: The absolute pressure sensor *ITR-200S*, the UHV leakage valve, the quadrupole mass spectrometer type *Inficon TSP-2* and the Helium sample leakage TL8.
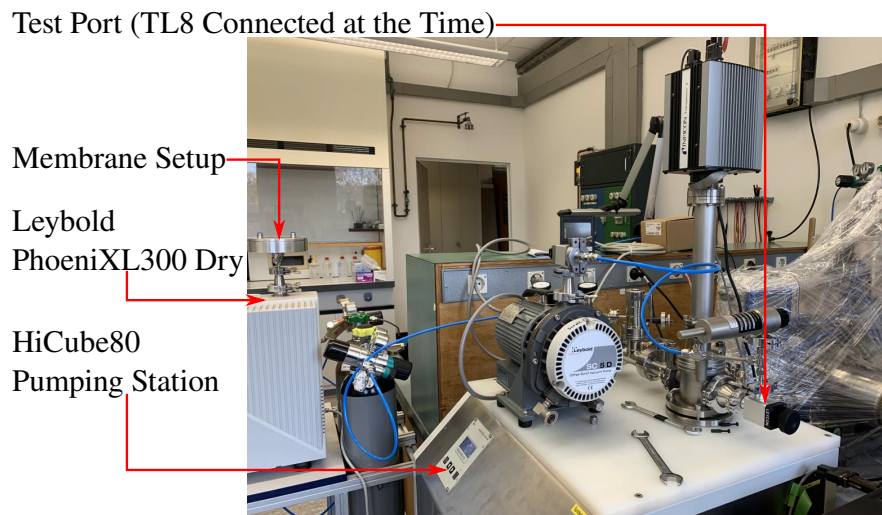
Figure 4.2: A different perspective of the setup [Bon21a, p.3]. The Helium leakage sampler *Leybold PhoeniXL300 dry* is visible on the left-hand side, with the membrane setup on top. The ultra high vacuum test stand *Pfeiffer HiCube 80* provides the foundation for the setup. The nearest instrument visible is the previously mentioned sample leakage *TL8*, which, at the time of photography, is connected to the test port of the setup.

4.1.2 Pilot Measurements and Calibration

To ensure calibration of the used *Inficon TSP-2* mass spectrometer, measurements regarding the output partial pressure are conducted. The execution of the measurement process begins with the evacuation of major parts of the setup, utilizing the *Pfeiffer HiCube 80*. When an absolute pressure of below $1 \cdot 10^{-6}$ mbar, measured by the *ITR-200S* absolute pressure sensor, is reached, pure Nitrogen is admitted into the setup by

means of the UHV leakage valve. Since the vacuum was sufficiently high before this admission of Nitrogen, the partial pressure measured by the *TSP-2* mass spectrometer for Nitrogen equals the total pressure in the setup, and the peak of Nitrogen in the spectrum of the *TSP-2* is the most prominent one. The data acquired serve as the first point for a two point calibration of the absolute pressure measurement of the *TSP-2*. The second point is measured by repetition of the described procedure with an approximately ten times higher Nitrogen intake.

This calibration procedure is not perfect. The *ITR-200S* has an accuracy of $\pm 10\%$ [Bon21a]. Furthermore, the Nitrogen peaks used for the calibration are pushing the upper limit for partial pressures of the mass spectrometer [Bon21a].

The *TSP-2* outputs a partial pressure of Nitrogen below the total pressure in the setup measured by *ITR-200S*. Since, in good approximation, the entirety of the pressure in the setup originates from the admitted Nitrogen, the amplifier gain of the mass spectrometer is adjusted until the output data reflect that fact. After this calibration procedure, the Nitrogen is cut off from the setup.

4.1.3 Leakage Tests

In the following leakage tests, the unit $\frac{\text{mbar} \cdot \text{L}}{\text{s}}$ will be featured prominently. A leakage rate of $1\,\frac{\text{mbar} \cdot \text{L}}{\text{s}}$ corresponds to a change in pressure of $1\,\text{mbar}$ in $1\,\text{s}$ for a volume of $1\,\text{L}$ (compare [Ley, above eq.1.7]).

Accordingly, eq. (3.3) can be used to translate this unit into $\frac{\text{L}}{\text{h}}$. The number of particles leaked into the volume through the leakage each second can be calculated:

$$1\,\frac{\text{mbar} \cdot \text{L}}{\text{s}} = pV\frac{1}{\text{s}} = Nk_{\text{B}}T\frac{1}{\text{s}}$$
$$\Leftrightarrow \qquad N = \frac{1}{k_{\text{B}}T}\text{mbar} \cdot \text{L}.$$

From this, a corresponding volume at atmospheric pressure ($1013.25\,\text{mbar}$) can be derived:

$$pV = Nk_{\text{B}}T \qquad \Leftrightarrow \qquad V = \frac{Nk_{\text{B}}T}{p}$$
$$\Rightarrow \qquad V = \frac{\frac{1}{k_{\text{B}}T}\text{mbar} \cdot \text{L} \cdot k_{\text{B}}T}{p}$$
$$\Leftrightarrow \qquad V = \frac{1\,\text{mbar} \cdot \text{L}}{p} \approx 986.92 \cdot 10^{-6}\,\text{L}$$

Since the common unit is $\frac{L}{h}$, this value has to be multiplied by 3600 to conclude

$$1\,\frac{\text{mbar} \cdot \text{L}}{\text{s}} \approx 3.5529\,\frac{\text{L}}{\text{h}}. \tag{4.1}$$

This conversion is an approximation. Besides the ideal gas approximation, the atmospheric pressure often differs from the given value. Regardless, a similar conversion is common practice in vacuum applications (see [Ley, tab.7a], [Bon21a, p.15]).

Reference: Helium Leakage of Membrane and Sample Leak

To crosscheck the setup including the *TSP-2* mass spectrometer regarding quantitative findings of gas tightness, a sample leak and the *Kapton* membrane are tested with both setups, the *Leybold PhoeniXL300 dry* and the mass spectrometer setup, towards their respective Helium leakage rate.

The *PhoeniXL300 dry* outputs a leakage rate of $2.3 \cdot 10^{-8}\,\frac{\text{mbar} \cdot \text{L}}{\text{s}}$ for the sample leakage and $8.0 \cdot 10^{-5}\,\frac{\text{mbar} \cdot \text{L}}{\text{s}}$ for the membrane respectively.

For the setup including the *TSP-2*, both parts, the membrane and the sample leakage, are connected to the testing port of the setup subsequently. The connected antechamber is evacuated using a scroll pump. Connection to the rest of the setup is established and in case of the sample leakage the latter gets opened. The intake of Helium is expected to depend on the suction efficiency of the *Pfeiffer HiCube 80* vacuum pump for Helium. This is specified to be $S_{\text{eff}} = 58\,\frac{\text{L}}{\text{s}}$ [Vac22, p.3]. Combining this suction efficiency with the partial pressure measured by the *TSP-2* mass spectrometer yields Helium leakage rates of $1.39 \cdot 10^{-8}\,\frac{\text{mbar} \cdot \text{L}}{\text{s}}$ for the *TL8* sample leakage and $3.55 \cdot 10^{-5}\,\frac{\text{mbar} \cdot \text{L}}{\text{s}}$ for the *Kapton* membrane respectively.

Comparison of the two data sets allows conclusions towards the reliability of the method. First, it can be noted that the determined leakage rates are in the same order of magnitude for both methods of acquisition. However, the quantitative differences amount to $165\,\%$ for the *TL8* sample leakage and to $225\,\%$ for the *Kapton* membrane. The setup including the *TSP-2* mass spectrometer measures roughly half the leakage of the one measured with the *PhoeniXL300 dry* leak tester.

This deviation could have a variety of reasons. The specified suction efficiency might not be accurate for this setup, since it is specified at the vacuum flange of the pump, while the mass spectrometer is a distance away from this position, as can be discerned in fig. 4.1 and fig. 4.2. The calibration of the *PhoeniXL300 dry* leak tester could be
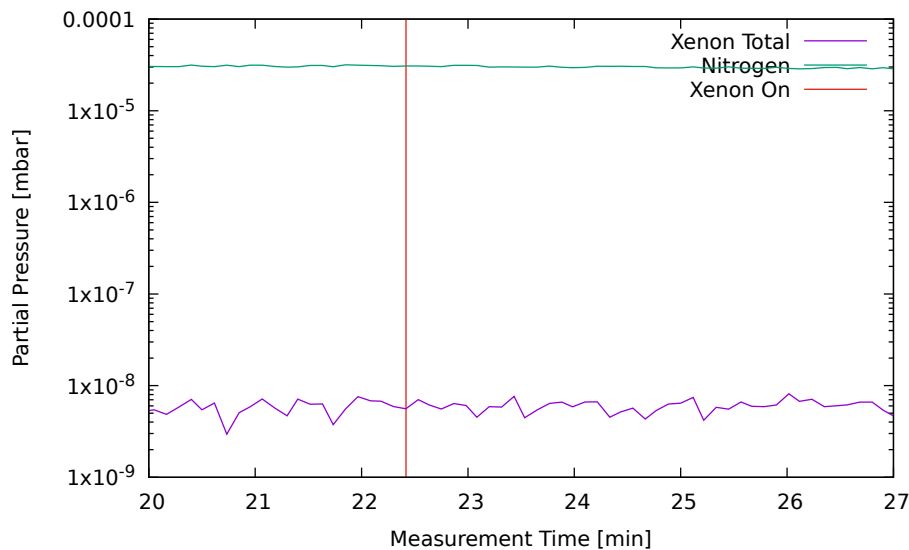
Figure 4.3: The output of the *TSP-2* mass spectrometer over measurement time with the membrane connected to the analyzed volume. At 'Xenon On' the flushing of the membrane with Xenon begins. 'Xenon Total' is the sum of the outputs for $m = 128\,\text{u}, 129\,\text{u}, 130\,\text{u}, 131\,\text{u}, 132\,\text{u}, 134\,\text{u}$ and $136\,\text{u}$. 'Nitrogen' is the measurement output for $m = 28\,\text{u}$.

faulty, temperature dependencies are unchecked, the absolute pressure sensor might be unreliable, residue gas might have a bigger impact than expected, the connections to the different setups might be of different quality and many more [Bon21a, p.10].

Regardless of these valid points of criticism, the discrepancies between the output of the *Leybold PhoeniXL300 dry* and this test measurement are in the same direction and in the same order of magnitude. The results are therefore plausible and suitable for an order of magnitude check.

Xenon Leakage of the Membrane

To determine the Xenon leakage rate of the membrane, the membrane is connected to the test port of the setup shown in fig. 4.1. The setup is evacuated. The *TSP-2* mass spectrometer is set to measure all masses up to $140\,\text{u}$. All stable Xenon isotopes are therefore measurable with this setup. The side of the membrane not facing the vacuum is flooded with Xenon, while spectra are measured. In fig. 4.3 the mass spectra recorded by the spectrometer are shown. In the beginning of the measurement the membrane is connected to the setup, but not flushed with Xenon. The key observation is the absence of a significant increase in partial pressure of Xenon when the flushing of the membrane begins at 'Xenon On'.
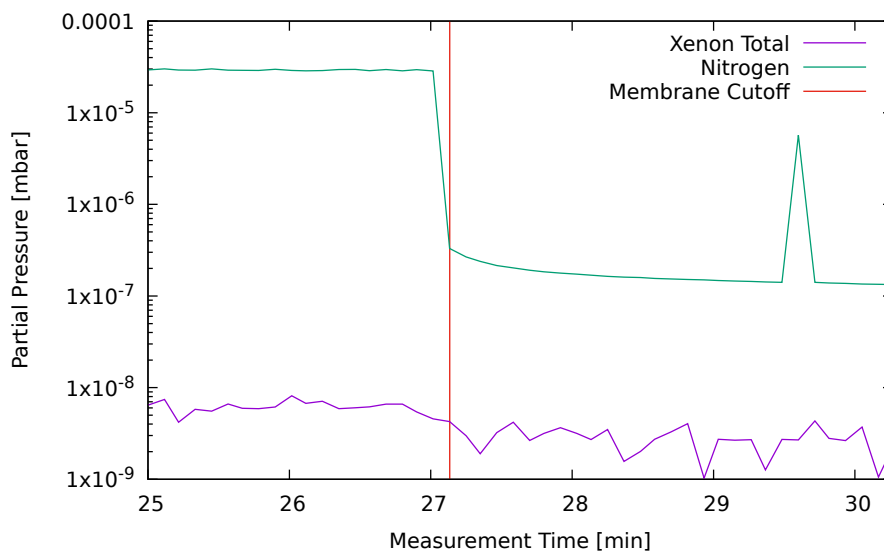
Figure 4.4: The development of Xenon and Nitrogen partial pressures with the cut-off of the membrane from the vacuum. 'Xenon Total' is the sum of the outputs for $m = 128\,\mathrm{u}, 129\,\mathrm{u}, 130\,\mathrm{u}, 131\,\mathrm{u}, 132\,\mathrm{u}, 134\,\mathrm{u}$ and $136\,\mathrm{u}$. 'Nitrogen' is the measurement output for $m = 28\,\mathrm{u}$.

The visible fluctuations in 'Xenon Total' over time are due to limitations of measurement accuracy for very low partial pressures. Measurement values in the regime of $10^{-9}\,\mathrm{mbar}$ are not quantitatively reliable on their own, but the trends observed remain true.

 The decrease of Xenon after the membrane cut off, visible in fig. 4.4, is either a sign for a base amount of Xenon diffusing through the membrane, or of a minor leakage in the antechamber connected to the test port. The rapid decrease in Nitrogen pressure with cut off of the test port suggests a previous intake of air, pointing towards a leakage in the membrane holder or connected parts. Since the membrane is flushed with Xenon, the leakage is more likely to be located in the connected fittings.

The peak in Nitrogen partial pressure is unexpected. There is no information regarding its origin, however, since it is only a short increase and returns to the previous baseline immediately after, it is not further discussed.

To test the sensitivity of the mass spectrometer towards Xenon, a small amount of the latter is leaked into the setup through the UHV leakage valve. The resulting development of partial pressures is shown in fig. 4.5. Beginning with the leakage of Xenon into the setup at 'Xenon Inlet', the partial pressure of Xenon increases linearly, the curvature visible in fig. 4.5 is the result of the logarithmic scale. This behavior is expected and confirms that the mass spectrometer is sensitive to Xenon.
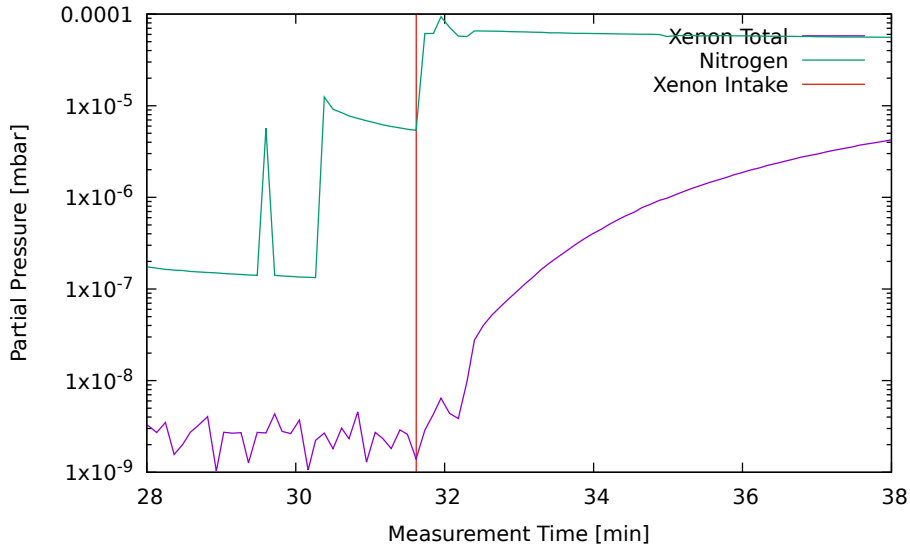
Figure 4.5: The development of Xenon and Nitrogen partial pressures with intake of Xenon through the leak valve beginning at 'Xenon Intake'. 'Xenon Total' is the sum of the outputs for $m = 128\,\mathrm{u}, 129\,\mathrm{u}, 130\,\mathrm{u}, 131\,\mathrm{u}, 132\,\mathrm{u}, 134\,\mathrm{u}$ and $136\,\mathrm{u}$. 'Nitrogen' is the measurement output for $m = 28\,\mathrm{u}$.

Conclusion

The entrance window foil contributes very little to the leakage of the TRD modules. Fitting a constant to the total Xenon content during the flushing of the membrane with Xenon yields a partial pressure of $(5.9 \pm 0.1) \cdot 10^{-9}\,\mathrm{mbar}$. The fit is shown in fig. A.7. The uncertainty of this value is clearly underestimating the real fluctuations observed in the figures above. To establish an upper limit of the Xenon leakage through the foil, the partial pressure is overestimated to be $10^{-8}\,\mathrm{mbar}$.

With a suction efficiency of $43\,\frac{\mathrm{L}}{\mathrm{s}}$ [Bon21a, p.15] this results in a leakage rate of $4.3 \cdot 10^{-7}\,\frac{\mathrm{mbar} \cdot \mathrm{L}}{\mathrm{s}}$ for the foil segment tested. Scaling this leakage rate with the area of the entrance window of $92\,\mathrm{cm} \times 92\,\mathrm{cm}$ yields a leakage rate of $3.8 \cdot 10^{-5}\,\frac{\mathrm{mbar} \cdot \mathrm{L}}{\mathrm{s}}$. This translates to a leakage rate of $1.35 \cdot 10^{-4}\,\frac{\mathrm{L}}{\mathrm{h}} = 135\,\frac{\mu\mathrm{L}}{\mathrm{h}}$ (using eq. (4.1)). The real leakage rate of the entrance window is expected to be below $135\,\frac{\mu\mathrm{L}}{\mathrm{h}}$, since this value is calculated as an upper limit. Furthermore, there are indications pointing towards a leakage in the membrane holder setup, which would further contribute to the partial pressure of Xenon within it.

Besides the check for Xenon tightness, the measurement can be used to get an estimate for the leakage of other gases through the entrance window.

Table 4.1: The partial pressure difference of different gases before and after membrane cutoff. The values are the result of constant fits over two minutes before the membrane cutoff and two minutes after a one-minute-break after membrane cutoff. The fits and determined partial pressures are shown in fig. A.8. The unexpected peaks at 29.6 min measurement time are neglected in the fits. Also shown are the suction efficiencies for the different gases ([Bon21a, p.15], [Vac22, p.3]) and the resulting leakage rates, scaled up by window area. The leakage rate is converted into liters per hour by means of eq. (4.1).

Gas	Partial Pressure Difference [mbar]	S_{eff} $[\frac{\text{L}}{\text{s}}]$	Leakage Rate
Argon	$(7.85 \pm 0.01) \cdot 10^{-7}$	66	$(16\,390 \pm 21)\,\frac{\mu\text{L}}{\text{h}}$
Hydrogen	$(1.37 \pm 0.04) \cdot 10^{-8}$	48	$(208 \pm 6)\,\frac{\mu\text{L}}{\text{h}}$
Helium	$(1.93 \pm 0.01) \cdot 10^{-8}$	58	$(354 \pm 2)\,\frac{\mu\text{L}}{\text{h}}$
Nitrogen	$(2.90 \pm 0.01) \cdot 10^{-5}$	67	$(615 \pm 2)\,\frac{\text{mL}}{\text{h}}$
Xenon	$(3.35 \pm 0.32) \cdot 10^{-9}$	43	$(46 \pm 4)\,\frac{\mu\text{L}}{\text{h}}$

The difference in partial pressure before and after membrane cutoff, estimated by a constant fit, combined with the suction efficiencies yields the desired results shown in table 4.1. The determined leakage rate for Xenon is far below the previously discussed upper limit. This is most likely due to the fact, that not the entire Xenon-amount in the setup is the basis of this calculation, but only the offset amount added by the membrane setup. Furthermore, the gases found in the setup are reflective of the air surrounding it, as can be seen in table 4.2. Since Xenon is extremely rare in air, the previous upper limit is the more conservative estimate. The leakage rate of other gases besides Xenon is of interest because these gases might leak into the gas system. The values found in table 4.1 do not have to be corrected for their respective concentration in air, because the module will be surrounded by air in the final setup for the CBM experiment.

Instead of the partial pressure, the relative pressure can be used to put the gas concentrations into context. The relative pressures shown are the ratio between partial pressure of the specific gas and the sum of all partial pressures measured for that time step.

Table 4.2 further points towards a leak in the membrane setup. Before the membrane cutoff, the ratio of residue Nitrogen and Oxygen is ≈3.72. This ratio is very close to the ratio in air of ≈3.73 [Dem15, p.206, Tab.7.4]. After the membrane cutoff, this ratio is ≈3.25. While the relative pressures shown in table 4.2 do not take into account the different suction efficiencies, the difference in ratio before and after the membrane cutoff still are pointing towards an air intake, since the suction efficiencies

Table 4.2: The relative pressures of different gases before and after membrane cutoff, determined by normalizing the measurement results by the sum of all partial pressures recorded. The values are the result of constant fits over two minutes before the membrane cutoff and two minutes after a one-minute-break after membrane cutoff. The fits are shown in fig. A.9. The unexpected peaks at $29.6\,\mathrm{min}$ measurement time are neglected in the fits. Also shown is the relative volume concentration of some of the gases in air [Dem15, p.206, Tab.7.4].

Gas	Rel. Press. Before [%]	Rel. Press. After [%]	Vol. Conc. [%]
Argon	1.433 ± 0.004	0.312 ± 0.002	0.934
Hydrogen	$(5.11 \pm 0.01) \cdot 10^{-2}$	0.786 ± 0.008	$5 \cdot 10^{-5}$
Helium	$(3.539 \pm 0.008) \cdot 10^{-2}$	$(1.42 \pm 0.05) \cdot 10^{-2}$	$5.2 \cdot 10^{-4}$
Nitrogen	52.9 ± 0.2	8.00 ± 0.01	78.084
Xenon	$(1.10 \pm 0.04) \cdot 10^{-2}$	0.14 ± 0.01	–
Oxygen	14.23 ± 0.03	2.46 ± 0.03	20.947
Water	18.6 ± 0.1	46.4 ± 0.2	–

do not change with connection of the membrane setup. The relatively low pressure percentage of Nitrogen, compared to the concentration in air, is the result of water and molecule fragments in the setup contributing to the total pressure in the system. Especially the high amount of water vapor contributes to the total pressure, shifting the relative partial pressure of Nitrogen towards the lower value shown in table 4.2. The drop of the Nitrogen-to-Oxygen ratio points towards a shift from a non-discriminatory leakage towards a smaller leakage, where molecule size and other processes are of major importance.

4.2   Expected Leakage Rate and Measurement Methods for CBM-TRD Modules

For the purpose of the CBM-TRD two kinds of leaks are of importance: diffusive leaks and viscous leaks, observed in the ALICE-TRD [18, p.96, sec.3.4.1]. Diffusive leaks allow gas to flow in and out of the module with little delay. Viscous leaks are high resistivity leaks, resulting in their impact not showing in other purity indicators such as Oxygen content at overpressure, as discussed in [Pit12, p.76f.].

To measure the total leakage rate two options are available for the purposes of the TRD: Measure the Oxygen content for both over- and negative pressure at a known gas flow, as discussed in [Pit12, p.77, eqs.5.9-5.12], or the overpressure test conducted for this thesis. The latter is chosen due to the more direct approach to the subject. The

test does not discriminate between diffusive and viscous leaks. And by using Argon, a gas similar to the Xenon used for the final modules, the leakage rates found by this setup should be closer to the leakage rates that would be found with Xenon.

To have an idea of the expected amount of leakage and the points of interest for leakage, one can compare to the similarly constructed MWPCs of the ALICE-TRD.

The MWPCs of the ALICE-TRD have a similar structure to the ones used in the CBM-TRD. The gas volume in both chamber types is enclosed by fiberglass-epoxy at the sides, an aluminized foil for an entrance window and a pad-plane on the back of the volume, as documented in [Cor01, p.22ff. Section 4.2]. All material transitions are managed by epoxy resin for both experiments. Besides these similarities it has to be noted, that there are some key differences between the modules. While the materials used are similar, the number of parts embedded in epoxy is different. The substructure of the pad-planes is not similar. The spatial dimensions of the modules differ, although they are in the same order of magnitude ($1100\,\text{mm} \times 956\,\text{mm}$ to $1605\,\text{mm} \times 1178\,\text{mm}$ for ALICE [Cor01, p.9, Table 2.2] vs. $99\,\text{cm} \times 99\,\text{cm}$ for CBM [BBE18, p.37]).

The ALICE-TRD has an average leak rate of $0.23\,\frac{\text{L}}{\text{h}}$ [Gar19, p.6]. This leakage is the combined loss of 540 [Cor01, p.5 Section 1.4] TRD modules in the ALICE-TRD. Therefor a single module accounts for $426\,\frac{\mu\text{L}}{\text{h}}$.

The volume of a CBM-TRD module is $9216\,\text{cm}^2 \times 1.2\,\text{cm} = 11\,059.2\,\text{cm}^3$ [BBE18, p.64 Table 5.2]. Approximating the gas as ideal and assuming a constant pressure of $1013\,\text{mbar}$ and a linear pressure decay, this leak rate would correspond to a decrease in pressure of $39\,\frac{\mu\text{bar}}{\text{h}}$. A realistic target resolution for this setup is $0.1\,\text{mbar}$. This sets the measurement duration for each measurement cycle to about $1\,\text{d}$.

As discussed in section 3.11, section 3.12 and section 4.3.6, this design premise is incomplete. The decay of the overpressure in the TRD is observed to be exponential in section 4.5, as expected from the relations shown in section 3.10 and section 3.11. While a linear decay might be observed for small leakage rates, as is done in section 4.4, the exponential decay is predominant in the observed leakage rate. The implications of these observations on the setup as a whole are discussed in section 4.3.6 and chapter 5.

4.3 Leakage Rate Measurement Setup
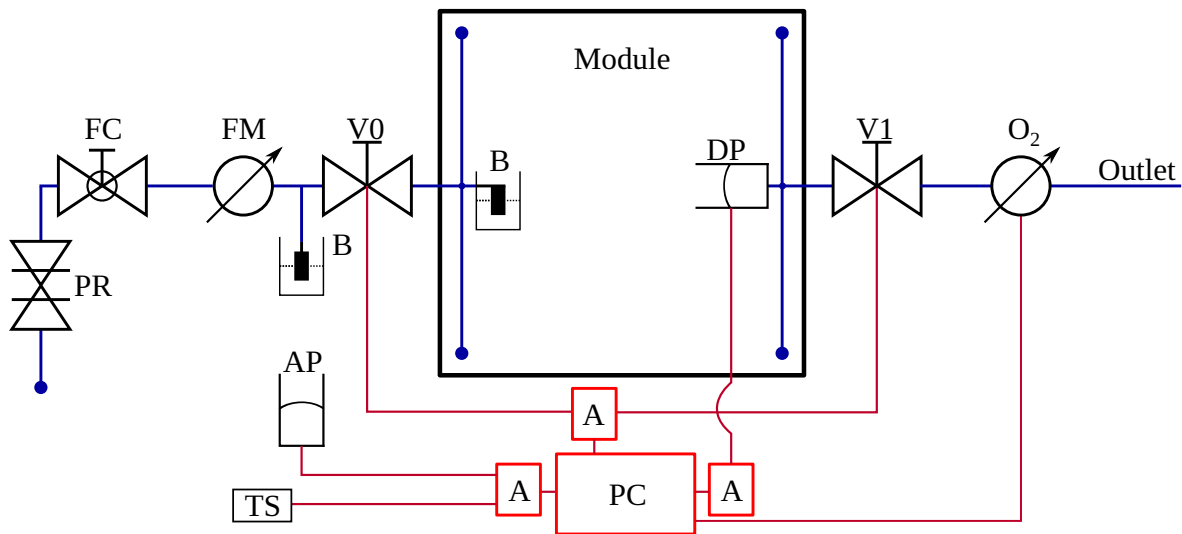
Figure 4.6: A sketch of the setup for the investigation of gas tightness of a TRD module. Gas connections are represented by blue lines, electrical ones by red lines. From left to right the abbreviations in the gas system stand for pressure reducer, flow controller, flow meter, bubbler, valve, TRD module, differential pressure sensor and Oxygen sensor. The abbreviations in the electrical component of the setup from left to right stand for temperature sensor, absolute pressure sensor, Arduino and PC.

The measurement of the gas tightness of a TRD module is conducted using the setup described in this section.

The idea for this test is simple. The module in question is filled with gas until a differential overpressure of about 1 mbar is reached. The module is then closed off at the gas in- and outlet. The decay of this overpressure over time is directly proportional to the leakage rate of the module.

This sets several requirements to the measurement setup. Since the TRD modules have a flexible entrance window, as described in section 3.8, the ambient pressure has to be monitored closely to be able to correct the development of differential pressure by ambient changes, if necessary.

Furthermore, it has been determined, that the maximum pressure the TRD modules can be exposed to without risking damage is 1 mbar. Since the safety of the chambers is of utmost importance, a bubbler, acting as a relief valve, set to 1 mbar ensures that no higher overpressure can be reached. The bubbler is discussed further in section 4.3.5.

To yield a quantitative leakage rate this measurement has to approximate the used gas (Ar/CO_2 82/18) as ideal, as motivated in section 3.9. This approximation works better

for noble gases than for air. Therefore, an Oxygen sensor is deployed. The measured Oxygen content serves as an indicator for gas purity.

Since changes in ambient pressure are a regular occurrence, one of the key aspects of this setup is that it is controlled by software running on a PC. This allows measurements overnight and several consecutive measurement cycles without the necessity of manual changes to the setup. This software is described in section 4.3.1.

With these conditions fulfilled, the setup consists of a pressure reducer, a flow controller, two controllable valves, a bubbler, two temperature sensors, one differential pressure sensor, one absolute pressure sensor, an Oxygen sensor, two Arduinos, a PC and the TRD module under investigation. The setup is sketched in fig. 4.6.

As shown in fig. 4.6, the pressure of the used gas, Ar/CO_2 82/18, is reduced from bottle pressure by a pressure reducer in a first step. The output-pressure is around 1.5 bar. A manually set flow controller limits the flow to a desired amount, the magnitude of which is depending on the ongoing measurement. The flow controller is followed up by a digital flow meter. This flow meter is used during setup to set the flow to a desired order of magnitude. Since the flow is controlled manually, while the rest of the setup is automated, a bubbler releases excess gas to the room during measurement cycles when valve 0 is closed. This prevents the buildup of a critical overpressure in the gas system upstream of the first valve. The valves in this setup are controlled by pressured air, at a pressure of 4 bar, which in turn is controlled by pneumatic valves. These pneumatic valves are controlled by an Arduino which is connected to the PC. Further details can be found in appendix A.4.2.

Downstream of the first valve, the chamber under investigation is connected. A bubbler is attached to the gas line at the gas inlet of the chamber with some distance to it. A rise in ambient pressure without reaction of the software could cause a negative differential pressure. Under these circumstances, the atmospheric pressure could push oil up the bubbler into the gas system. Said distance is a safety measure and provides additional volume, in which oil from the bubbler can flow into, in case off such an unpredicted setup failure. On the outlet of the chamber the differential pressure sensor is connected. This sensor is described in section 4.3.2 and transmits the measurement results using 4 mA to 20 mA-signals to a second Arduino connected to the computer. The gas outlet is controlled by a second valve downstream of the chamber. This valve is again connected to the computer via an Arduino, which controls a relay. The relay controls the pneumatic valves that control the gas valves, V0 and V1.
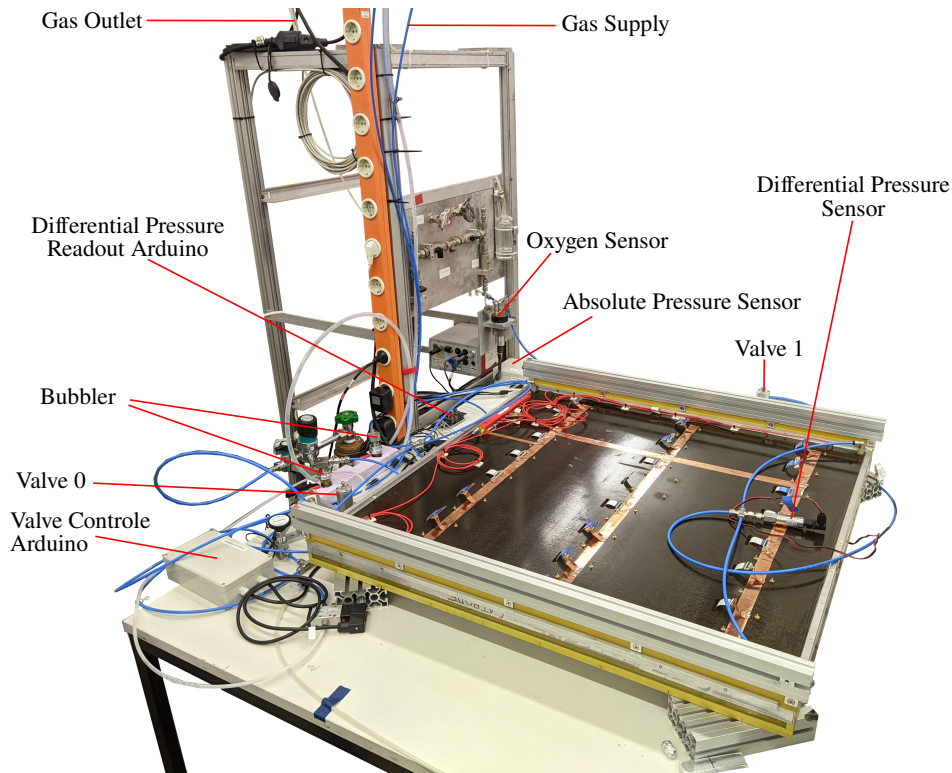
Figure 4.7: A commented picture of the measurement setup. All visible components mentioned in fig. 4.6 are highlighted. The gas bottle, the flow controller and the flow meter are close to a wall to the left of this photo. The computer is in the base of the rack.

The last gas sensor upstream of the gas outlet is the Oxygen sensor described in section 4.3.4.

As mentioned before, an absolute pressure sensor connected to the PC monitors the ambient pressure. This sensor is enclosed in a case with a temperature sensor. The latter is necessary to get an approximation of the uncertainty of the absolute pressure reading. A picture of the setup is shown in fig. 4.7.

4.3.1 Readout Software

The readout software, that controls the measurement setup serves four major functions: To protect the investigated chamber module during the measurement, to set up new measurements automatically, to log the data obtained during the measurements and to indicate the source of error if one occurs.

To serve these functions the software can be sectioned into three main parts:

1. The **initial setup** of the program establishes connection to the Arduinos and the Oxygen sensor. In this stage, the software assigns the devices to the respective directory on the computer. If any connection can not be established, the program terminates displaying an error message. If the messages received from the devices do not fulfill certain quality checks, e.g. message length, the program is terminated with an error message displayed on screen. Once the connection to all connected devices of the setup is established, one of two cases is to be considered.

2. In case a **measurement is already ongoing**, the program is checking if the differential pressure is within the allowed boundaries, namely 0 mbar to 1 mbar. If this is the case, the software continues the readout cycle without further action. If ten measurement points, corresponding to about twenty seconds time, are beyond the threshold of 1 mbar the software opens the valves and terminates the program with an error message concerning the bubbler configuration.

   In case that thirty measurement points are below or equal to the lower bound of 0 mbar differential pressure the measurement is completed and the program begins a new measurement. This is the second case for the program.

3. A **new measurement** is initiated by opening the valves. The measured Oxygen content is monitored to ensure gas purity. Once the Oxygen content is below 100 ppmV for three consecutive measurement points valve 1, V1 in fig. 4.6, downstream of the module, is closed. Once the overpressure is in the targeted range of 0.9 mbar to 1 mbar, valve 0, V0 in fig. 4.6, upstream of the chamber, is closed. This concludes the initiation of a new measurement cycle. If the targeted overpressure can not be reached, for example due to bad bubbler configuration, the measurement is aborted by opening both valves and terminating the program with an error displayed on screen.

A flow diagram of the program is shown in fig. 4.8.
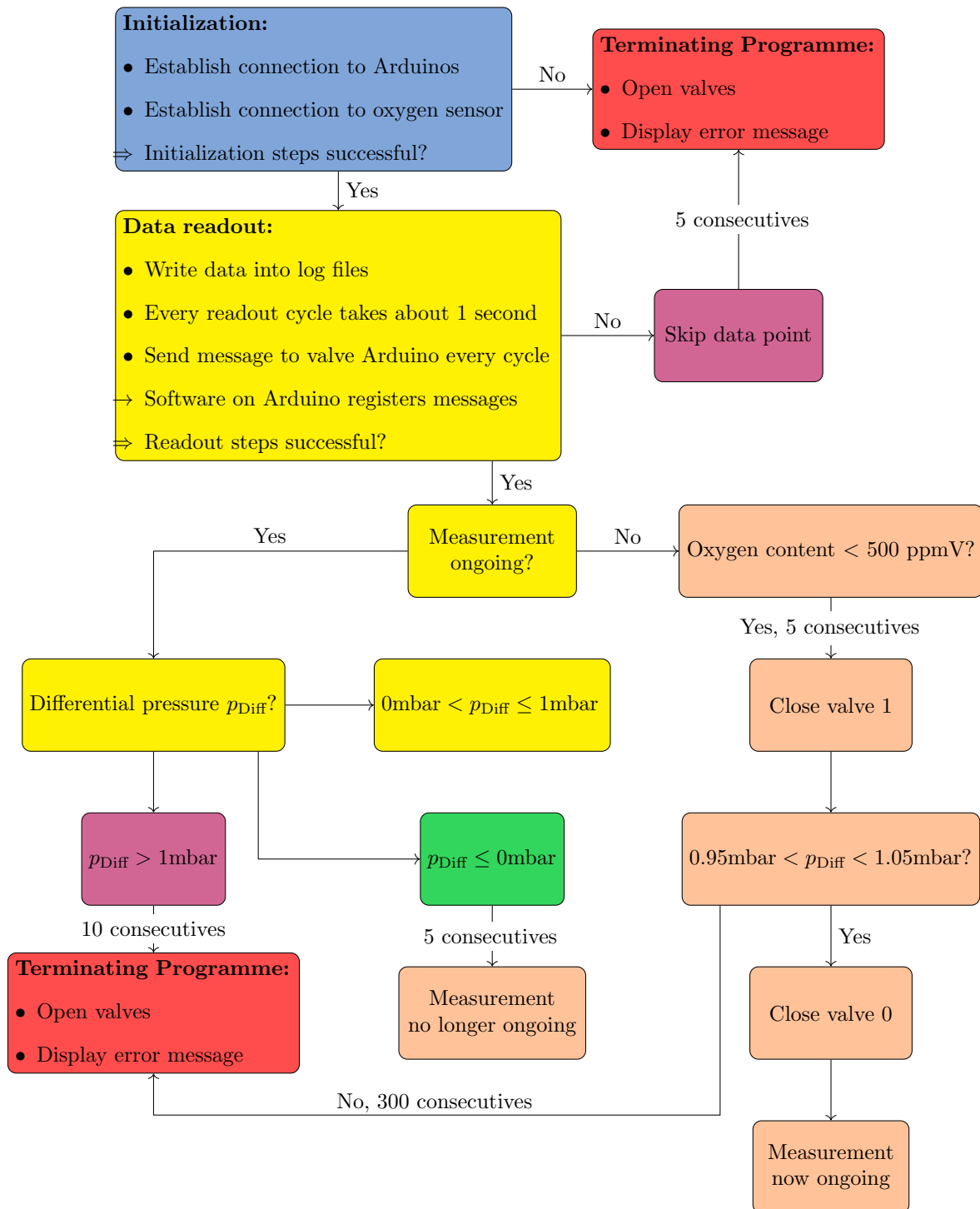
Figure 4.8: A flowchart of the readout software. If the condition specified on an arrow is not met, the program continues with the next data readout step. The software starts at the blue initialization box. Yellow boxes mark parts of a standard readout loop, where no further action is necessary. Start up of a new measurement within the program still running is content of the orange boxes. In case of critical error, the red boxes specify the actions undertaken by the program to abort the measurement safely. Purple boxes mark suboptimal conditions, which when reached consecutively lead to a termination of the program. Finally, the green box marks the successful end of a measurement.

4.3.2 Differential Pressure Sensor

The differential pressure sensor measures the difference in pressure between two sides. The model used in this setup is a *CTEM7N010GQ4* by *First Sensor AG*, the measurement interval of which ranges from $-10\,\mathrm{mbar}$ to $10\,\mathrm{mbar}$. Readout of this sensor is conducted via $4\,\mathrm{mA}$ to $20\,\mathrm{mA}$ current signal, which is digitized by an Arduino Uno equipped with a suitable shield with a $9\,\mathrm{bit}$ resolution.

Principle of Operation

This sensor operates using silicon based piezoresistive pressure sensors [AGb]. The resistances of these piezo modules are dependent on the strain applied to them. In case of these differential pressure sensors, a connected silicon membrane deformed by the difference in pressure puts strain on the piezo modules, as shown in fig. 4.9. This links their resistances to the differential pressure [Niea]. The details of the connection between membrane and piezoresistive module are not public for the sensor used in this setup. Since the piezo modules resistances also depend on the temperature, the sensor compensates for changes in temperature automatically.
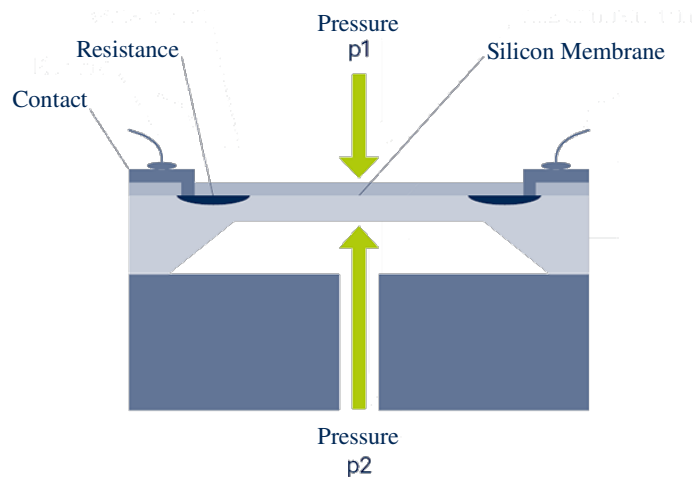
Figure 4.9: A sketch of a piezoresistive pressure sensor [Niea, translated]. The resistances are arranged in a Wheatstone bridge.

Uncertainties

The accuracy of the chosen sensor is specified in [AGa, p.2]. Span and offset temperature dependence accounts to $u_{\mathrm{TSpan}} = \pm 0.004\,\frac{\mathrm{mbar}}{^\circ\mathrm{C}}$ and $u_{\mathrm{TOffset}} = \pm 0.002\,\frac{\mathrm{mbar}}{^\circ\mathrm{C}}$ referring to a temperature of $25\,^\circ\mathrm{C}$. It is not expected for this temperature dependence to impact the measurement significantly, since the changes due to it are systematic in nature

and about 50 times smaller than the targeted pressure resolution of 0.1 mbar. Non-linearity and hysteresis add another $u_{\mathrm{NL}} = \pm 0.04$ mbar of uncertainty, split throughout the entirety of the measurement range. Since only a small fraction of said range is used in this setup (-0.1 mbar to 1.1 mbar for the measurement with a TRD-chamber), it is plausible that the uncertainty due to non-linearity and hysteresis is smaller for this measurement. Long term stability, output noise and repeatability account for additional $u_{\mathrm{LTS}} = \pm 0.1$ mbar, $u_{\mathrm{Noise}} = \pm 0.02$ mbar and $u_{\mathrm{Rep}} \pm 0.04$ mbar. The latter two of which are the most relevant for this measurement, since the long term stability describes the change in measurement output after 1 year. This is partially accounted for by setting the zero-point according to current output at zero differential pressure. This true zero differential pressure is achieved by leaving the pressure sensor open at both sides of the sensor, while measuring the output current. This method does not fully compensate the ageing of the sensor, but since this measurement setup operates in close proximity to this true zero, the long term stability is neglected in the analysis of the data. The power supply used to supply the sensor with power has an output voltage of 12 V. This adds another uncertainty of $u_{\mathrm{PSOffset}} = \pm 0.006$ mbar and $u_{\mathrm{PSSpan}} = 0.012$ mbar. Additional to the sensors intrinsic uncertainty, the readout adds another digitization error. Assuming a rectangular distribution of the readout data yields a digitization error of approximately $u_{\mathrm{ADC}} = \pm 0.02$ mbar.

The total uncertainty adds up to

$$
\begin{aligned}
u_{\mathrm{DP}}^2(\Delta T) = {}& u_{\mathrm{TSpan}}(\Delta T)^2 + u_{\mathrm{TOffset}}(\Delta T)^2 + u_{\mathrm{NL}}^2 \\
& + u_{\mathrm{Noise}}^2 + u_{\mathrm{Rep}}^2 + u_{\mathrm{ADC}}^2 + u_{\mathrm{PSOffset}}^2 + u_{\mathrm{PSSpan}}^2 \\
= {}& \left(0.004\,\frac{\mathrm{mbar}}{^\circ\mathrm{C}}\Delta T\right)^2 + \left(0.002\,\frac{\mathrm{mbar}}{^\circ\mathrm{C}}\Delta T\right)^2 + (0.04\,\mathrm{mbar})^2 \\
& + (0.02\,\mathrm{mbar})^2 + (0.04\,\mathrm{mbar})^2 + (0.02\,\mathrm{mbar})^2 + (0.006\,\mathrm{mbar})^2 + (0.012\,\mathrm{mbar})^2
\end{aligned}
$$

$$
u_{\mathrm{DP}}(\Delta T) = \sqrt{\left(0.004\,\frac{\mathrm{mbar}}{^\circ\mathrm{C}}\Delta T\right)^2 + \left(0.002\,\frac{\mathrm{mbar}}{^\circ\mathrm{C}}\Delta T\right)^2 + 0.004\,18\,\mathrm{mbar}^2}. \tag{4.2}
$$

where ΔT is the temperature difference to 25 $^\circ$C.

4.3.3 Absolute Pressure and Temperature Sensor

The absolute pressure sensor measures the absolute pressure within the measurement range of $800\,\text{mbar}$ to $1100\,\text{mbar}$. The model used in this setup is a *First Sensor 144SC0811BARO*, shown in fig. 4.10. The sensor is housed in a plastic casing with two inlets and is temperature compensated. The inlets are left open in this setup. The sensor output is realized by a $0\,\text{V}$ to $5\,\text{V}$ analog signal. This signal is readout using a $16\,\text{bit}$ Analog-to-Digital Converter (ADC) connected to an Arduino. The ADC used for this sensor is an *ADS1115*. It is set to sample an interval of $-6.144\,\text{V}$ to $6.144\,\text{V}$, which is the closest available range to the needed interval of $0\,\text{V}$ to $5\,\text{V}$. Each bit of the output therefore corresponds to $2 \cdot 6.144\,\text{V}/2^{16} = 0.1875\,\text{mV}$. This output is communicated to an Arduino using an I^2C bus.

A temperature sensor is enclosed in the external housing of the pressure sensor. This sensor is used to monitor the ambient temperature and to estimate additional uncertainties due to changes in temperature. An *LM75* sensor by *National Semiconductor* is chosen. This model also communicates with the same Arduino using the I^2C bus. The Arduino is connected to the PC and returns the measurement outcomes, if pinged by the PC. This is motivated in appendix A.4.1. More details for this sensor are referenced in appendix A.4.3.
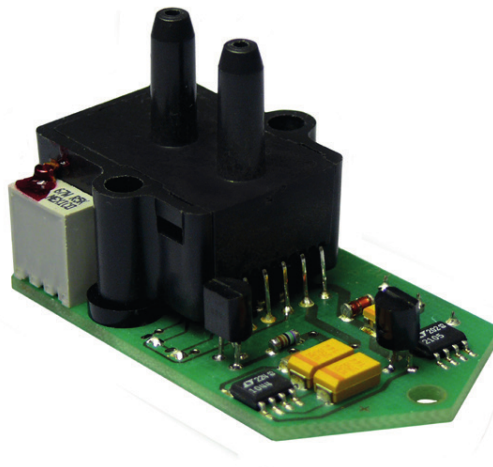
Figure 4.10: A picture of the absolute pressure sensor [20, p.1]. The black pipes lead to the pressure sensor.

Principle of Operation

The operation principle of this particular sensor is not documented publicly by *First Sensor AG*. However, there is some information to be gained from the *First Sensor AG*-webpage. Absolute pressure sensors use a vacuum reference to operate [Nieb] (see fig. 4.11). The vacuum has to be sufficiently high, meaning sufficiently low pressure, to be negligible compared to the pressure to be measured [Nieb].

A similar setup to the one described in section 4.3.2 could be employed to translate the deformation of a membrane into an absolute pressure.
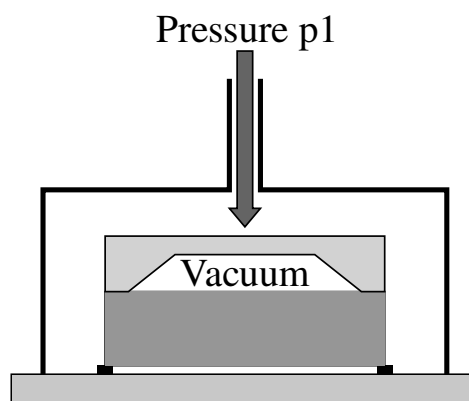
Figure 4.11: A schematic drawing of a *First Sensor AG* pressure sensor [Nieb, modeled on Bild 2, translated]. The sensor structure is similar to the one shown in fig. 4.9.

Uncertainties

For the pressure sensor the combined non-linearity and hysteresis lead to a typical uncertainty of $u_{\text{NL}} = \pm 0.15\,\text{mbar}$, as specified by *First Sensor AG* in [20, p.3]). This systematic uncertainty is of no mayor importance for changes in ambient pressure during the measurement, because only small parts of the measurement range are reached each cycle. Calculating the difference between a presssure reading at the beginning of a cycle and the reading during the cycle evens out this error. The typical temperature stability is $u_{\text{TOffset}} = \pm 0.015\,\frac{\text{mbar}}{°\text{C}}$ for the offset and $u_{\text{TSpan}} = \pm 0.03\,\frac{\text{mbar}}{°\text{C}}$ for the span (see [20, p.3]), referring to a temperature of $25\,°\text{C}$. But since these uncertainties are again systematic in nature, only the additional uncertainties due to temperature changes after the start of a new measurement cycle need to be added for the change in ambient pressure during a measurement cycle. Due to the short timescales of these measurements, the long term stability of $u_{\text{LTS}} = \pm 0.3\,\text{mbar}$ is neglected completely in the analyses.

For the absolute pressures measured, the power supply rejection has to be taken into account. For a supply voltage greater than 8 V, offset and span vary by $u_{\text{PSOffset}} = \pm 0.15 \frac{\text{mbar}}{\text{V}}$ and $u_{\text{PSSpan}} = \pm 0.09 \frac{\text{mbar}}{\text{V}}$ respectively. Since the voltage supplied to the setup is 9 V, the uncertainty totals to $u_{\text{PS}} = \pm 0.17\,\text{mbar}$ for the absolute pressure readings. For changes in ambient pressure, this uncertainty evens out.

Besides the uncertainties stemming from the pressure sensor, the digitization of the measurement output contributes a small uncertainty. Since one bit corresponds to $0.011\,25\,\text{mbar}$, a rectangular distributed uncertainty of $u_{\text{ADC}} = \pm \frac{0.011\,25\,\text{mbar}}{2\sqrt{3}}$ is added. The total systematic uncertainty for the change in ambient pressure during a measurement cycle is

$$
\begin{aligned}
u_{p\text{Diff}}(\Delta T_{\text{Cycle}}) &= \sqrt{2u_{\text{ADC}}^2 + \left(\Delta T_{\text{Cycle}} \cdot u_{\text{TOffset}}\right)^2 + \left(\Delta T_{\text{Cycle}} \cdot u_{\text{TSpan}}\right)^2} \\
&= \sqrt{2\left(\frac{0.011\,25\,\text{mbar}}{2\sqrt{3}}\right)^2 + \left(\Delta T \cdot 0.034\,\frac{\text{mbar}}{{}^\circ\text{C}}\right)^2}.
\end{aligned}
\tag{4.3}
$$

ΔT_{Cycle} is the temperature difference between ambient temperature at the time of data point acquisition and temperature at the beginning of the measurement cycle.

The absolute pressure readings have a combined uncertainty of

$$
\begin{aligned}
&u_p(\Delta T) \\
&= \sqrt{u_{\text{ADC}}^2 + \left(\Delta T u_{\text{TOffset}}\right)^2 + \left(\Delta T u_{\text{TSpan}}\right)^2 + u_{\text{NL}}^2 + u_{\text{PSOffset}}^2 + u_{\text{PSSpan}}^2} \\
&= \sqrt{\left(\frac{0.011\,25\,\text{mbar}}{2\sqrt{3}}\right)^2 + \left(\Delta T \cdot 0.034\,\frac{\text{mbar}}{{}^\circ\text{C}}\right)^2 + (0.15\,\text{mbar})^2 + (0.17\,\text{mbar})^2}
\end{aligned}
\tag{4.4}
$$

In this formula ΔT is the difference between ambient temperature and $25\,{}^\circ\text{C}$.

For the temperature sensor the accuracy is specified to be $2\,{}^\circ\text{C}$ for the temperature interval in question ($-25\,{}^\circ\text{C}$ to $100\,{}^\circ\text{C}$) [96]. The sensor outputs the temperature in $0.5\,{}^\circ\text{C}$-steps. The total uncertainty of the temperature reading sums up to

$$
u_T = \sqrt{(2\,{}^\circ\text{C})^2 + \left(\frac{0.5\,{}^\circ\text{C}}{2\sqrt{3}}\right)^2} \approx 2\,{}^\circ\text{C}.
\tag{4.5}
$$

ADC Correction

The ADC used to digitize the pressure sensor signal is prone to error. In rare instances, a jump in ADC-output is observed. To filter out these instances, a continuity condition is exerted onto the data. If the ADC-output changes in a manner that would allege a

change in ambient pressure of above 30 mbar within the time between two measurement points of about 1 s, the ADC-value is dismissed.

4.3.4 Oxygen Sensor

The Oxygen sensor measures the Oxygen content of the gas flowing through the setup. The model chosen in this setup is a *Hach Orbisphere 510* with an electrochemical sensor. The sensor can measure Oxygen content from a few ppmV up to atmospheric Oxygen level. A temperature sensor and a pressure sensor are included in the sensor housing and the Oxygen sensor is temperature compensated [09, p.16]. The *Orbisphere* has several output options available. In this particular setup RS485 digital communication is used to relay the outputs to the PC.

Since the Oxygen content only serves as a benchmark for gas purity and is not of quantitative importance for this measurement the uncertainty is neglected.

The accuracy of the temperature sensor is not specified in the manual of the sensor ([09]). Since the temperature reading of the instrument is output in 0.1 °C-steps, the minimal uncertainty can be described by

$$u_{\mathrm{T}Orbi} = \frac{0.1\,^{\circ}\mathrm{C}}{2\sqrt{3}} \approx 0.03\,^{\circ}\mathrm{C}. \tag{4.6}$$

This value most likely underestimates the systematic uncertainty. Due to lack of information, an uncertainty of 0.5 °C is assigned to the temperature reading of the *Orbisphere*:

$$u_{\mathrm{T}Orbi} = 0.5\,^{\circ}\mathrm{C}. \tag{4.7}$$

Principle of Operation

This Oxygen sensor operates by chemically splitting Oxygen molecules using electrolysis, as described in [09, p.15f. section 3.2]. Its inner construction is shown in fig. 4.12. The gas flow is directed to pass by a membrane which allows a proportion of Oxygen to pass through it. On the other side of the membrane there is a solution of electrolyte in which the Oxygen dissolves. A voltage is applied to anode and cathode submerged in said solution. The dissolved Oxygen causes a reaction at the cathode, leading to a

measurable current. This current is proportional to the Oxygen content in the electrolyte, which is proportional to the partial pressure of Oxygen in the gas passing by the membrane [09, p.15f. section 3.2].
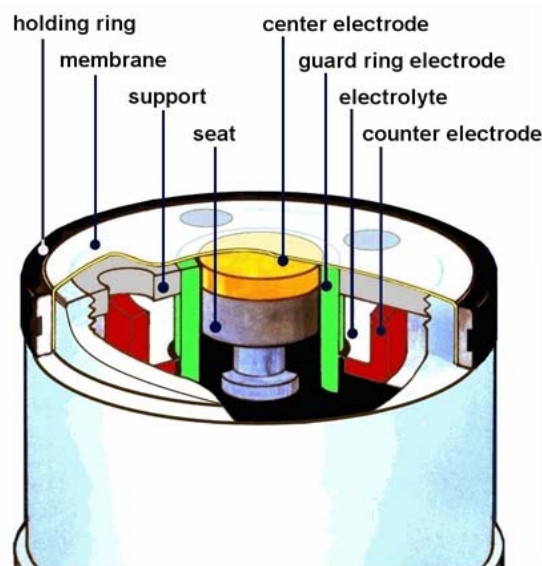
Figure 4.12: A schematic drawing of the Oxygen sensor [09, p.15, Figure 3]. The center electrode (orange) is the cathode, the counter electrode (red) is the anode. The guard ring electrode (green) reduces the impact of other gases on the reading . The membrane (light gray) allows the passing of Oxygen into the sensor. The remaining named parts ensure the structural integrity of the sensor (see [09, p.15f., section 3.2]).

4.3.5 Bubbler

To ensure that no chamber damaging overpressure can be applied to the module gas bubblers are employed in the setup. The bubblers used in this setup were designed by Daniel Bonaventura and Felix Fidorra.

Principle of Operation

A bubbler is – for the purposes of this thesis – a pipe inserted vertically into a liquid. Typically, that liquid is a mineral oil. The gas system gets connected to the vertical pipe. If there is an overpressure present in the gas system, the gas displaces the oil in the pipe. To escape from the pipe through the liquid, the gas has to overcome the hydrostatic pressure of the displaced oil at depth of penetration. The oil used for the bubblers in this setup is *Leybold*'s *DIFFELEN normal* diffusion pump oil.
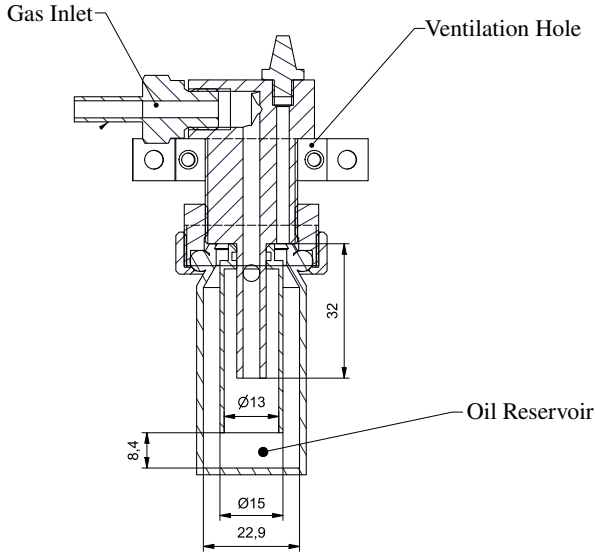
Figure 4.13: A technical drawing of the bubbler used in this setup [Bon21b, translated]. The dimensions are noted in millimeters. The decimal markers are commas instead of points. The oil reservoir is filled with *DIFFELEN normal* by *Leybold*. Noticeably the dimensions of the pipe inserted into the oil are larger than the gas line diameter.

Calibration

Different factors, besides the initial oil level above the end of the inserted pipe h_{start}, contribute to the set pressure threshold. Since the cross-section area inside the pipe is not negligible compared to the cross-section area outside the pipe, the additional hydrostatic pressure of the displaced oil has to be taken into account, as is motivated in the sketch below. With the dimensions from fig. 4.13 the additional oil level gained due to displaced oil can be calculated. If the entire pipe that was inserted into the oil at depth h_{start} gets filled with gas, the oil level rises to:

$$
h_{\text{oil}} = h_{\text{start}} + \frac{h_{\text{start}} A_{\text{in}}}{A_{\text{out}}}
$$
$$
\approx 1.56 h_{\text{start}}
$$
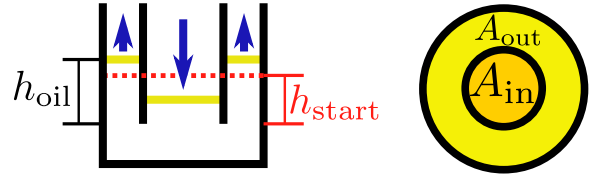
where A_{in} and A_{out} are the areas inside and outside the inserted pipe.

The pressure threshold is given by the hydrostatic pressure of *DIFFELEN normal* at h_{oil} [Dem15, p.165, sec.6.3.2.2, eq. 6.31]:

$$
p_{\text{th}} = g \varrho_{\text{DIF}} h_{\text{oil}} \approx 9.81 \, \frac{\text{m}}{\text{s}^2} \cdot 868 \, \frac{\text{kg}}{\text{m}^3} \cdot 1.56 h_{\text{start}} \approx 13\,286 \, \frac{\text{N}}{\text{m}^3} h_{\text{start}} \tag{4.8}
$$

where g is the gravitational acceleration [Bun, 51.9607°, 60 m] and ϱ_{DIF} is the density of *DIFFELEN normal* at 20 °C [19, p. 22, LVO 500].

Due to the comparatively high viscosity of *DIFFELEN normal*, the volume of the gas bubble created at the end of the pipe inserted in the oil will also have an impact on

the threshold-setting. The additional volume of oil displaced by the bubble increases the threshold as shown in the sketch above.

A measurement is conducted where different oil levels h_{start} are set and the resulting break-through differential pressure is measured. The setup uses a simplified version of fig. 4.6, where no TRD-module is connected. The module in- and outlet connectors are directly connected to each other. The flow is set below $3\,\frac{\text{L}}{\text{h}}$. Valve 1, downstream of the differential pressure sensor, is closed.

The oil level is measured with a tape measure. Since the *DIFFELEN* adheres to the glass of the bubbler, the oil level is hard to read, leading to the large uncertainties shown in fig. 4.14. Because these bubblers are commonly used and the outcome therefore is of some interest, the measurement results are summarized briefly here.
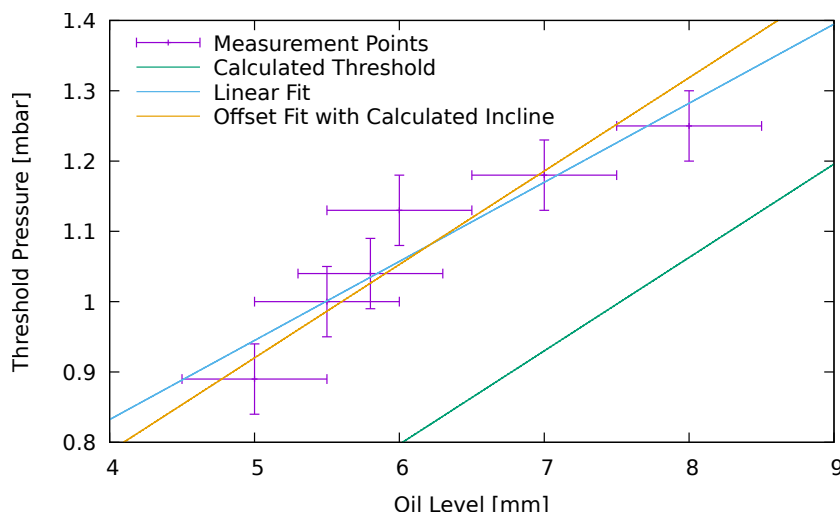
Figure 4.14: Different oil levels and the respective observed threshold pressure. Thermal effects are not taken into account for the uncertainty of the threshold pressure. The uncertainty of the oil level readings result from the oil clinging to the glass of the oil reservoir, obstructing the view on the oil levels. The offset between the thresholds calculated using eq. (4.8) (green line) and the measurement points is clearly visible. Fitted to the data is a linear function (blue line). A graph with the same incline as the calculated threshold and a fitted offset is shown (yellow line).

As can be seen in fig. 4.14, an expected offset is visible between the measurement points and the calculated pressure threshold of eq. (4.8). If the calculated incline, determined in eq. (4.8), is used, the resulting offset-parameter in the linear fit is $(0.26 \pm 0.02)\,\text{mbar}$, represented by the yellow line in fig. 4.14. The agreement between this approach and the measurement data is not perfect, but reasonable.

The linear fit, where the incline is adjustable, yields a slope of $(0.11 \pm 0.02)\,\frac{\text{mbar}}{\text{mm}}$. The

offset is determined to be $(0.38 \pm 0.13)\,\text{mbar}$. This offset is higher than expected, since it implies, that the gas bubble at the end of the pipe displaces $\approx 1\,\text{mL}$ of oil. Implying a sphere-shaped bubble, the bubble radius would be $6.2\,\text{mm}$. This is not consistent with observations. The difference in incline between $0.13\,\frac{\text{mbar}}{\text{mm}}$ calculated in eq. (4.8) and the fitted value of $(0.11 \pm 0.02)\,\frac{\text{mbar}}{\text{mm}}$ can in part be explained by oil residue remaining in the pipe. Not all the oil located in the pipe at the beginning of the measurement is displaced by the gas.

Regardless of the discussed differences between the model and the measurement, the linear fit is within the errors of the offset line resulting from eq. (4.8). Both models are sufficient to set a bubbler according to the needs of a setup. For the final setup, the bubbler is set to a starting height h_{start} of $5.5\,\text{mm}$, resulting in an overpressure threshold of $1\,\text{mbar}$.

4.3.6 Resolution of the Setup

The resolution of this setup is not limited by the minimum pressure steps resolved by the differential pressure or ambient sensor, but by the reasonable measurement time. As discussed in section 3.11, the volume leakage rate is related to the decay parameter λ by eq. (3.11). Assuming the leakage rate in section 4.2 is at an overpressure of $1\,\text{mbar}$, eq. (3.11) yields

$$0.426\,\frac{\text{mL}}{\text{mbar} \cdot \text{h}} = \lambda(\frac{V_0}{p_{\text{Amb}}} + B).$$

With $B = 371\,\frac{\text{mL}}{\text{mbar}}$, derived in section 3.12, $p_{\text{Amb}} = 1013\,\text{mbar}$ and $V_0 = 10\,156.8\,\text{mL}$ this leads to a decay parameter of

$$\lambda = 0.0011\,\frac{1}{\text{h}}.$$

The uncertainties of the values are neglected, since this is an order of magnitude estimation. The time to decay to half of the overpressure at the beginning of the measurement is given by

$$t_{\text{half}} = \frac{\ln(0.5)}{-\lambda} = 620\,\text{h}. \tag{4.9}$$

This measurement time is not realistic for this setup, because changes in ambient temperature and pressure would have a noticeable impact on the measurement outcome.

Limiting the measurement time at $24\,\mathrm{h}$ in which a decay to half the starting overpressure is to take place yields a decay parameter of

$$\lambda = 0.03\,\frac{1}{\mathrm{h}}.$$

Transforming this into a leakage rate by means of eq. (3.11) yields a minimum resolvable leakage rate of

$$F_{V\mathrm{max}} = 11.43\,\frac{\mathrm{mL}}{\mathrm{mbar}\cdot\mathrm{h}}.$$

 To get an estimation of the upper limit of the chamber leakage, measuring only a fraction of the pressure decay might be discussed.

As observed in section 4.4, the overpressure might decay linearly instead of exponentially for small module leakages. Furthermore, if only the first fraction of an exponential decay is analyzed, the evolution can be approximated by a linear function. This is a trivial consequence of the Taylor expansion of an exponential decay.

Inserting eq. (3.6) and a linear pressure decay

$$p(t) = \Delta p_0 - \eta t + p_{\mathrm{Amb}} \tag{4.10}$$

where η is a decay parameter determined by a linear fit to the data, into the ideal gas equation eq. (3.3) yields

$$(\Delta p_0 V_0 - \eta t + p_{\mathrm{Amb}})(V_0 + B(\Delta p_0 - \eta t)) = N(t)k_{\mathrm{B}}T_{\mathrm{Amb}}. \tag{4.11}$$

The pressure only decays until it reaches ambient pressure. The maximum time, that can be inserted into the expression above is therefore $t_{\mathrm{max}} = \frac{\Delta p_0}{\eta}$.

Solving eq. (4.11) towards the particle number $N(t)$ yields

$$N(t) = (\eta^2 t^2 B - \eta t(2B\Delta p_0 + V_0 + p_{\mathrm{Amb}}B) + (V_0 + \Delta p_0 B)(p_{\mathrm{Amb}} + \Delta p_0))/(k_{\mathrm{B}}T_{\mathrm{Amb}}). \tag{4.12}$$

The particle leakage is therefore

$$\dot{N}(t) = \frac{2\eta^2 tB - \eta(2B\Delta p_0 + V_0 + p_{\mathrm{Amb}}B)}{k_{\mathrm{B}}T_{\mathrm{Amb}}}. \tag{4.13}$$

The maximum contribution of the first term in this expression is reached for $t = t_{\mathrm{max}}$ and is $2\eta\Delta p_0 B/(k_{\mathrm{B}}T_{\mathrm{Amb}})$. This contribution is negligible compared to the last term of the constant contribution $-\eta p_{\mathrm{Amb}}B/(k_{\mathrm{B}}T_{\mathrm{Amb}})$, since $\Delta p_0/p_{\mathrm{Amb}} \approx 0.001$. Additionally, $t = t_{\mathrm{max}}$ is not reached, if only a fraction of the overpressure decay is measured, making the approximation even better. The resulting approximation for the particle leakage is then given by

$$\dot{N} = -\eta\frac{2B\Delta p_0 + V_0 + p_{\mathrm{Amb}}B}{k_{\mathrm{B}}T_{\mathrm{Amb}}}. \tag{4.14}$$

Transforming this particle leakage rate into a volume leakage rate F_{VL}, using the ideal gas equation, eq. (3.3), as is done for eq. (3.11), yields

$$F_{\mathrm{VL}} = \eta\frac{2B\Delta p_0 + V_0 + p_{\mathrm{Amb}}B}{p_{\mathrm{Amb}}}. \tag{4.15}$$

To determine the decay parameter η, at the very least three distinct overpressure ADC-steps have to be reached within the maximum measurement time of $24\,\mathrm{h}$. The 9-bit ADC used for the differential pressure sensor in this setup results in overpressure ADC-steps of $\approx 0.04\,\mathrm{mbar}$, as discussed in section 4.3.2. The resulting minimal determinable decay rate is

$$\eta_{\mathrm{MD}} = \frac{3 \cdot 0.04\,\mathrm{mbar}}{24\,\mathrm{h}} = 0.005\,\frac{\mathrm{mbar}}{\mathrm{h}} \tag{4.16}$$

resulting in a volume leakage of

$$\begin{aligned}
F_{\mathrm{VLmin}} &= 0.005\,\frac{\mathrm{mbar}}{\mathrm{h}} \cdot \frac{2B\Delta p_0 + V_0 + p_{\mathrm{Amb}}B}{p_{\mathrm{Amb}}} \\
&\approx 0.005\,\frac{\mathrm{mbar}}{\mathrm{h}} \cdot \frac{2 \cdot 371\,\frac{\mathrm{mL}}{\mathrm{mbar}} \cdot 0.95\,\mathrm{mbar} + 10\,157\,\mathrm{mL} + 1013\,\mathrm{mbar} \cdot 371\,\frac{\mathrm{mL}}{\mathrm{mbar}}}{1013\,\mathrm{mbar}} \\
&\approx 1.9\,\frac{\mathrm{mL}}{\mathrm{h}}
\end{aligned}$$

The values for the variables are put in disregarding their uncertainties. The minimal determinable upper limit of $1.9\,\frac{\mathrm{mL}}{\mathrm{h}}$ is still about a factor five higher than the expected leakage rate discussed in section 4.2. This limit could be lowered by increasing the digitization resolution of the differential pressure sensor. The implications of this limit are further discussed in chapter 5.

4.4 Offset Leakage Measurement

To distinguish the leakage rate of the TRD chamber from the leakage rate of the setup, the latter is measured. For this purpose, overpressure decay measurements are conducted on the setup described in section 4.3 without the TRD module in place. Instead of the chamber, I-connectors connect the in- and outlet directly. These I-connectors use the same type of connection as the chamber. Therefore, they are also expected to void the impact of the outdated connectors used for the module under investigation.

The inner bubbler installed next to the module in section 4.3 is also omitted. For the offset measurement, this bubbler is replaced by a plug. This is done to account for changes in ambient pressure more easily. With the bubbler present, the effect of changes in ambient pressure is significantly dampened. This is shown in fig. 4.15.
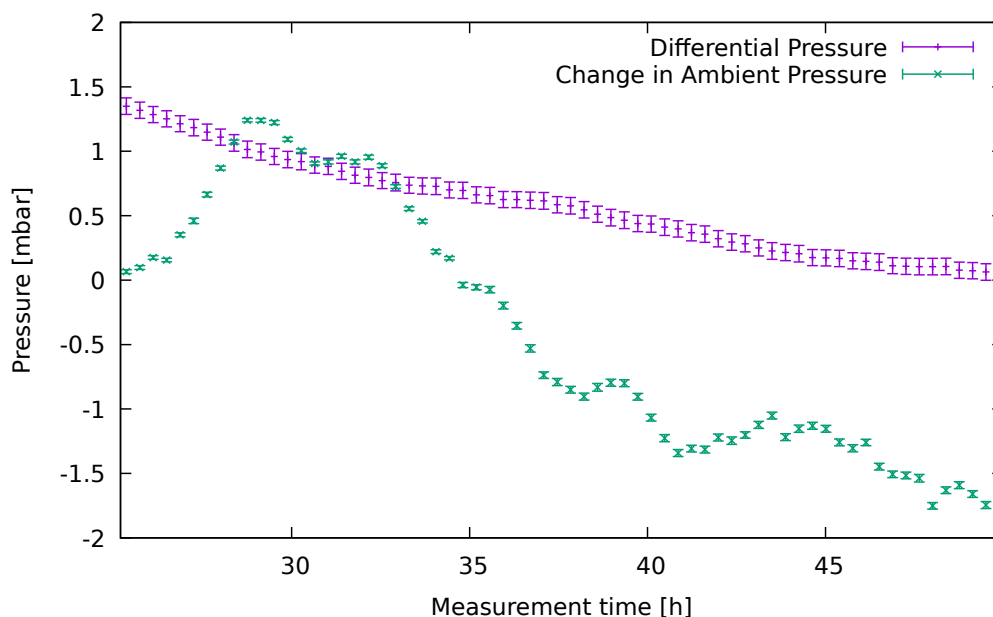
Figure 4.15: A typical decay of overpressure observed in the test-measurement, represented by the purple points. Also shown is the change in ambient pressure in green. The points shown are weighted averages over 60 measurement points. The uncertainties are calculated as described in section 4.3 combined with the variation of the weighted averages. Since the temperature is constant during the measurement, the uncertainties of the change in ambient pressure are small. Only every 30th point is shown.

Figure 4.15 shows a typical decay of overpressure with the bubbler included in the offset measurement setup. Noticeably, the decay of overpressure takes several hours. Both, the lack of changes in differential pressure with changes in ambient pressure and

the prolongation of the measurement, point towards the effect of the bubbler on the measurement outcome. For the small volume of the hoses of $(80\pm1)\,\mathrm{mL}$, the change in setup volume due to differences in oil levels in the bubbler pipe is not negligible. The effect of decreasing numbers of gas particles in the setup on the differential pressure is dampened due to a correlated decrease in volume.

The bubbler should not contribute to the total leakage of the setup. The oil-barrier provided by the bubbler is gas tight for gas pressures below the pressure relief threshold. Omitting the bubbler therefor does not impact the result of the measurement.

The offset leakage measurement setup is shown in fig. 4.16. With only the excess gas relief bubbler present, the maximum overpressure can be raised to $2\,\mathrm{mbar}$.
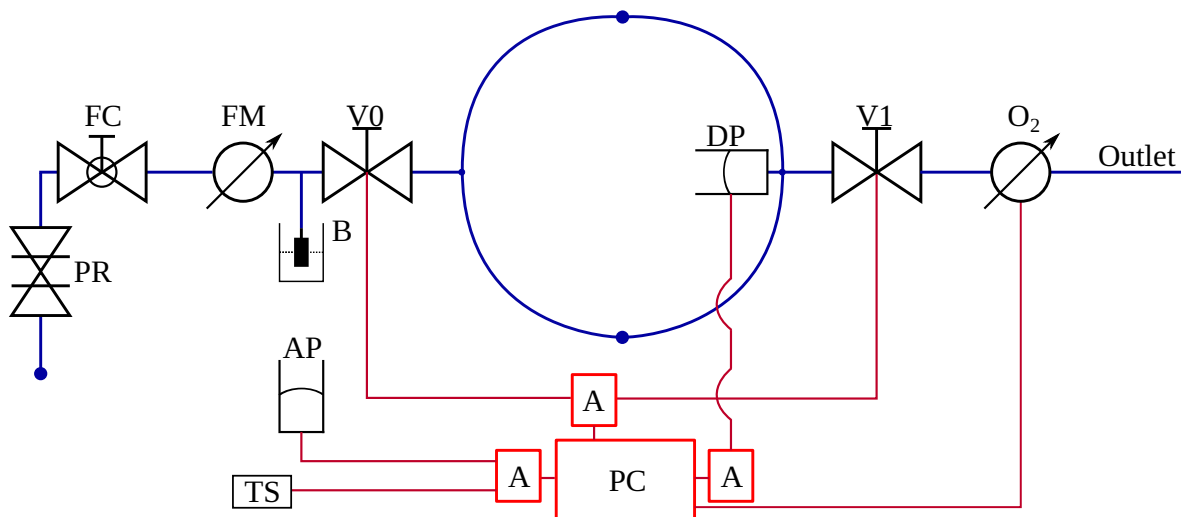
Figure 4.16: A sketch of the measurement setup. Gas connections are shown in blue, electrical connections in red. The abriviations are identical to the ones used in fig. 4.6. The bubbler previously included in the gas system between valve 0 and valve 1 is replaced by a plug.

As can be observed in fig. 4.17, the internal overpressure is directly linked to changes in ambient pressure. An increase in ambient pressure directly results in a decrease in overpressure, while a decrease in ambient pressure translates to an increase in overpressure. To correct for changes in ambient pressure, it is therefor viable to add the change in ambient pressure to the differential pressure for the offset measurements. For the measurement cycle previously shown in fig. 4.17, the resulting corrected overpressure decay is shown in fig. 4.18.
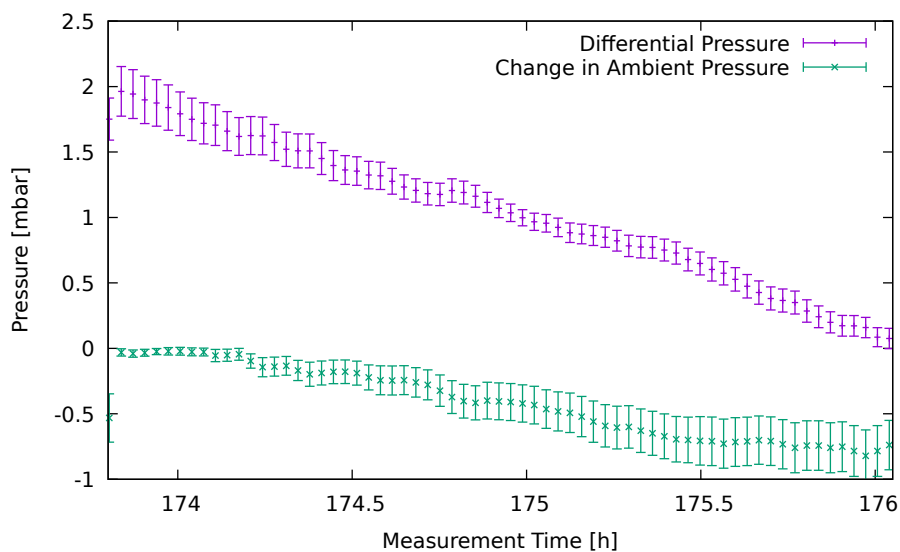
Figure 4.17: The decay of overpressure over measurement time in purple and the change in ambient pressure in green. Uncertainties calculated as described in eq. (4.3) and eq. (4.2) combined with the variation of the weighted mean. The increasing uncertainty of change in ambient pressure is due to a change in temperature.
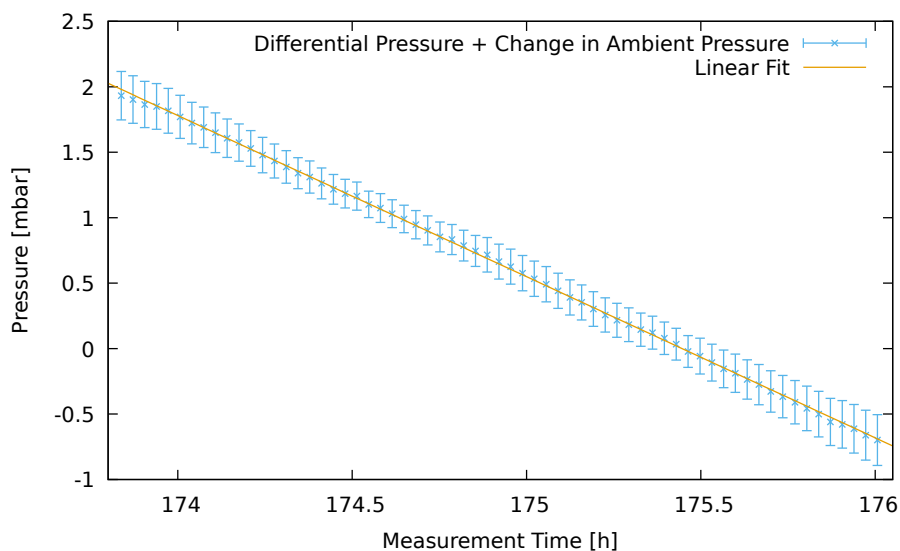
Figure 4.18: A typical decay in overpressure corrected by the change in ambient pressure. The values shown are averaged over 60 measurement points. The error bars represent the combined uncertainties of the differential pressure readings, the change ambient pressure values and the variance of the weighted mean. The displayed fit is a linear function with an incline of $(-1.2238 \pm 0.0006) \frac{\text{mbar}}{\text{h}}$.

Figure 4.18 shows a linear decay of the overpressure in the gas system. Negative pressures are the result of decaying ambient pressure, visible in fig. 4.17. A linear deterioration is not expected for a pressure driven decay. As discussed in section 3.10

and section 3.11, an exponential decay is anticipated. A linear decay points towards a very small leakage, where a laminar flow is no longer present, unlike the holes discussed in section 3.10.

Regardless of physical justification, a linear function describes the data very well. For the analyses of the leakage offset measurements linear fits are applied to the data. The incline a of the linear fits can be calculated into a volume outflow. With the ideal gas equation, eq. (3.3), the volume outflow V_{out} is determined to be

$$V_{\text{out}} = a \cdot \frac{V_{\text{GS}}}{p_{\text{Amb}}} \tag{4.17}$$

where V_{GS} is the volume of the gas system included in the offset measurement and $p_A mb$ is the ambient pressure. V_{GS} is calculated by measuring the length of the hoses between V0 and V1 in fig. 4.16 and multiplying it by the cross-section area of the hose. The combined length of all the hoses is $(6.33 \pm 0.10)\,\text{m}$. The uncertainty is an estimation that accounts for the unknown effective volumes of involved fittings. The cross-section area is the area of a circle with a radius of $2\,\text{mm}$. The volume determined this way is $V_{\text{GS}} = (80 \pm 1)\,\text{mL}$.

The ambient pressure data are obtained by calculating the weighted average of the measurement values over the entire measurement cycle. The uncertainty attached to these values is a combination of the maximum systematic uncertainty in the measurement cycle, discussed in section 4.3.3, and the variance of the weighted average, as described in section 3.13.

Using eq. (4.17), all determined inclines are converted into a leakage rate for the rest of the analyses of the offset measurements.

Measurements are conducted before and after the investigation of the TRD module. This is done to ensure long term leak tightness of the gas system supplying the module and to improve data availability for investigations into temperature and ambient pressure dependencies. The results of the measurements are presented in the context of said dependencies.

Figure 4.19 shows the determined leakage rates for both measurements. For the second measurement, only cycles of a length of more than $0.5\,\text{h}$ are shown. The observed differences in leakage rate are further discussed in the following subsections. The average leakage rate for the first measurement is $(119 \pm 16)\,\frac{\text{µL}}{\text{h}}$ the one for the second measurement is $(57 \pm 3)\,\frac{\text{µL}}{\text{h}}$. The uncertainty of the first average is dominated by the statistical
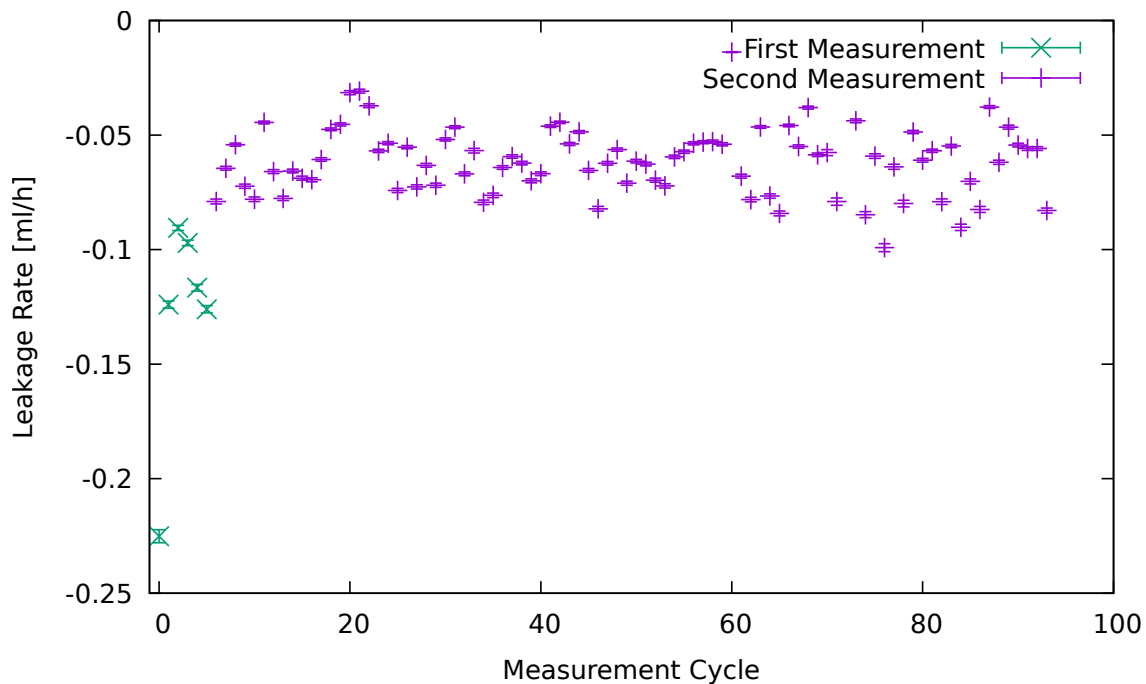
Figure 4.19: The obtained leakage rates for both measurements. For the second measurement, only cycles longer than 0.5 h are shown. The error bars are partly covered by the point markers.

uncertainty, determined as discussed in section 3.13. The second values uncertainty are of equal parts systematic and statistical.

4.4.1 Temperature Dependencies

To evaluate temperature dependencies, the temperature output of the *Orbisphere* is used for the conducted offset measurements. The temperature readings are averaged. The standard deviation of that average combined with the maximal systematic uncertainty yields the total uncertainty. Especially for large changes in temperature during a measurement cycle, this method is suboptimal. For the low cycle-length of the offset measurements, however, this method suffices.
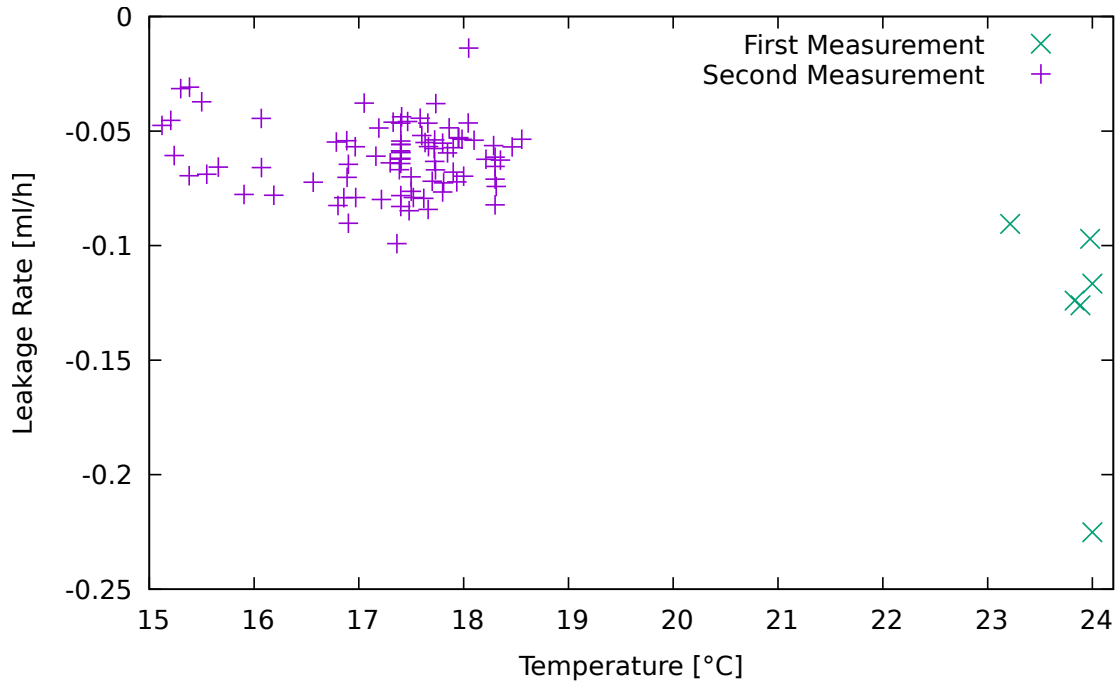
Figure 4.20: The volume outflow determined by linear fits to the ambient pressure corrected overpressure decay measurements and eq. (4.17) as a function of the setup temperature. The measurement values obtained before the chamber measurement are shown in green, the ones after in purple. The temperatures are averages over the measurement cycle. The uncertainties of the values are not shown. The data plotted for the second measurement only show instances, where the measurement cycle is longer than 0.5 h. A heat map of this plot is shown in fig. A.14.

The relation between temperature readings of the *Orbisphere* and the decay rate, determined by applying linear fits to the ambient pressure corrected data, is shown in fig. 4.20. For the second measurement, plotted in purple in fig. 4.20, the uncertainties of the decay rate are high compared to other data points. In these cases, the linear fit does not describe the data well. Examples of these decays are shown in appendix A.5. In some of these measurement cycles, unexpected bumps in the measurement data are observed. In others, the change in ambient parameters is rapid, leading to inaccuracies in the correction method of choice.

The temperature relation displayed in fig. 4.20 suggests a positive correlation between the temperature in the gas system and the observed absolute leakage rates. The higher the temperature, the faster the pressure in the gas system seems to decay. While the data suggests a correlation, the setup might have been set up differently for the second measurement. Some connections had to be opened and resealed in the measurement

process, which might have lead to different leakage quality between the offset measurements.

4.4.2 Pressure Dependency

The ambient pressure readings are obtained by the absolute pressure sensor discussed in section 4.3.3. The weighted average of the ambient pressure is calculated for each measurement cycle. This is an approximation, the accuracy of which depends on the change of the ambient pressure within the specific cycle.
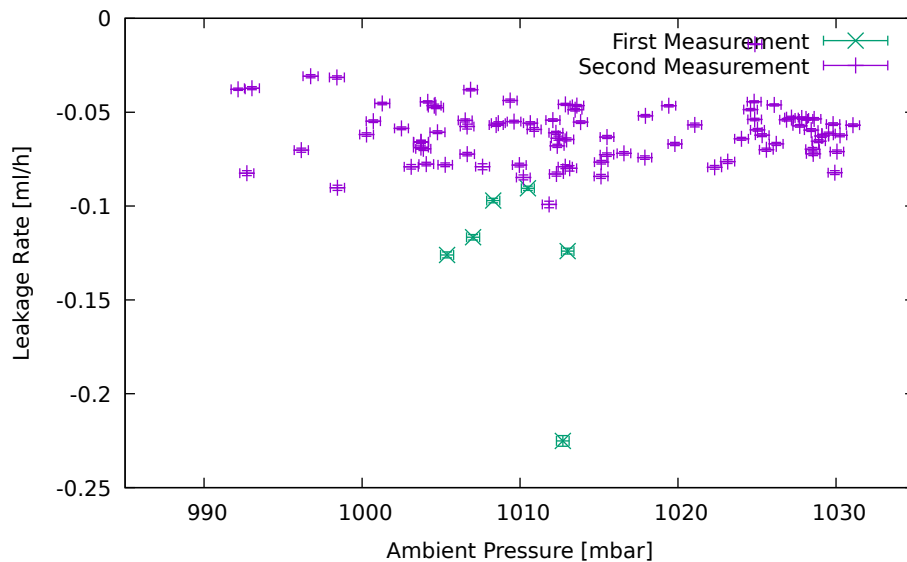
Figure 4.21: The volume outflow determined by linear fits to the ambient pressure corrected overpressure decay measurements and eq. (4.17) as a function of the ambient pressure. The measurement values obtained before the chamber measurement are shown in green, the ones after in purple. The ambient pressure values are weighted averages over the measurement cycle. The uncertainties are a combination of the maximum systematic uncertainty in the respective cycle and the variance of the average. The data plotted for the second measurement only show instances, where the measurement cycle is longer than 0.5 h.

Figure 4.21 shows the determined volume outflow and the corresponding ambient pressure. No correlation between ambient pressure and decay rate can be determined. This behavior is expected. No correlation with the ambient pressure beyond the relation in eq. (4.17) is anticipated.

4.4.3 Discussion of the Offset Measurements

Regardless of the dependencies, an upper limit of the offset decay rate is determined to be $(225\pm3)\,\frac{\mu L}{h}$. That is the highest determined volume outflow. This value is an outlier in comparison to all other determined outflow rates. No explanation for this outlier is documented. Since the weighted average of the outflow rates in the first measurement is $(119\pm16)\,\frac{\mu L}{h}$, this outlier is not expected to be representative for the actual leakage rate.

This is further supported by the lower leakage rate determined in the second offset measurement, where the average volume outflow is $(57\pm3)\,\frac{\mu L}{h}$.

The pneumatic plug connectors used for the prototypes investigated in this thesis, which are also used in these offset measurements, are likely to be the weak link in the gas system. All other connections are realized using stainless steel *Swagelok* gas fittings.

The investigations of correlations between ambient quantities and the determined decay rate yield no reliable conclusions. A positive correlation between temperature and absolute leakage rate seems likely, but is not proven by the data accumulated in these sections.

Measurements with the final gas detector will increase reliability and repeatability of offset measurements. The screwed on gas connectors of the final design are easier to handle repeatably.

Regardless, the determined upper limit for the offset leakage of $225\,\frac{\mu L}{h}$ would still allow the measurement of leakage rates in the expected order of magnitude of $426\,\frac{\mu L}{h}$.

4.5 Leakage Measurements on a TRD Prototype

With the low leakage rate of the setup without the chamber found in section 4.4, a measurement including a TRD module can be conducted. This measurement utilizes the complete setup described in section 4.3.

A total of 55 measurement cycles are conducted for this measurement with the TRD-prototype.
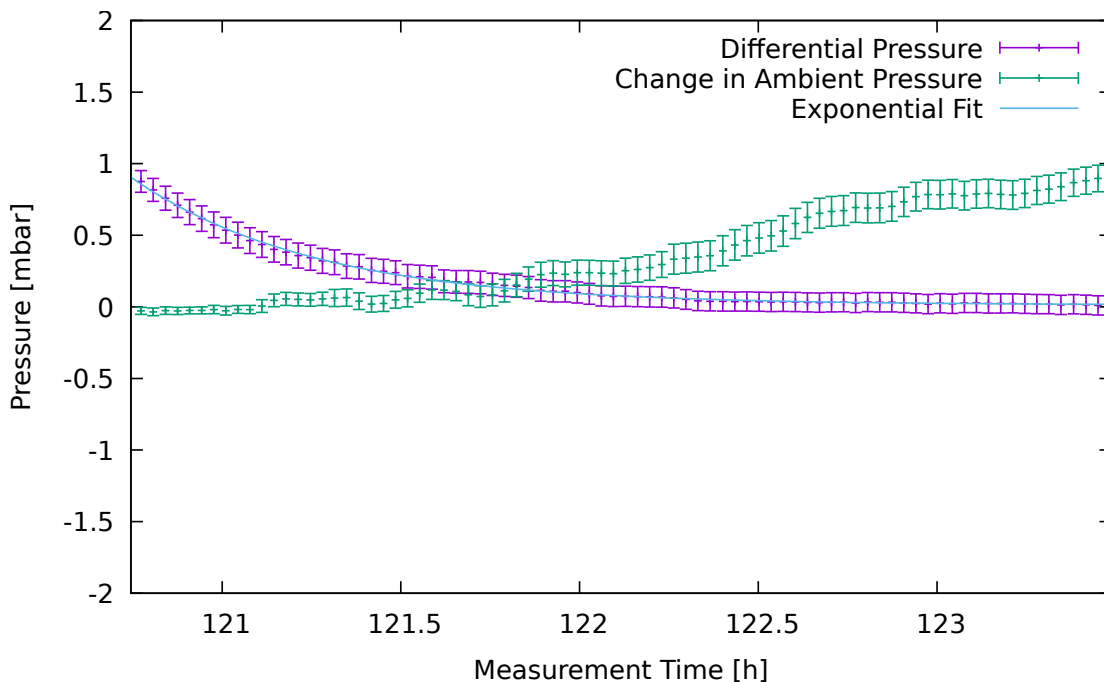
Figure 4.22: The first measurement cycle conducted with the TRD module in place. An exponential fit based on eq. (3.10) is applied to the data and shown in blue. The data are not corrected for changes in ambient pressure. The points shown are averaged over sixty consecutive measurement values.

Figure 4.22 shows the first measurement cycle conducted with the TRD module in place. The fit applied to the data is based on eq. (3.9). Instead of the absolute pressure described in eq. (3.9), the fit describes the differential pressure $\Delta p(t) = p(t) - p_{\mathrm{Amb}}$. A fit parameter p_{Offset} is added, accounting for systematic uncertainties in the differential pressure readings. The fit parameters are Δp_0, λ and p_{Offset}:

$$\Delta p(t) = \Delta p_0 e^{-\lambda t} + p_{\mathrm{Offset}}. \tag{4.18}$$

The initial overpressure Δp_0 is expected to always be slightly below $1\,\mathrm{mbar}$, since the setup is set to start a measurement cycle with this overpressure. The decay rate λ can be translated into a volume leakage rate by means of eq. (3.11). The offset pressure p_{Offset} accounts for systematic uncertainties and is expected to be close to zero.
The ambient pressure in eq. (3.11) is given by the weighted average of all pressure readings within each measurement cycle. The uncertainty attached to the obtained value is the maximum systematic uncertainty for a pressure reading within the measurement cycle combined with the variance of the weighted mean, as discussed in section 3.13.

The temperature associated with a measurement cycle is calculated equivalently from the temperature readings of the *Orbisphere*.
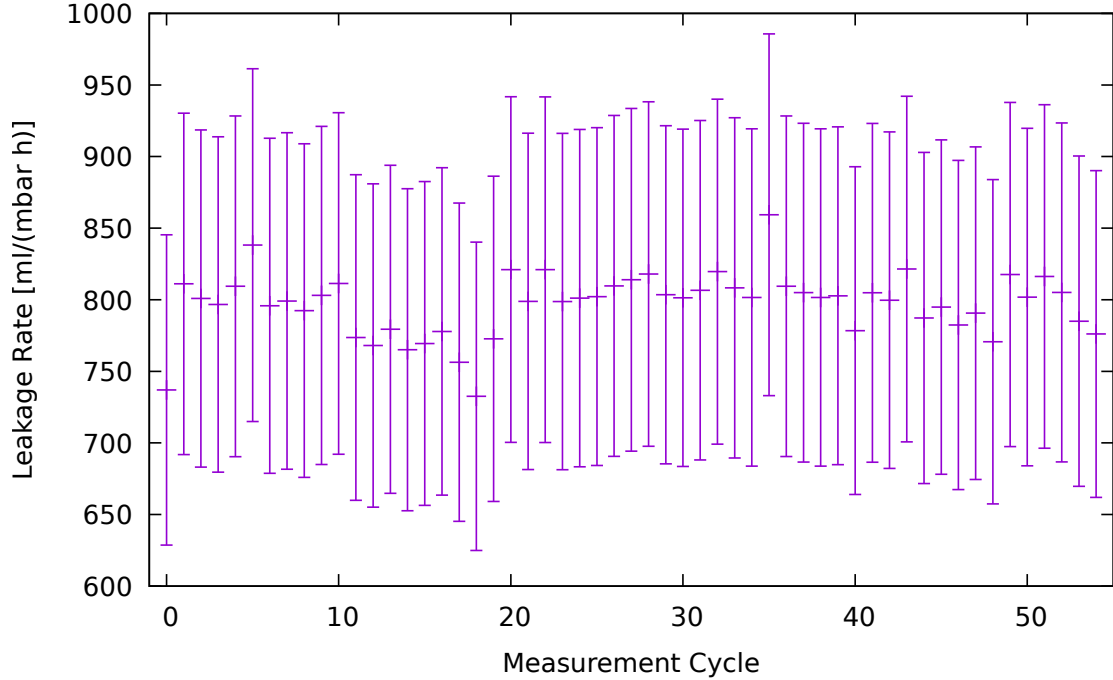
(a) The calculated leakage rates for each measurement cycle based on eq. (3.11). The uncertainties are calculated from the uncertainties of λ, B and p_{Amb}. The uncertainties are almost entirely due to the large uncertainty attached to the volume expansion coefficient B. This figure changed due to the error discussed in chapter 1.
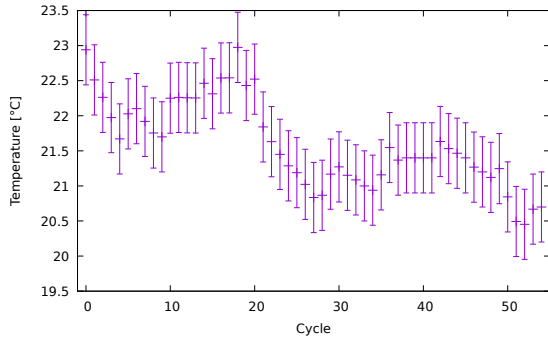
(b) The evolution of the ambient temperature over the measurement cycles. The uncertainties are determined as described in the text.
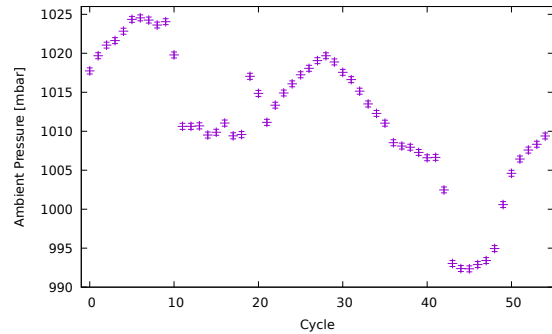
(c) The evolution of the ambient pressure over the measurement cycles. The uncertainties are determined as described in the text.

Figure 4.23: The calculated volume flows F_V based on eq. (3.11) and the average ambient temperature and pressure for each measurement cycle.

The leakage rates and the evolution of contributing quantities are shown in fig. 4.23. The other fit parameters are discussed and the raw decay rate λ is shown in appendix A.6.

As can be seen in fig. 4.23a, the leakage rate is approximately constant over the measurement cycles. Especially for cycles ten to twenty and fifty to fifty-five this constant nature is not preserved. Many factors may contribute to this observation. An underestimation of the ambient pressure might be an issue in these cycles. However, this is not expected, as the ambient pressure sensor is specified for a sufficiently high resolution, detailed in section 4.3.3. The shape and size of leakages in the module might change with temperature. As shown in fig. 4.23b, the temperature is unusually high for cycles ten to twenty. For cycles fifty to fifty-five the temperature is comparatively low.
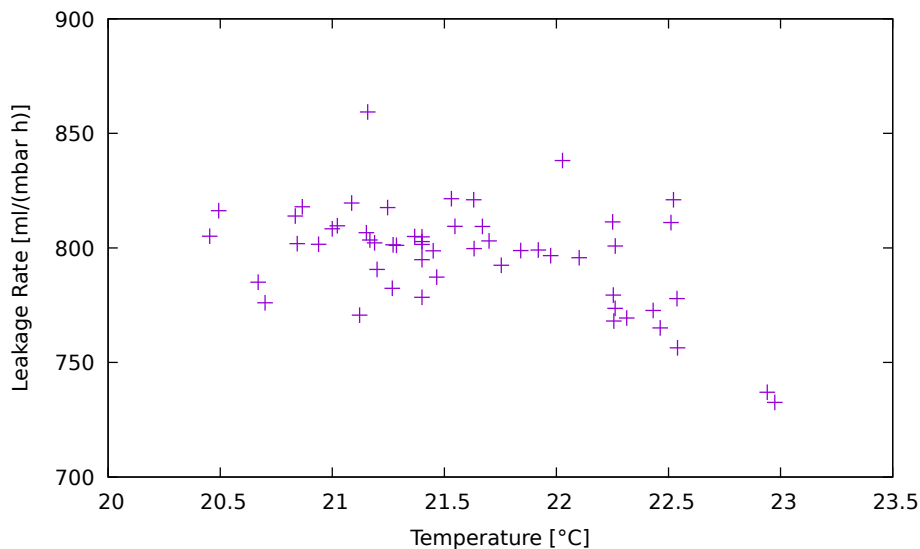
Figure 4.24: The determined leakage rate by temperature. The error bars of the leakage rate are not shown, to preserve visibility of the correlation. A heat map of this plot is shown in fig. A.19. This figure changed due to the error discussed in chapter 1.

The relation between temperature and leakage rate is shown in fig. 4.24. An accumulation of points is observable on the diagonal of fig. 4.24. This points towards a negative correlation between temperature and leakage rate, also found in section 4.6.1. The number of points off the diagonal in fig. 4.24 indicate the existence of another dependency.
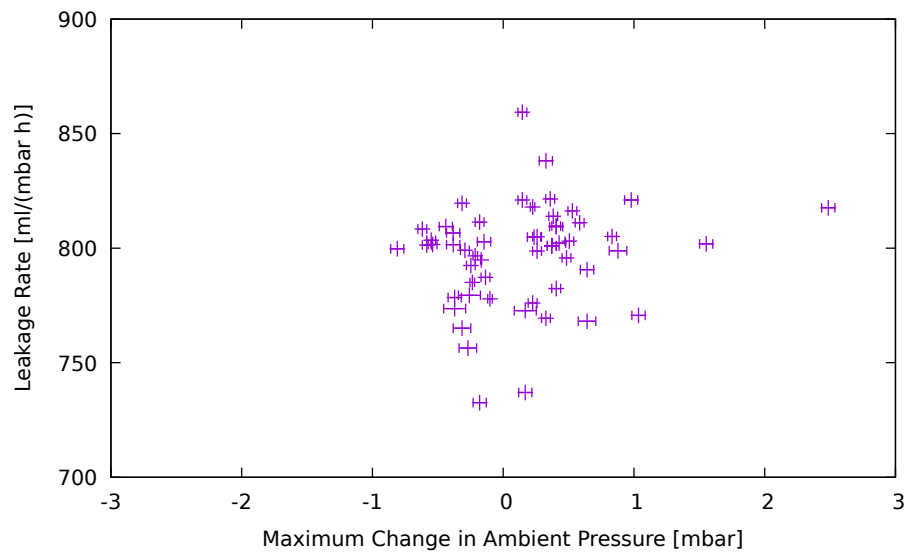
Figure 4.25: The determined leakage rate by maximum change in ambient pressure in the first hour of a measurement cycle. The error bars of the leakage rate are not shown, to preserve visibility of the correlation. This figure changed due to the error discussed in chapter 1.

Figure 4.25 shows the determined leakage rate plotted against the maximum change in ambient pressure within the first hour of each measurement cycle. Within the first hour of the measurement cycle most of the overpressure already decays, as can be discerned in fig. 4.22. No correlation is visible. This is consistent with observations of individual measurement cycles shown e.g. in fig. 4.22.

The change in ambient pressure seems not to be responsible for the off diagonal points in fig. 4.24. Because the determined leakage rate is still in the same order of magnitude of the other leakage rates, the observation is not investigated further.

To get a good representation of the leakage rate occurring, a histogram of the calculated volume flows is shown in fig. 4.26.
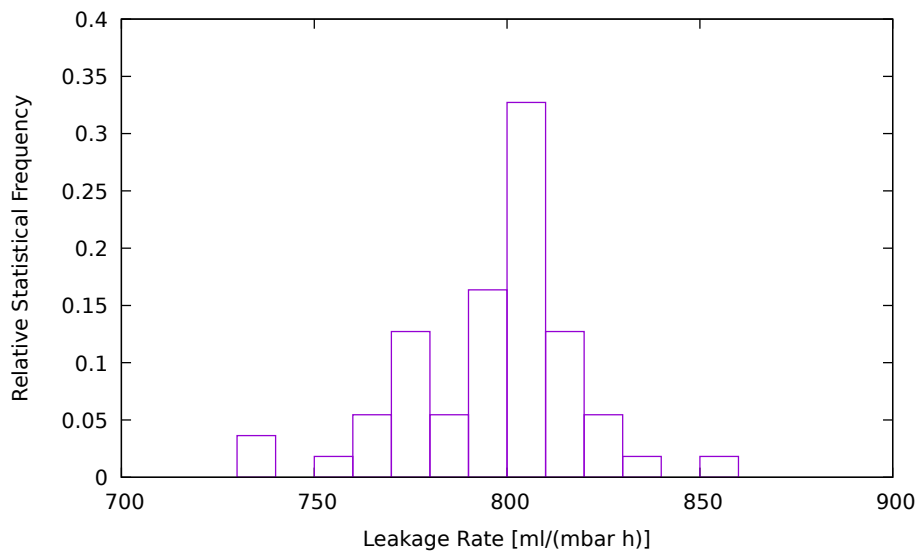
Figure 4.26: A histogram showing the relative frequency of the calculated volume flows with a bin width of $10 \frac{\text{mL}}{\text{mbarh}}$. This figure changed due to the error discussed in chapter 1.

Figure 4.26 shows an asymmetric distribution of calculated volume flows. Noticeably, two peaks can be discerned visually in accordance with the previously discussed temperature dependencies. Averaging the obtained leakage rates yields an average of $(796 \pm 126) \frac{\text{mL}}{\text{mbar·h}}$. This value is far above the expected leakage rate discussed in section 4.2.

The assumptions made to reach this conclusion are taken into account sufficiently by the uncertainty of this value. The latter is dominated by the uncertainty of the volume expansion parameter B.

The offset leakage determined in section 4.4 is negligible compared to this leakage rate. The localization of the leakages contributing to this leakage rate is discussed in the following section, section 4.6.

4.6 Locating Leakages in the TRD Prototype

To find the origins of leakage of the prototype found in section 4.5, further measurements towards its gas tightness are conducted. The possible leak sites are narrowed down by removing and reattaching plastic tape to the prototype under repetition of leakage measurements. Only seven measurement cycles are conducted for each configuration, to avoid unnecessary mechanical stress on the module.

Utilizing a gas sniffer and Helium, several precise leak sites are found.

4.6.1 Leakages underneath the Kapton Tape

As discussed in section 3.8.1, the investigated module already had undergone some attempts to seal leakages before the measurement described in section 4.5. Removing the *Kapton* tape applied as part of these affords and repeating the measurement yields information concerning the location of leakages underneath the tape.

Applying the same analysis steps for this measurement as in section 4.5, yields fig. 4.27.
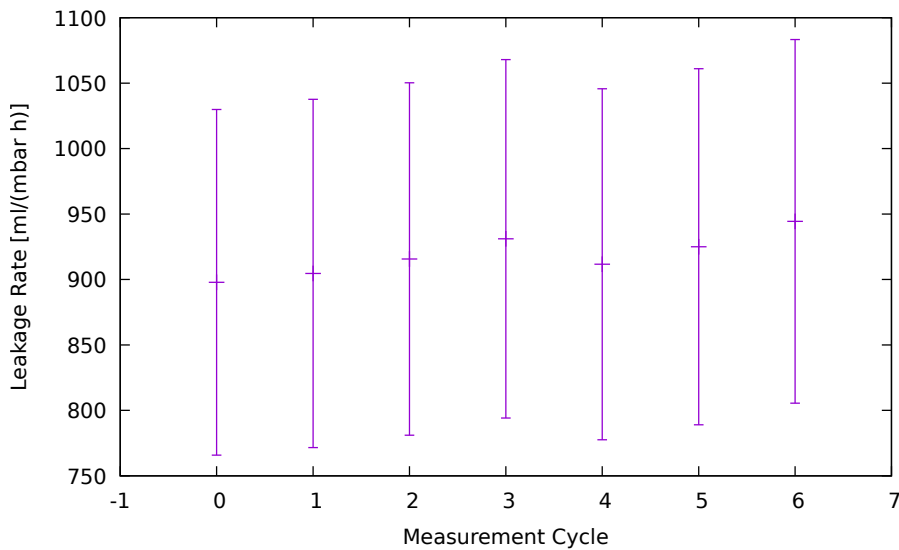
Figure 4.27: The calculated volume flows for each measurement cycle based on eq. (3.11). The uncertainties are calculated from the uncertainties of the average ambient pressure p_{Amb}, the decay parameter λ and the uncertainty of B. This figure changed due to the error discussed in chapter 1.

Comparing fig. 4.23a to fig. 4.27 shows that the leakage rate without the tape attached is higher. While the previous average was $(796 \pm 126)\,\frac{\mathrm{mL}}{\mathrm{mbar \cdot h}}$, the new average is $(918 \pm 139)\,\frac{\mathrm{mL}}{\mathrm{mbar \cdot h}}$.

Besides the increase in leakage rate due to removal of the tape, the temperature dependency hypothesized in section 4.5 is further substantiated by the data shown in fig. 4.28.
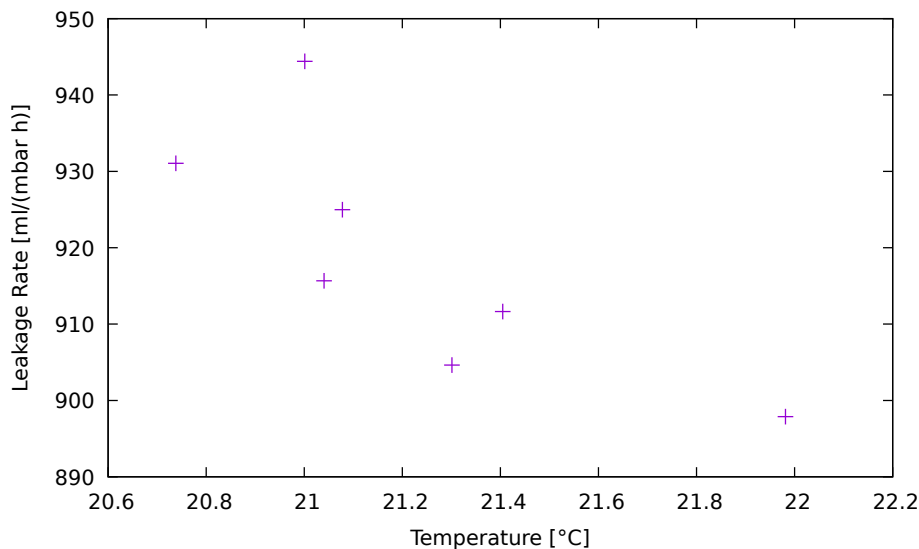
Figure 4.28: The average temperature readings of the *Orbisphere* and the occurring leakage rate for all seven measurement cycles. The uncertainties of the values are not shown to preserve visibility. This figure changed due to the error discussed in chapter 1.

The data shown in fig. 4.28 show the decreasing of leakage rate with increase in temperature. Since the temperature range is the same as in section 4.5, the temperature dependencies do not have to be taken into account for the discussion of the increased leakage rate.

The increased leakage rate after removal of the *Kapton* tape indicates the existence of leakages previously covered by it. This points towards leakages in the material transition from Aluminum frame to distance ledge or wire clamp system. Further, the seam between entrance window and the rest of the module might not be leak tight.

To check this assumption, residue free tape is applied to the module, covering both transitions.

The leakage measurement is repeated. The same analyses steps as for the previous measurements are taken.
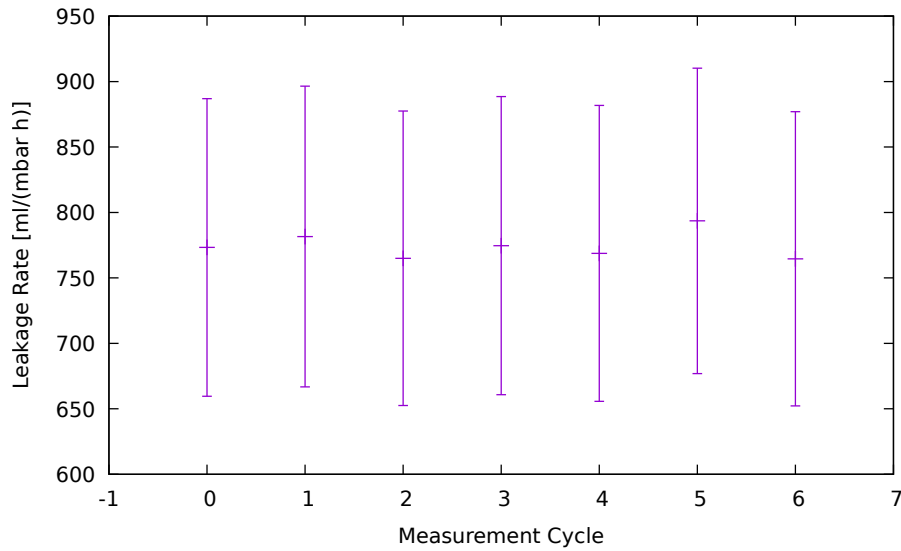
Figure 4.29: The calculated volume flows for each measurement cycle based on eq. (3.11). The uncertainties are calculated from the uncertainties of the average ambient pressure p_{Amb}, the decay parameter λ and the uncertainty of the volume expansion parameter B. This figure changed due to the error discussed in chapter 1.

Averaging over the volume flows shown in fig. 4.29 yields an average leakage rate of $(774 \pm 117)\,\frac{\mathrm{mL}}{\mathrm{mbar \cdot h}}$. This leakage flow does not significantly divert from the original volume flow of $(796 \pm 126)\,\frac{\mathrm{mL}}{\mathrm{mbar \cdot h}}$. The temperature is very similar to the temperatures for the measurement discussed in section 4.5, varying between $20\,^\circ\mathrm{C}$ and $21\,^\circ\mathrm{C}$. Therefore, the temperature dependency should be negligible for this comparison.

The significant change in leakage rate with reapplication of the tape leads to the conclusion that a significant amount of the leakage of the module stems from leakages located in the material transitions between Aluminum frame and distance ledge systems and distance ledge systems and entrance window.

More precise localization measurements are conducted in the following section, section 4.6.2.

4.6.2 Locating Leakages with a Gas Sniffer

To further narrow down the location of leaks, measurements with the gas sniffer, described in section 4.6.3, are conducted. The chamber is flushed with *Sagox 18* at about $2\,\frac{\mathrm{L}}{\mathrm{h}}$. Helium is added at roughly $0.3\,\frac{\mathrm{L}}{\mathrm{h}}$. A flow chart of the measurement setup used is shown in fig. 4.30. The measurement is repeated for higher gas flows leading to higher differential pressures. The investigated differential pressures range from $\approx 0.1\,\mathrm{mbar}$ to
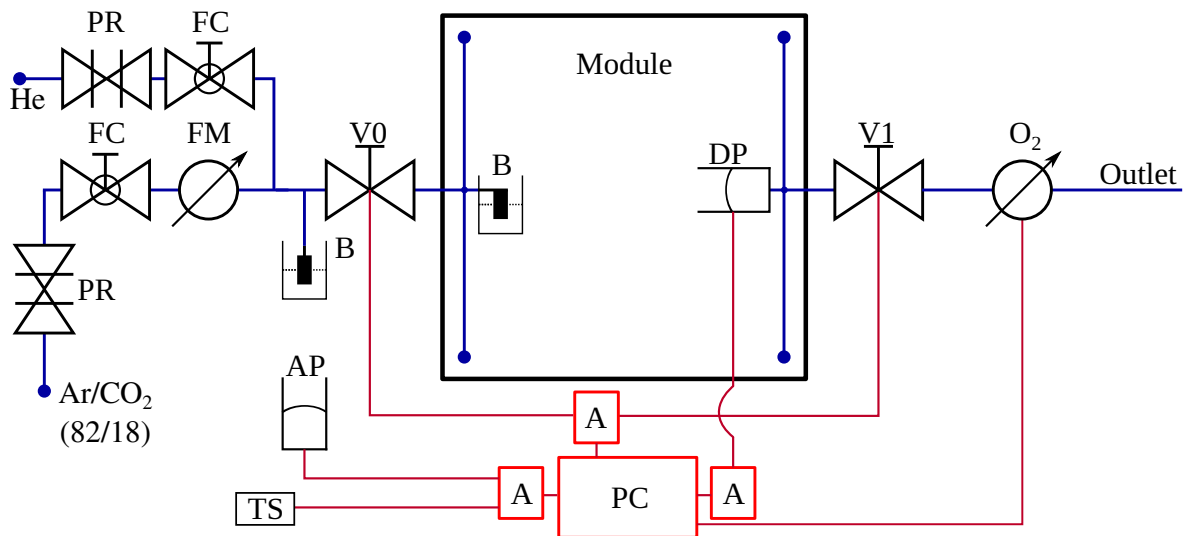
Figure 4.30: The setup used for the measurement with the gas sniffer. Another pressure reducer and another flow controller are added to the setup described in section 4.3 to introduce Helium from a gas bottle into the setup. The blue lines show gas connections, the red lines show electrical connections. The abbreviations are the same as in fig. 4.6

$\approx 0.9\,\mathrm{mbar}$. At higher pressures, the amount of gas leaving the gas system increases, as discussed in section 4.5. Smaller leakages might therefore be detected.

4.6.3 Gas Detector

To locate leaks in the gas system, a hand held gas detector is used. The model available is *Ion Science Messtechnik*'s *GAS-CHECK 5000.*

This device has a probe protected by a plastic nozzle through which it analyzes the gas in front of it. To find leaks, the device is put in close proximity to suspected leak sites with the nozzle pointing at the location in question. If the device detects gas, it is set to beep, flash an LED and display a leakage rate on its LCD [99, p.25, sec.4.6.1]. For small leaks, the procedure to find leaks alongside material transitions is to move the nozzle with $10\,\frac{\mathrm{mm}}{\mathrm{s}}$ along the seams [99, p.26, sec.4.6.2]. Evaluating the beep-frequency and the displayed leakage rate allows narrowing down of the location of the leak [99, p.25 sec.4.6.1].

For the short probe without the protective nozzle the device can detect gas flows below $1 \cdot 10^{-4}\,\frac{\mathrm{mL}}{\mathrm{s}}$ [99, p.23, sec.4.4.1]. The sensitivity depends on the gas to be detected and whether the protective nozzle is used. The device dilutes the gas tenfold for the analyzer if the nozzle is installed [99, p.7, sec.2.2].

To increase the sensitivity, a longer probe can be installed. This increases the reaction time of the device from about $1\,s$ to about $9\,s$[99, p.25, sec.4.6.1].

Principle of Operation

The device sucks small amounts of gas from the inlet into an analyzer, which measures the heat conductivity of the gas. On first start-up of the device or by manual command, the conductivity offset is determined. Every gas with a thermal conductivity different from this offset is registered by the device. The difference between measured and offset conductivity is calculated into a leakage rate [99, p.4, sec.1.3].

Uncertainties

The calibration of this device is overdue. Additionally, the gas mixture used in the setups discussed in this thesis is not natively supported by the device. The quantitative leakage rate displayed by the device is therefore meaningless.

However, a qualitative ambience or absence of leaks can be determined utilizing this detector. A quantitative argument is to be made by the radius around a leakage in which the device sounds the alarm. Additionally, if a leakage is large, the device takes time to get rid of the large amount of gas of different heat conductivity within its analyzer. During that time, it continues to signal. Therefore, by the duration of the alarm, an estimation of the relative size of the leakage can be made.

4.6.4 Localization Measurements

The sides of the module are investigated as described in section 4.6.3, slowly proceeding along the seam between backpanel and distance-ledge system. No tape is applied to the prototype in this measurement. Several leakages are found and their locations are sketched in fig. 4.31.

All the leaks found in the modules are either located at the corner of the module or on the distance ledge sides of the chamber, parallel to the wires. By the duration of the alarm a qualitative, relative estimation of the leak size can be attempted, as motivated in section 4.6.3.

For leak four and six in fig. 4.31 this duration is noticeably higher than for the rest of the leaks. Leak four, shown on the left-hand side of fig. 4.32, is the biggest leak in the entire chamber.
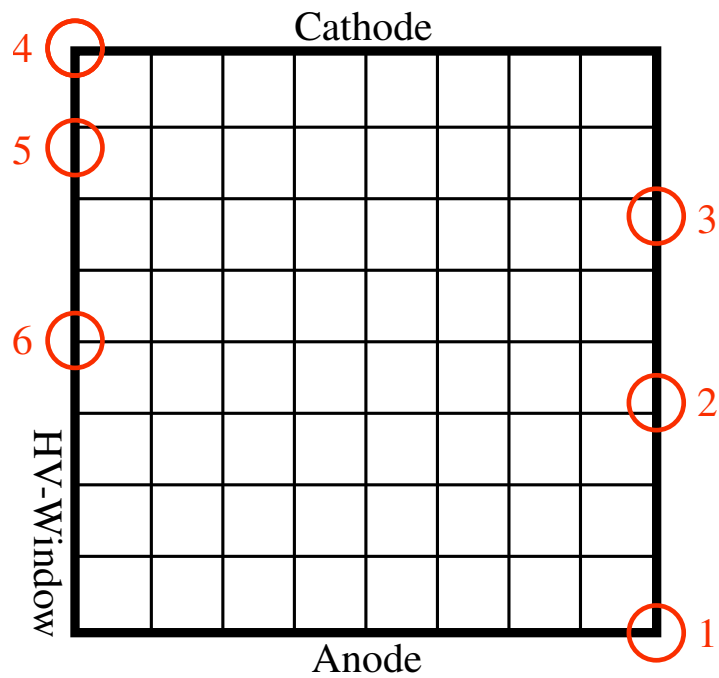
Figure 4.31: A sketch of the locations of the leaks found in the module. The leaks are numbered to ease discussion. The sides of the module are named after the high voltage connectors passed through on that side.
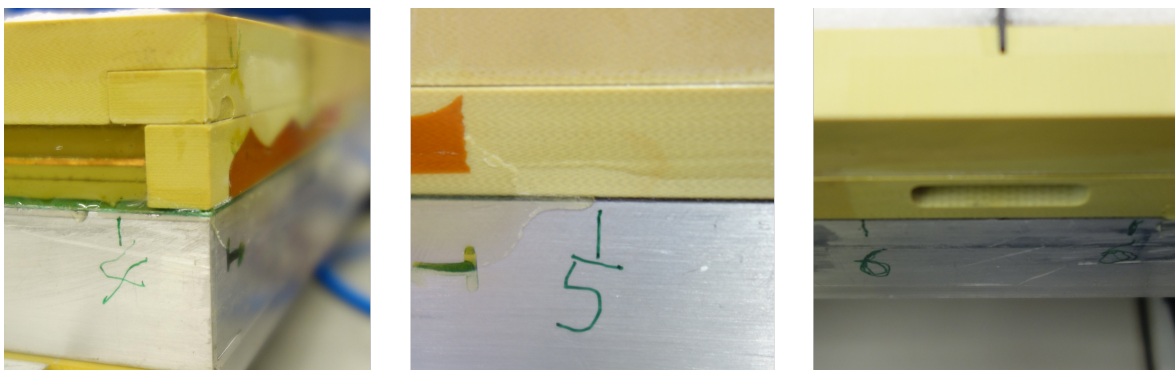
Figure 4.32: Photographs of selected leak sites. The leaks shown are numbered 4, 5 and 6 in fig. 4.31.

No leaks are found in the backpanel of the module. The same is true for the entrance window.

Since two out of four corners of the chamber are not leak tight, the production process is revised. The remaining leaks are all located in the distance ledge systems parallel to the wires. The amount of glue applied in the building process was insufficient. This is especially true for leak 6, shown on the right-hand side of fig. 4.32, located at the high voltage contact for the entrance window.

Noticeably, the distance ledge systems orthogonal to the wires, which are covered by a closed layer of epoxy, are leak-tight, within the sensitivity of the gas detector for operating overpressures ($< 1\,\mathrm{mbar}$). This points to a possible fix, if leaks should remain on the distance ledge sides parallel to the wires of the MWPC in future productions. The distance ledges in question could be reduced in depth, to allow a filling with epoxy similar to the one applied to the sides orthogonal to the wires.

In agreement with the experiment conducted with the test chamber in section 4.7, this measurement also indicates issues with fixes applied after the construction of a leaking module. Leak 5, shown in the middle of fig. 4.32, is located right next to epoxy glue added after module production. The gas leaving at the location of leak 5 might originate at a different internal leak site, which was covered in epoxy glue in an attempted to seal it. The gas seeps underneath this epoxy layer to leak 5. This hypothesis is supported by circumstantial evidence only. In the context of section 4.7, however, this observation is still noteworthy.

4.7 Repairability of a TRD Test-Module

In [Fab21] various behaviors of a TRD test-module under gas flow are investigated. One of the tests conducted in [Fab21, p.62, sec.5.3] includes closing the outlets of the test TRD module while gas still flows into the module. The differential pressure is monitored.

The result of this measurement is the establishment of an equilibrium overpressure. This equilibrium overpressure is flow dependent, as shown in [Fab21, p.69, fig.5.21]. Leakages in the test module investigated in [Fab21] are the cause of this behavior, as concluded in [Fab21, p.62, sec.5.3].

4.7.1 Locating the Leakages

To locate the leakages, investigations using the gas sniffer discussed in section 4.6.3 are conducted. The measurement procedure is the same as discussed in section 4.6.2. A small amount of Helium is added to the Argon/Carbon dioxide (82/18) mixture used for other measurements. The chamber is flushed at $\approx 3\,\frac{\text{L}}{\text{h}}$ total gas flow, with $\approx 0.3\,\frac{\text{L}}{\text{h}}$ of this flow being Helium. Epoxy grouts and material transitions in general are scanned with the sniffer.

Eight leakages are found in the transition from Aluminum frame to distance ledge system. These leakages coincide with the retractions of the epoxy ground behind the frame, one of which is shown in fig. 4.33. The corners of the Aluminum frame also show leakages occurring.

Figure 4.33: A hole in the epoxy grout between Aluminum frame (top) and distance ledge system (bottom) is shown.

4.7.2 Sealing of the Module

An attempt is made to fix the leaks found in section 4.7.1. To seal the test module, additional epoxy glue is added to the grout shown in part in fig. 4.33. The glue is heated using a heat gun, to lower its viscosity and increase flow velocity. The latter should increase depth of penetration and therefore increase the sealing capabilities of the glue. The corners of the aluminum frame are also covered with the same epoxy glue. Figure 4.34 shows the glue added to the module.

4.7.3 Repeating the Leakage Measurement

After the glue is applied to the module, the measurement conducted in [Fab21, p.62, sec.5.3] is repeated, using the same setup documented in [Fab21, p.13, sec.3]. This setup consists of a gas system containing four differential pressure located at the in-
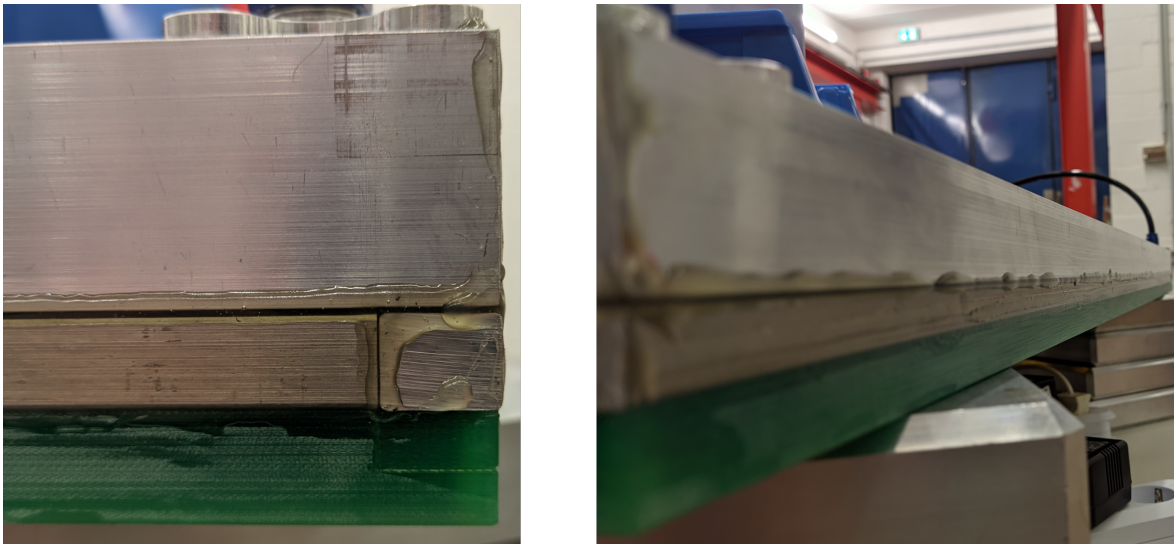
Figure 4.34: The glue applied to the test chamber at the corner of the module, shown on the left, and the transition from Aluminum frame to distance ledge, shown on the right.

and outlet of the TRD test module. The sensors are read out by converting the native 4 mA to 20 mA signal into a voltage by means of a 255 Ω resistor. The voltage is digitized by the 10 bit ADC of an *Arduino Uno* micro controller. A gas flow controller and a flow meter allow for the setting of a specific gas flow. The latter is read out using the same voltage measurement. The setup is discussed in detail in [Fab21, p.13, sec.3]. The gas flow is set to $3\frac{L}{h}$, $5\frac{L}{h}$ and $7\frac{L}{h}$ consecutively. A measurement with no gas flow and therefore no differential pressure is conducted to correct for drift of the measurement offset. For this order of magnitude estimation, an uncertainty calculation is not necessary.

The result of this measurement is shown in fig. 4.35 for a gas flow of $5\frac{L}{h}$. The displayed measurement points are averages over the output of all four differential pressure sensors. As is observed in [Fab21], the measurement values in fig. 4.35 vary. This is an artifact caused by the ADC of the *Arduino Uno* board used in this setup.

Despite the additional glue applied to the module, an equilibrium pressure is still reached. In fig. 4.35, a constant fit is applied to the data, shown as a green line. This fit estimates the equilibrium pressure. The same analysis is done for $3\frac{L}{h}$ and $7\frac{L}{h}$. Figure 4.36 shows the relation between set gas flow and resulting equilibrium overpressure, obtained by the methods described above. Note that the flow values in this graph are lower than the ones discussed in the text. This is due to the fact, that the flows
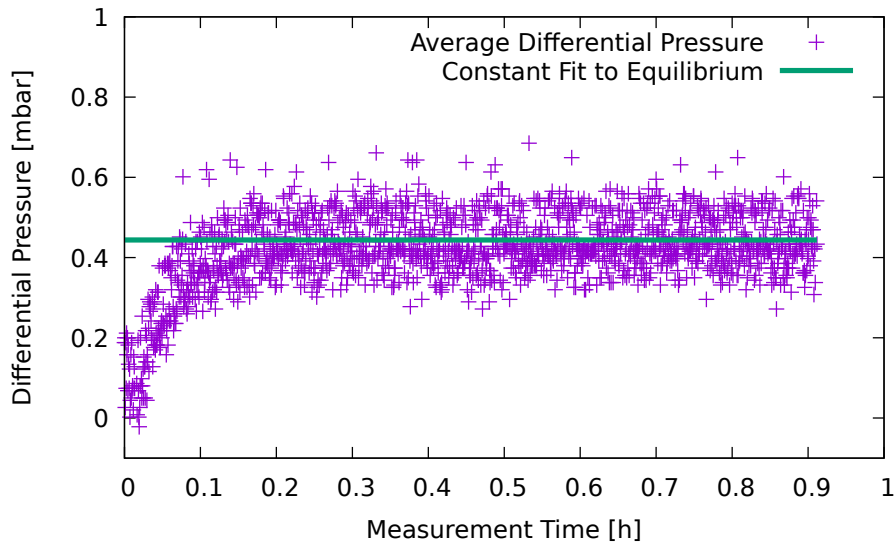
Figure 4.35: The differential pressure over measurement time at a gas flow of $5\,\frac{\text{L}}{\text{h}}$. The displayed pressure is the average output of all four differential pressure sensors included in this setup. The readings are corrected by the measured offset for each sensor before averaging. The constant is fittet to the data points in the time interval between $0.3\,\text{h}$ and $1\,\text{h}$. Only every second measurement point is shown. This plotis shown for the other gas flows in appendix A.8.
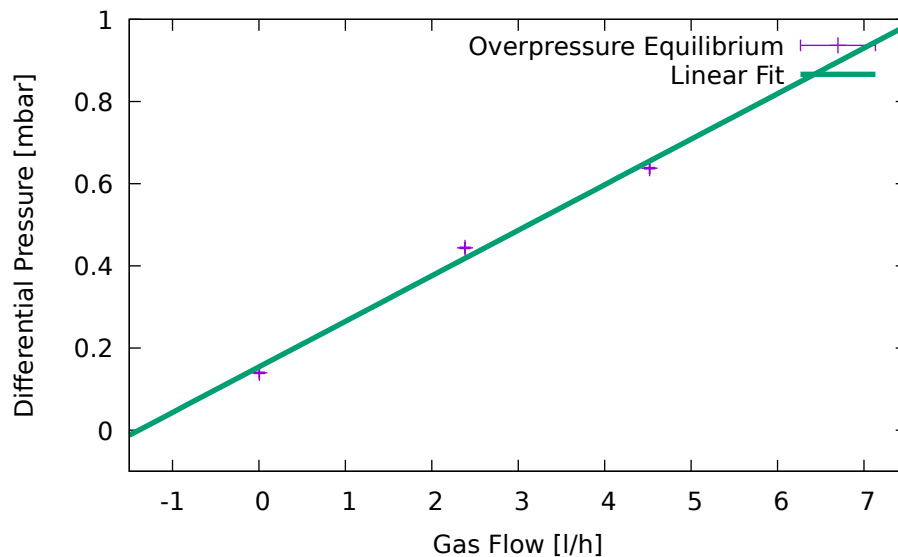
Figure 4.36: The flow dependent equilibrium pressures determined by constant fits to the data obtained in the described measurements. A linear fit is applied to the data. The plot is shown with the individual sensor readings in fig. A.30.
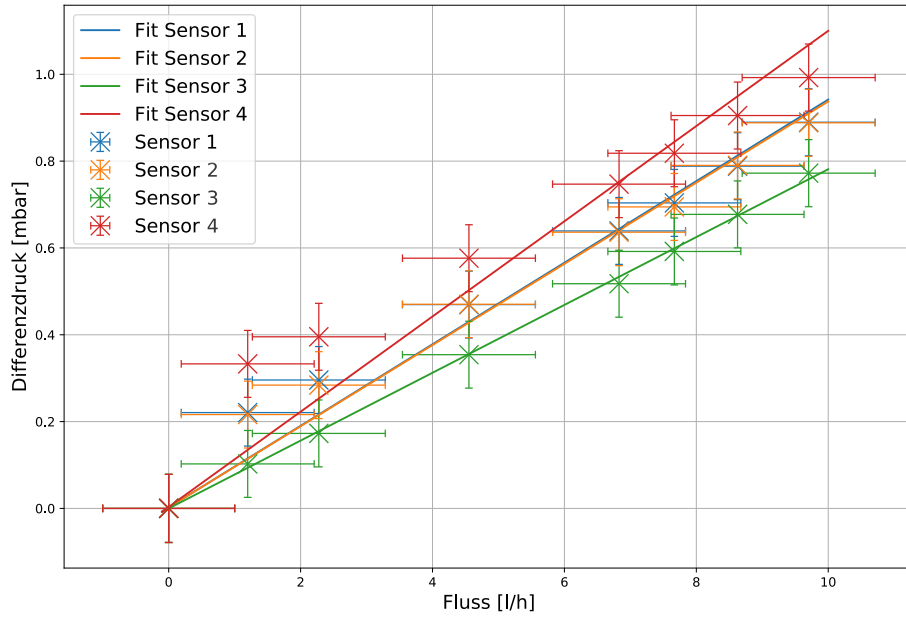
Figure 4.37: Equilibrium overpressures found before the gluing of the module at different gas flows in [Fab21, p.69, fig.5.21, edited to fix key].

Table 4.3: The fit parameters for the linear functions in fig. 4.37 [Fab21, p.68, tab.5.2].

Sensor	Incline $\left[\frac{\text{mbar·h}}{\text{L}}\right]$	Offset [mbar]
1	0.093 ± 0.003	0.002 ± 0.007
2	0.093 ± 0.003	0.002 ± 0.006
3	0.078	$(-5.8 \pm 100.0) \cdot 10^{-5}$
4	0.109 ± 0.006	0.003 ± 0.012

displayed in fig. 4.36 are calculated by [Fab21, p.25, eq.4.6], while the previously mentioned flows are read directly from a digital display on the flowmeter. The flowmeter has an offset of $-2.4\,\frac{\text{L}}{\text{h}}$ to $-2.3\,\frac{\text{L}}{\text{h}}$. All measurement values below zero, corresponding to flows below $2.3\,\frac{\text{L}}{\text{h}}$, are transmitted as $0\,\frac{\text{L}}{\text{h}}$. Therefore the flow calculated using [Fab21, p.25, eq.4.6] is off by about $2.3\,\frac{\text{L}}{\text{h}}$. [Fab21, p.25, eq.4.6] is still used, to better compare the measurement outcomes. The fit parameters of the linear fit in fig. 4.36 are an incline of $(0.11 \pm 0.01)\,\frac{\text{mbar·h}}{\text{L}}$ and an offset of $(0.15 \pm 0.03)\,\text{mbar}$.

The same relation displayed in fig. 4.36 for the measurement after the attempted improvement of module tightness, is shown in fig. 4.37 for the measurement before any changes to the module investigated. For fig. 4.37, the linear fits yield table 4.3 [Fab21, p.68, tab.5.2]. The fit parameters determined for the graphs in fig. 4.37 are in the same order of magnitude as the parameters of the fit in fig. 4.36. The inclines are very close to one another and partly within 1σ uncertainty of each other, despite the under

evaluation and underestimation of the uncertainty of the measurement points. The offsets in table 4.3 differ strongly from the offset determined in fig. 4.36. They seem to be heavily impacted by the measurement point for $0\,\frac{L}{h}$ in fig. 4.37. Extrapolating from the other data points in fig. 4.37 suggests an offset close to the $(0.15 \pm 0.03)\,\mathrm{mbar}$ found for fig. 4.36.

These observations lead to the conclusion, that the attempt of sealing the module was completely unsuccessful. The overpressure equilibriums remain the same.

4.7.4 Repeating the Leak Localization Measurement

The steps undertaken in section 4.7.1 to locate the leakages in the test module are repeated.

The added epoxy glue is leak tight. No more gas is detected at the old leak sites. However, new leaks are detected at the backpanel of the module. The transition between carbon backside of the backpanel and the outer aluminum frame is not leak tight. Gas can be detected in a cable pass through cutout of the backpanel close to the side of the module. The corners of the aluminum frame leak gas, wherever they are not covered by epoxy.

4.7.5 Discussion

The attempt to seal the test-module by adding epoxy glue from the outside showed no significant effect on the leakage rate. The specific leak sites were sealed on the outside of the module, but gas seeps underneath the Aluminum frame to other, previously undetected, leakages.

The design of the test-module differs from the design of the final TRD chambers. The test-module uses Aluminum instead of fiber-glass for the distance ledge systems. Furthermore, the contact of honeycomb, backpanel and ledge system differs. Therefore, the findings of these measurements do not directly impact series production, besides the general point that gas tightness must be ensured from the inside of the module.

While attempts at fixing leaks from the outside succeeded for the ALICE-TRD, the additional time and material required, combined with the negative impact on the mechanical structure, e.g. the added weight and increased size, are to be avoided. Instead, tightness should be reached in the construction process already.

5 Summary and Outlook

The gas tightness of CBM-TRD modules is investigated thoroughly in this thesis.
A setup to measure the leakage rate of an entire CBM-TRD module is designed, commissioned and characterized. The setup monitors the decay of an adjustable overpressure down to a resolution of $0.04\,\mathrm{mbar}$. The conduction of the measurements is automated to reliably repeat the measurement procedure while ensuring module safety.

With these measurements, a leakage rate of $(796 \pm 126)\,\frac{\mathrm{mL}}{\mathrm{mbar}\cdot\mathrm{h}}$ is found for the TRD prototype under investigation. This significantly exceeds the design value for the CBM-TRD. The leakages are located. The findings are provided to the team responsible for chamber construction, which adjusted the procedures accordingly in time for series production.

The leakage value is based on the mathematical description of the pressure decay detailed in section 3.11 and the models used to estimate the additional volume of the setup due to expansion of the TRD module. The uncertainties of these models are the dominant contributors to the uncertainty of the determined leakage rate. For TRD modules produced in, as of writing of this thesis upcoming, series production, this uncertainty is lower.
The setup is not capable of resolving the target leakage rate of CBM-TRD modules, as discussed in section 4.3.6. Measuring only a small fraction of the decay and extrapolating the leakage rate is problematic, because the exponential character of the decay is not necessarily accurate for small leakage rates, as observed in section 4.4. Only an upper limit of the leakage rate can be determined this way, but still does not reach the necessary resolution, as motivated in section 4.3.6. For the modules produced in series production, the lowest resolvable upper limit is approximately $2.4\,\frac{\mathrm{mL}}{\mathrm{h}}$. This can be improved by using a higher resolving ADC for the differential pressure sensor. By using a 10 bit ADC instead of a 9 bit ADC, this limit would get lowered to $1.2\,\frac{\mathrm{mL}}{\mathrm{h}}$, approaching the design value of below $1\,\frac{\mathrm{mL}}{\mathrm{h}}$ (as stated on p.58, tab.5.1. [BBE18]). However, because ambient pressure and temperature might change significantly within

the time frame of 24 h, the measurement would not work for every measurement cycle, negatively impacting predictability of the real measurement time required for each module.

The unfeasible length of measurement time is mainly due to the additional volume of the setup with increasing internal overpressure. It could be discussed, whether a support structure restricting the bulging of the module might therefore increase the resolution of this setup. However, since such a structure would have to make direct contact with the entrance window, risking scratching or other damage, this is not planned. Instead, an Oxygen content measurement at over- and negative pressure, as conducted for the ALICE-TRD, is suggested here. An example of such a measurement is discussed in [Pit12].

While different chemical properties could have an impact on the leakage measured, as observed for water and oxygen in [Web18], the models used to estimate the additional volume of the modules add large uncertainties to the determined leakage rates.

The models might be improved or superseded by more accurate simulations. However, the established method of Oxygen content measurement at over- and negative pressure does not have to rely on such models at all. The better resolution and simpler calculation of the leakage rate from the measured data, discussed in [Pit12, p.77, eq.5.12], makes it the preferable measurement candidate for module series production.

Several investigations towards the origins of the found leakage rate are conducted.

A measurement towards the Xenon tightness of the Aluminum coated *Kapton* entrance window is documented and a sufficient leak tightness of the entrance window is found. Upper limits of leakages for other impurities are assessed. Different observations, described in section 4.1, point towards a leakage in the setup used for these investigations besides the expected leakage of the *Kapton* entrance window. This leakage will lead to an overestimation of the foil leakage, but since the latter is found to be sufficiently low, this is not an issue.

In section 4.6 the distance ledge systems at two sides of the module and the corners, where the distance ledge systems connect to the wire-ledge systems, are found to leak gas. The high voltage connector of the entrance window is also not gas tight.

As no leakages have been found on the wire-ledge sides of the module, where the ledges are fully covered with epoxy, a similar sealing procedure could be considered for the other ledge sides, if necessary.

For the ALICE-TRD, leakages were suspected in the connection between reinforced

honeycomb and pad plane PCB [18, sec.3.4.1]. These findings were taken into account in the production procedure of the CBM-TRD and leakages of this sort were not found so far with the methods used in this thesis project. Nevertheless, the high leakage rate determined in section 4.5 overshadows any more subtle leakages.

While the gas tightness can be improved with the findings of this thesis, the issue might not be completely resolved. As soon as modules are produced, their gas tightness will be investigated.

A Appendix

A.1 Foil Bulging
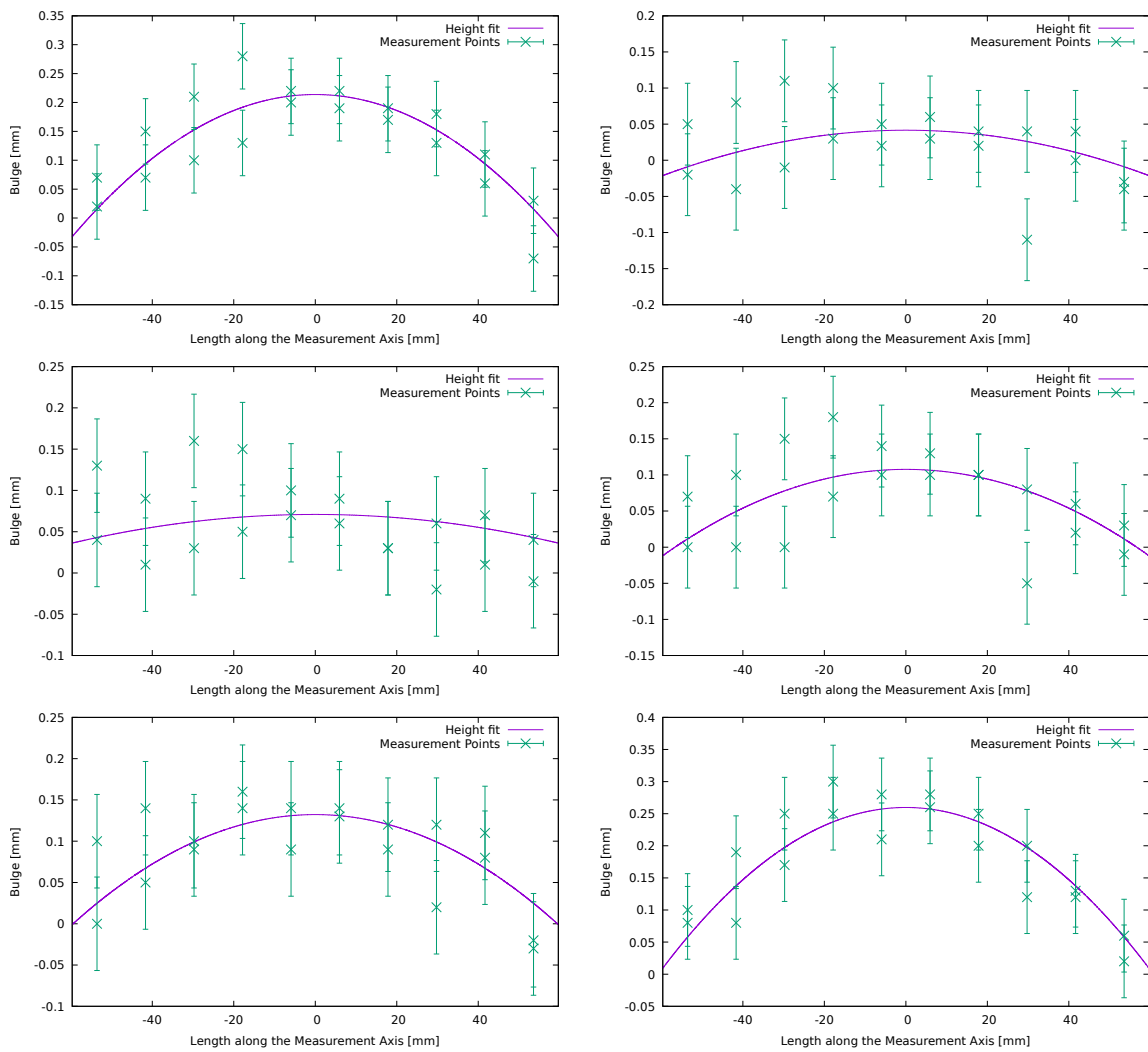
Figure A.1: The model for the bulging of the foil segments applied to the data obtained for the short cross-sections of window segment 3 in [Fab21]. The gas flows are different for the different plots.
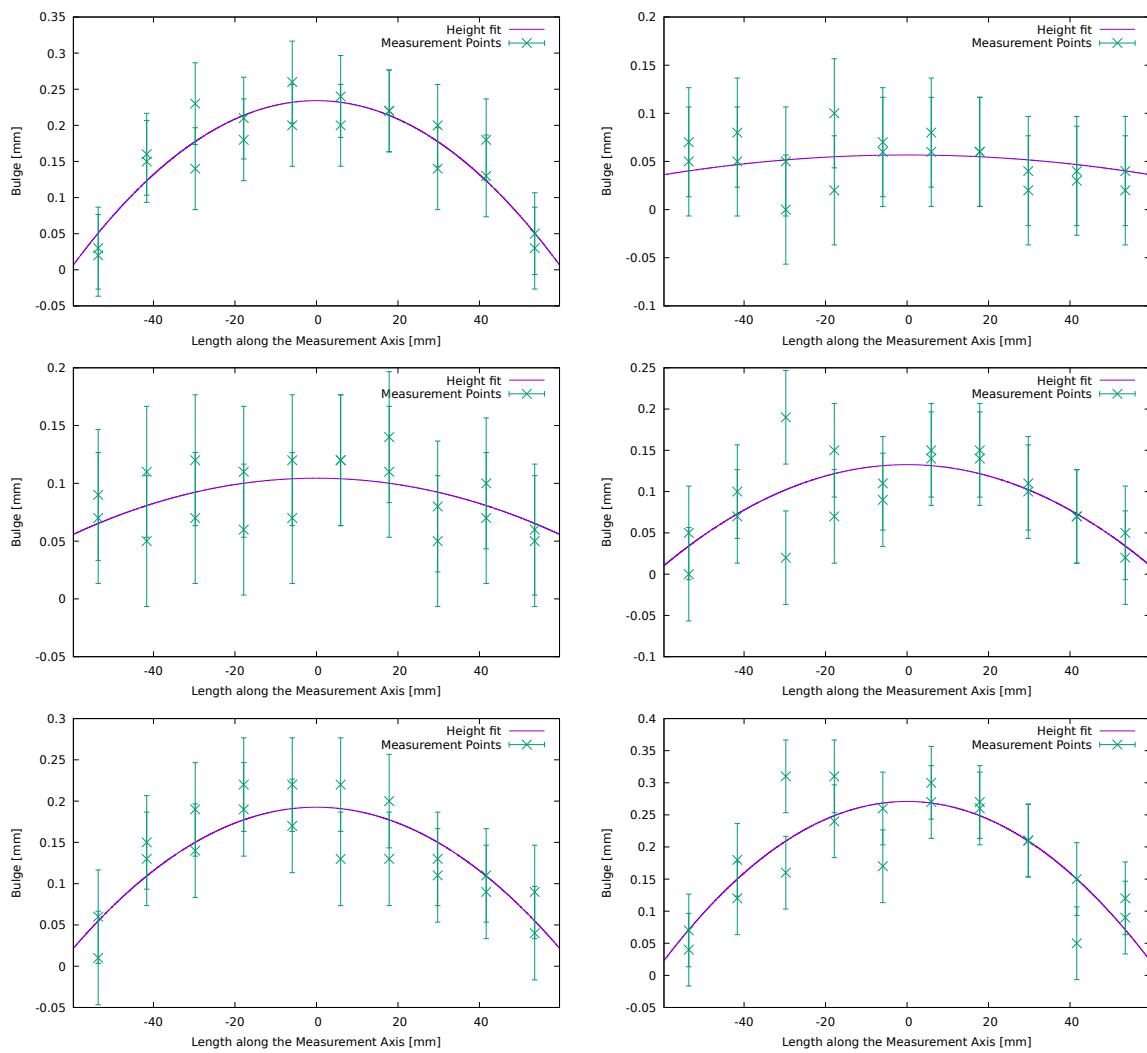
Figure A.2: The model for the bulging of the foil segments applied to the data obtained for the short cross-sections of window segment 2 in [Fab21]. The gas flows are different for the different plots.
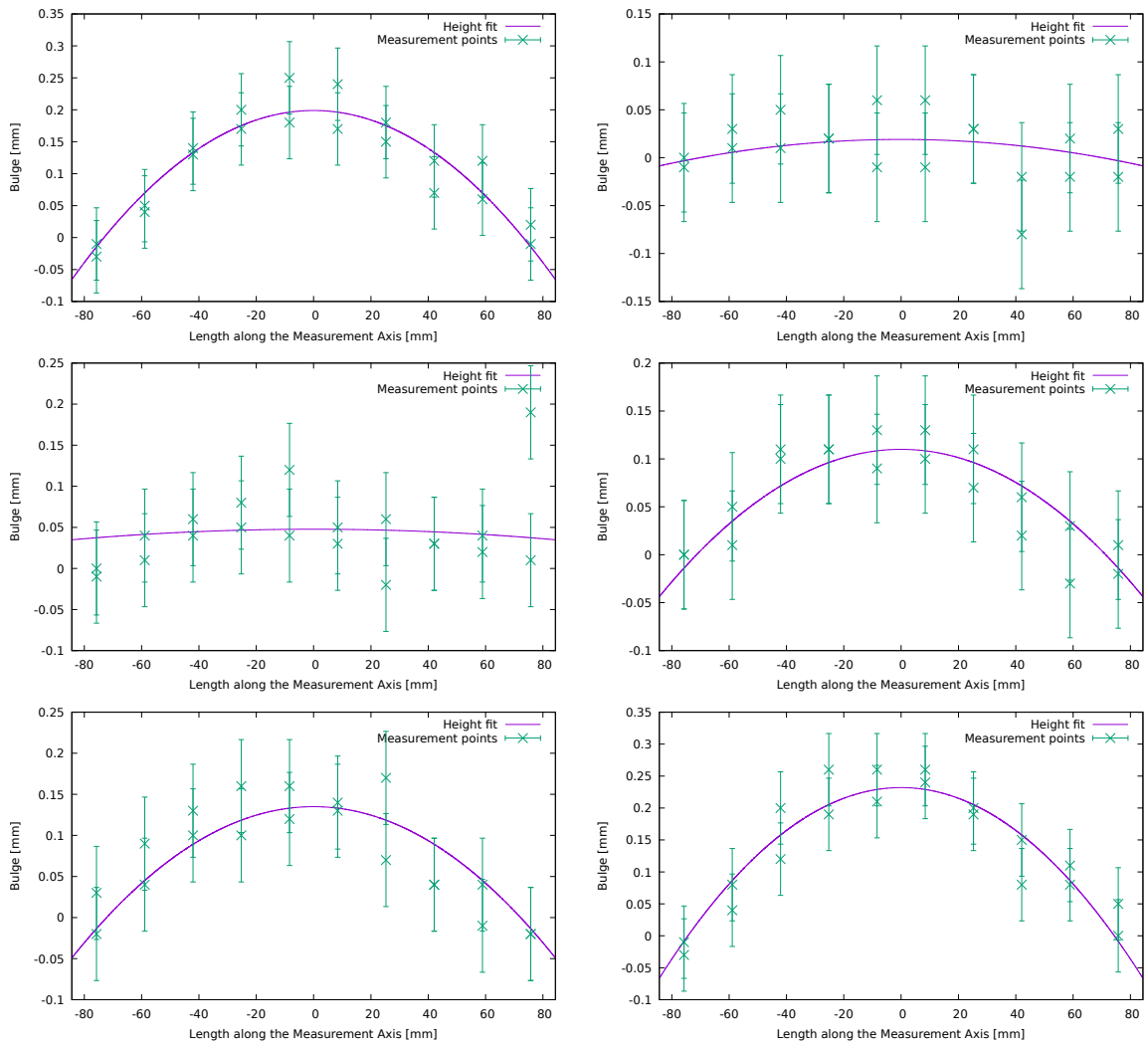
Figure A.3: The model for the bulging of the foil segments applied to the data obtained for the diagonal cross-sections of window segment 3 in [Fab21]. The gas flows are different for the different plots.
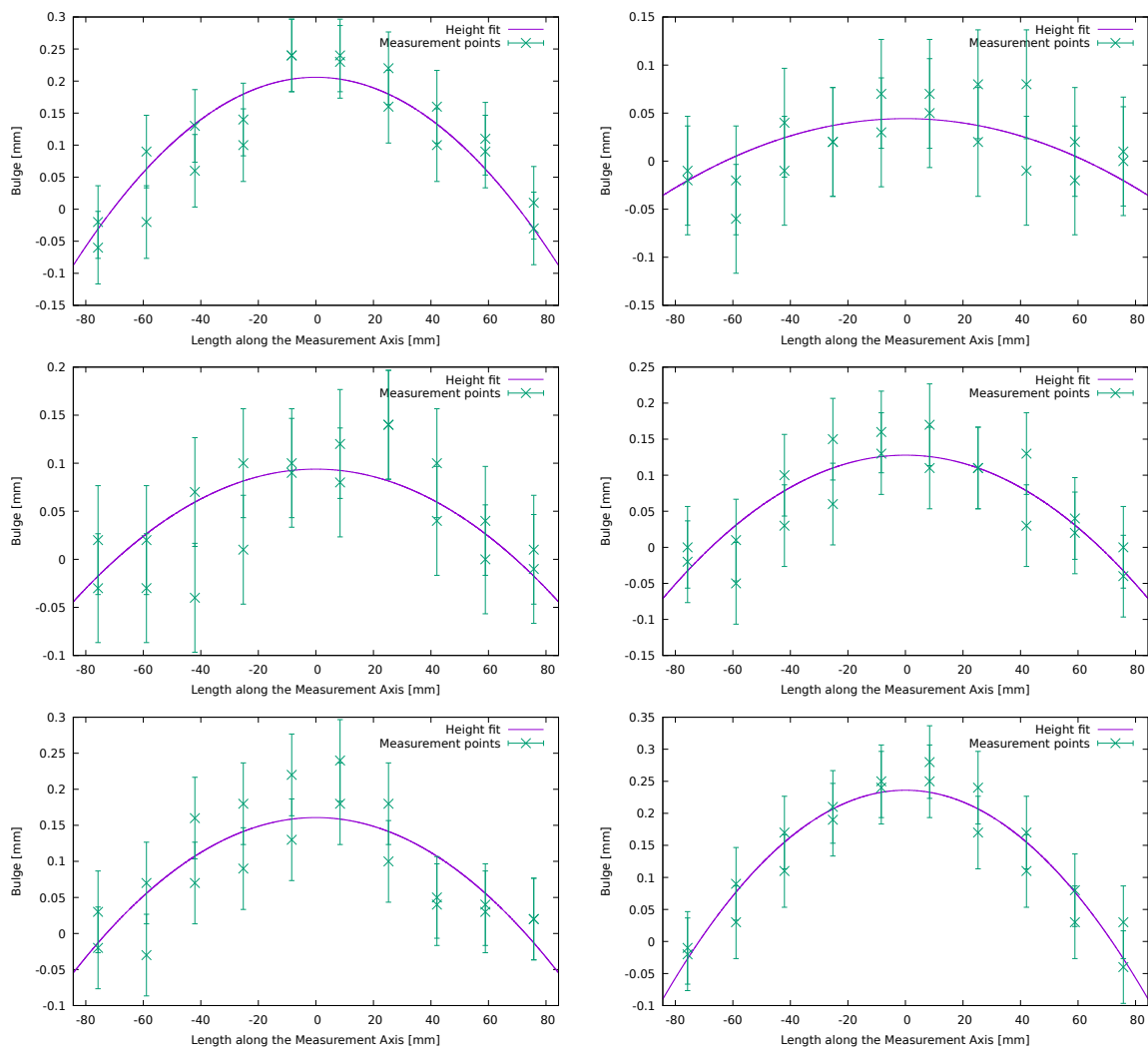
Figure A.4: The model for the bulging of the foil segments applied to the data obtained for the diagonal cross-sections of window segment 2 in [Fab21]. The gas flows are different for the different plots.

A.2 Grid Bulging
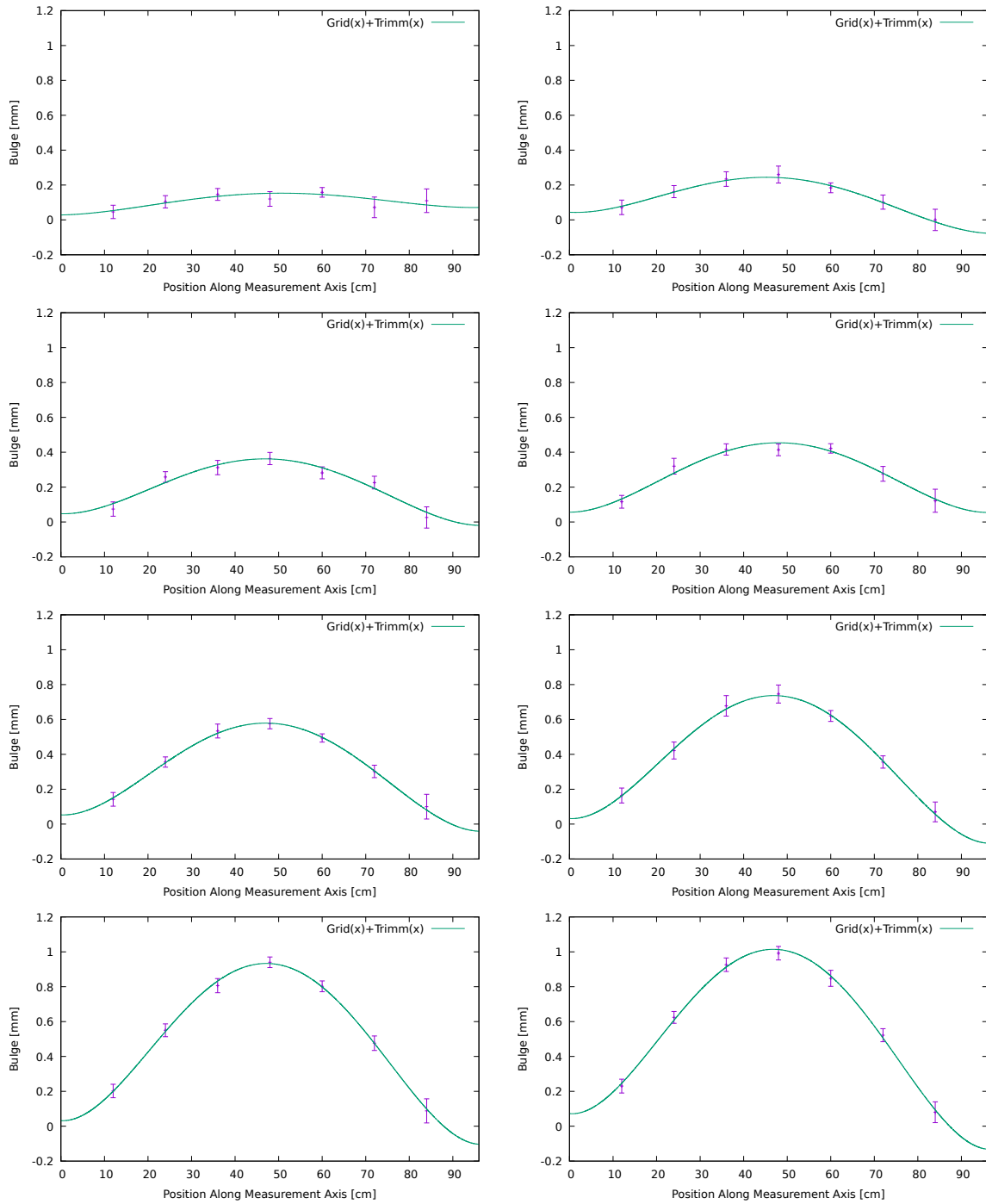
Figure A.5: Equation (3.18) applied to all data for the horizontal bulging of the grid, measured in [Fab21, p.48, sec.5.2.1.4]. The differential pressure applied to the module varies for the displayed plots.
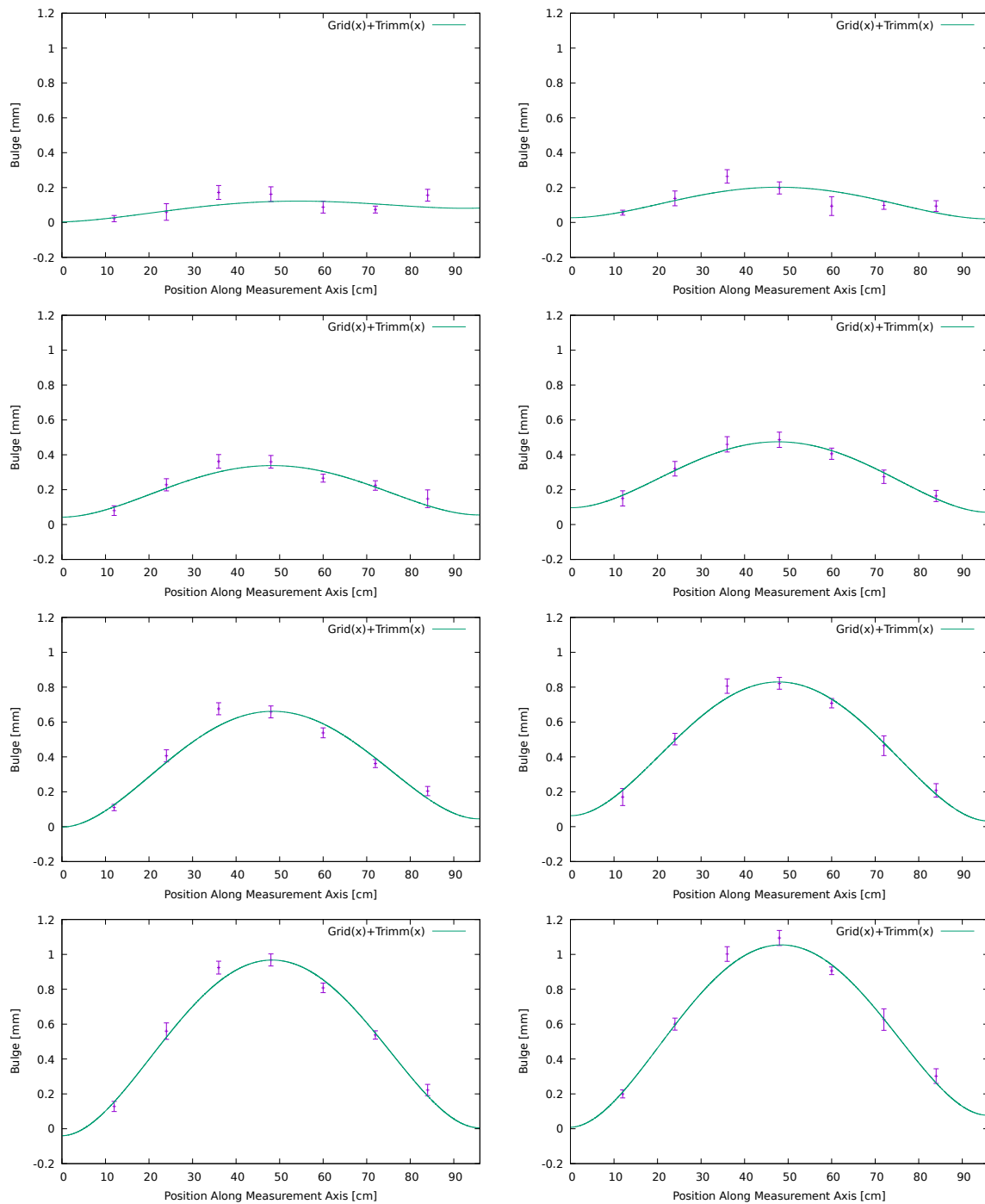
Figure A.6: Equation (3.18) applied to all data for the vertical bulging of the grid, measured in [Fab21, p.48, sec.5.2.1.4]. The differential pressure applied to the module varies for the displayed plots.

A.3 Leakage of the Entrance Window

The partial pressure for the upper limit of Xenon leakage determined in section 4.1 is based on the constant fit shown in fig. A.7.
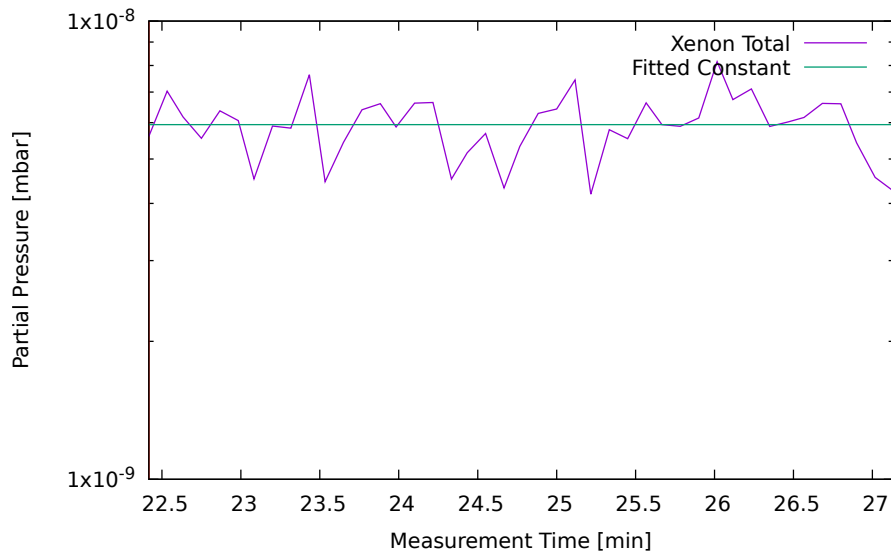
Figure A.7: A constant fit applied to the sum of the partial pressures associated masses of Xenon isotopes.

The constant fits, on which the values in table 4.1 are based on, are shown in fig. A.8.
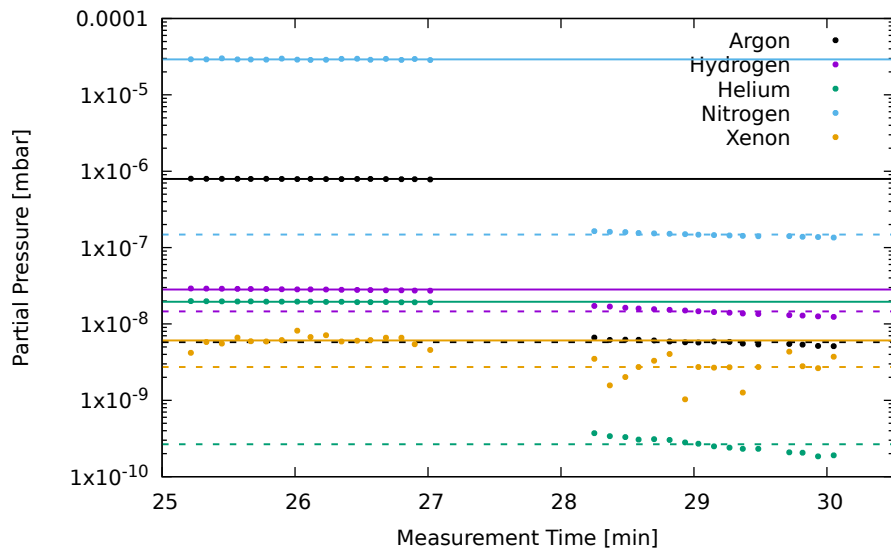
Figure A.8: The measurement values of the mass spectrometer before and after the cutoff of the membrane holder. Constant fits are applied to the data before and after the cutoff. The solid lines represent the constant fits before the membrane cutoff, the dashed lines the ones after. The line colors match the colors of the measurement points.

The determined constants are shown in table A.1. The fits that are the basis of table 4.2 are shown in fig. A.9.

Table A.1: The determined partial pressures before and after membrane cutoff for different gases. The values are the result of constant fits over two minutes before the membrane cutoff and two minutes after a one-minute-break after membrane cutoff. The fits and determined partial pressures are shown in fig. A.8. The unexpected peaks at 29.6 min measurement time are neglected in the fits.

Gas	Part. Press. Before [mbar]	Part. Press. After [mbar]
Argon	$(7.91 \pm 0.01) \cdot 10^{-7}$	$(5.77 \pm 0.11) \cdot 10^{-9}$
Hydrogen	$(2.82 \pm 0.01) \cdot 10^{-8}$	$(1.46 \pm 0.04) \cdot 10^{-8}$
Helium	$(1.95 \pm 0.01) \cdot 10^{-8}$	$(2.66 \pm 0.14) \cdot 10^{-10}$
Nitrogen	$(2.92 \pm 0.01) \cdot 10^{-5}$	$(1.48 \pm 0.02) \cdot 10^{-7}$
Xenon	$(6.08 \pm 0.22) \cdot 10^{-9}$	$(2.73 \pm 0.23) \cdot 10^{-9}$
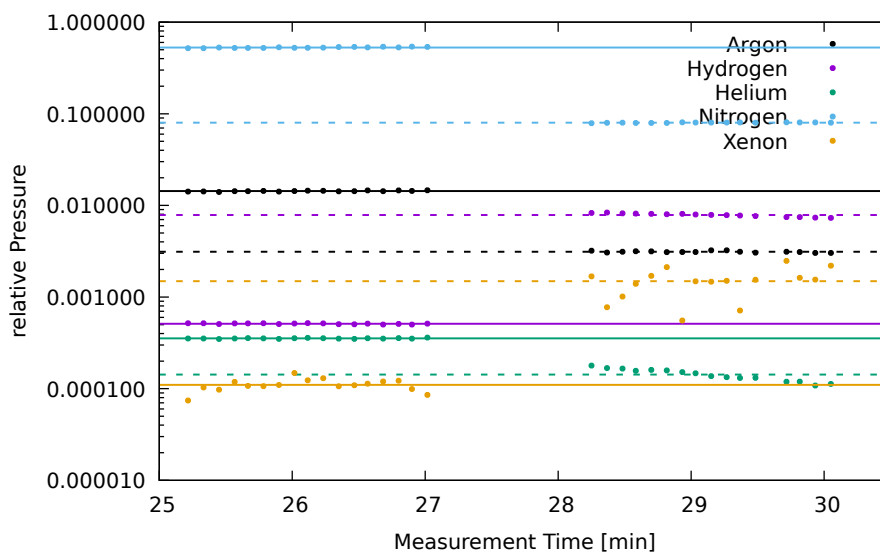
Figure A.9: The measurement values of the mass spectrometer before and after the cutoff of the membrane holder. Constant fits are applied to the data before and after the cutoff. The solid lines represent the constant fits before the membrane cutoff, the dashed lines the ones after. The line colors match the colors of the measurement points. The relative pressures shown are the ratio between partial pressure of the specific element and the sum of all partial pressures in the respective time step.

A.4 Overpressure Decay Measurement Setup

A.4.1 Readout-On-Request Necessity

In general, the readout of the Arduino could be done by writing the sensor data obtained to the serial port connected to the computer with a predefined frequency, e.g. every second. The computer would collect the data by reading the serial port. However, this
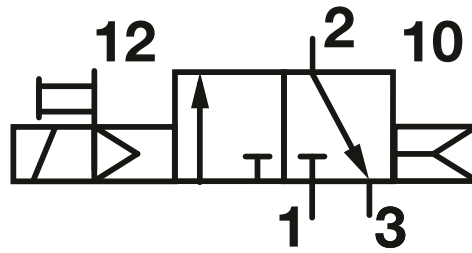
Figure A.10: Symbol of the inner workings of the *Norgren* 3/2 directional valves used in this setup [Nor15, p.2].

is not feasible, if multiple Arduinos are used or the length of a readout cycle varies. This is because the Arduino has a buffer for characters written to the serial port. If the Arduino writes the data more frequently than they are collected by the computer, this buffer fills up quickly. The readout of this buffer is based on the first in, first out method. Therefore, if the buffer is full, the computer obtains outdated data from the Arduino. Especially for the control of the valves in the offset measurements described in section 4.4, this is problematic. Because of the small volume of this system, even a short delay leads to the overpressure surpassing the abort threshold, before valve 0 is closed.

To avoid this issue, all Arduinos used in this setup only read out the connected sensors if they receive a ping from the computer.

A.4.2 Valve Controller

The pressured air controlled gas valves are build in-house. The valves are closed, when no pressured air is applied to them. The air flow is managed by *Norgren V60A413A-A2* 3/2 directional control valves. These valves are actuated by solenoids and air springs. The right side of fig. A.10 shows the valve position if no power is provided to the solenoid. Port 2 of the valve is connected to port 3. If power is applied to the solenoid, port 1 is connected to port 2, as shown on the left side of fig. A.10. The switching of positions only works, if pressured air is supplied to this directional valve.

The gas valve is connected to port 2 of the *Norgren* valve. The air supply is connected to port 1 and set to a pressure of 4 bar, well within the operation pressure of the *Norgren* valves of 2 bar to 10 bar [Nor15, p.2]. Port 3 only serves as an outlet.

This connection scheme results in the gas valve being closed if no power is provided to the solenoid. The gas valve opens, if the solenoid is powered.

Said solenoids use standard line voltage and consume 5 W of power. The voltage is

controlled by a 4-channel relay. Both, the connection of line conductor and neutral are switched, when a valve is addressed. The connections to line power are suitably fused. The relay is connected to an *Arduino Uno*. The switches are controlled using the digital pins of said *Arduino*. As all other *Arduinos* used in this setup, the valve control Arduino is addressed every readout cycle to ensure ongoing operation.

Further details of the valve control unit are available at the electrical workshop of the Institut für Kernphysik Münster, for the order numbered *2102000003*. A sample software is also available but does not feature the readout-on-request functionality necessary for some setups. The software used in this thesis will be provided to the team in Münster.

A.4.3 Absolute Pressure and Temperature Sensor

The absolute pressure and temperature sensors are connected to the *Arduino Uno* using the digital I²C protocol. More precisely, the pressure sensor is connected to the ADC and the ADC is connected to the Arduino. The exact circuit and a sample software for the Arduino involved are available at the electrical workshop of the Institut für Kernphysik Münster, for the order numbered *2102000003*. Note that the software provided does not calculate the absolute pressure correctly, because of precision limitations of the Arduino. Additionally, the readout-on-request functionality is highly recommended for this sensor. The software used in this thesis will be provided to the team in Münster.

A.4.4 Readings of Different Temperature Sensors

Figure A.11 shows the readings of the temperature sensor included with the ambient pressure sensor, the *Orbisphere* and an external sensor produced by *PeakTech*. The model used is the *PeakTech 5185* ambient data logger. The accuracy of this sensor is specified to be $0.3\,°C$ [Pea21, p.16] at a resolution of $0.1\,°C$. The recommended recalibration interval is $1\,year$ [Pea21, p.36]. This particular unit was not calibrated in at least $5\,years$. However, as can be seen in fig. A.11, the values of *Orbisphere* and *PeakTech* sensor are only divided by an offset of about $0.8\,°C$. The observed trends are identical. Similarly, the temperature sensor enclosed in the housing with the absolute pressure sensor observes the same trends, while being limited by the resolution of the sensor of $0.5\,°C$. The offset between this sensor and the *Orbisphere* readings visible in
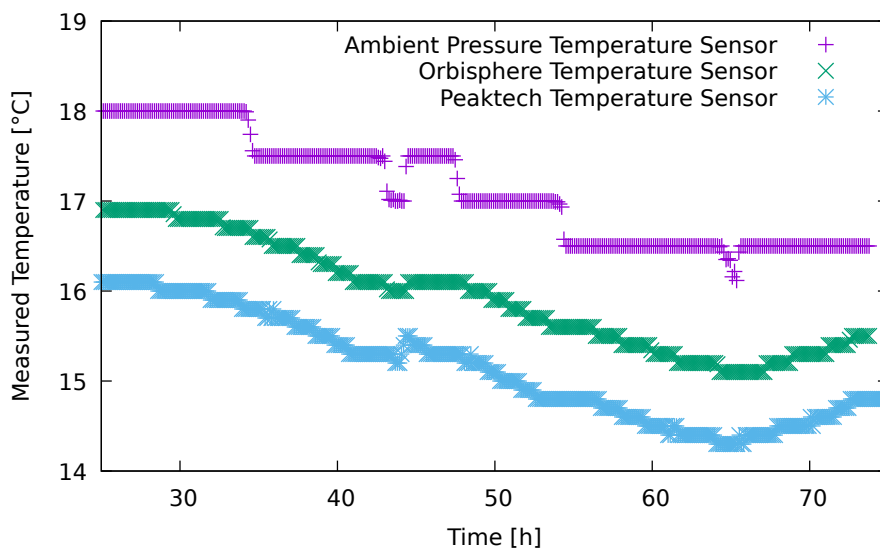
Figure A.11: The readings of the different temperature sensors over time. The readings for the ambient pressure and *Orbisphere* temperature sensor are averaged over 60 consecutive values. The *PeakTech* readings are not averaged. For *Orbisphere* and absolute pressure sensor, every fourth value is shown. For the *Peaktech* sensor every eighth reading is plotted. Uncertainties are not shown to keep the data visible.

fig. A.11 might be a result of the electrical power heating up the enclosure.

Regardless of these observations, using the temperature output of the *Orbisphere* for most of the conducted analysis is valid. The temperature reading is off by a constant offset at worst. This would have an impact on the uncertainties of the differential pressure sensor, as discussed in section 4.3.2. However, even if the offset is $1\,^{\circ}\mathrm{C}$ this would only add an uncertainty of $0.004\,\mathrm{mbar}$, as described in section 4.3.2, in a worst case scenario. Depending on the direction of the offset and the temperature value obtained, the uncertainty might even be overestimated due to this discrepancy.

A.5 Offset Measurement

The linear description of the measurement data works for most measurement cycles. In rare instances, unpredicted developments occur. Some of these instances are shown in the following figures. The plotted data points are averages over 60 measurement points. The uncertainty is determined as described in section 3.13. Linear fits are applied to the data.
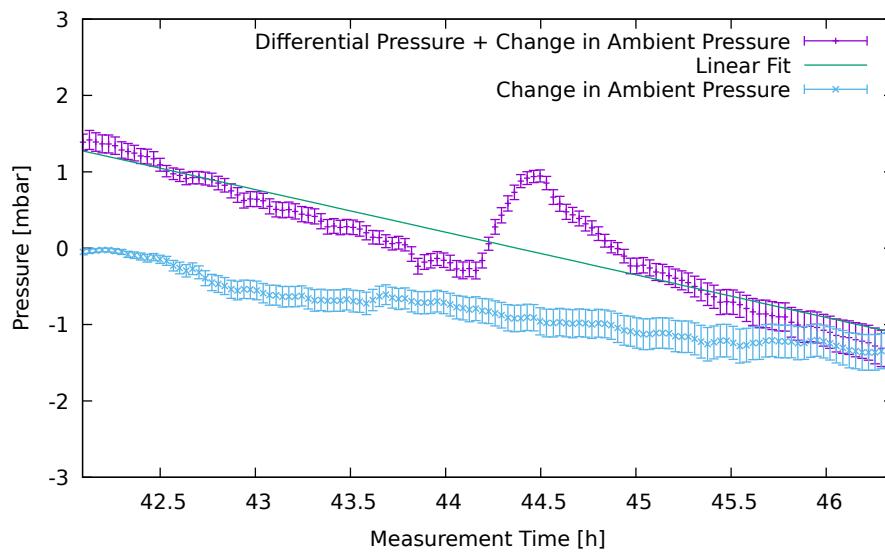
Figure A.13: A cycle of the second offset measurement. An unexpected peak appears halfway through the decay. No explanation for this behavior is documented. The differential pressure sensor might have been moved, leading to a change in barometric pressure on one side of the differential pressure, unaccounted for by the ambient pressure sensor.
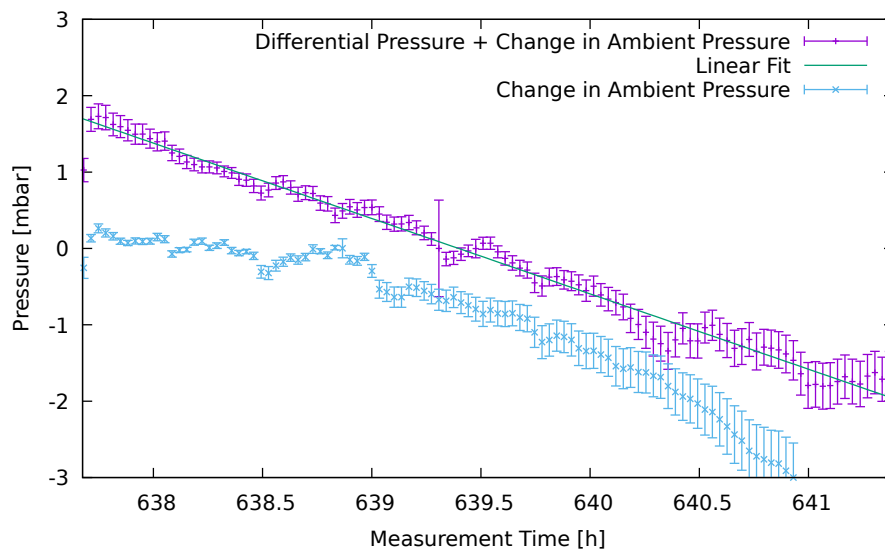
Figure A.12: A regular cycle of the second offset measurement. The data are unusually noisy, deviating in both directions from the clear linear decay observed in other cycles.

A.5.1 Temperature Dependency
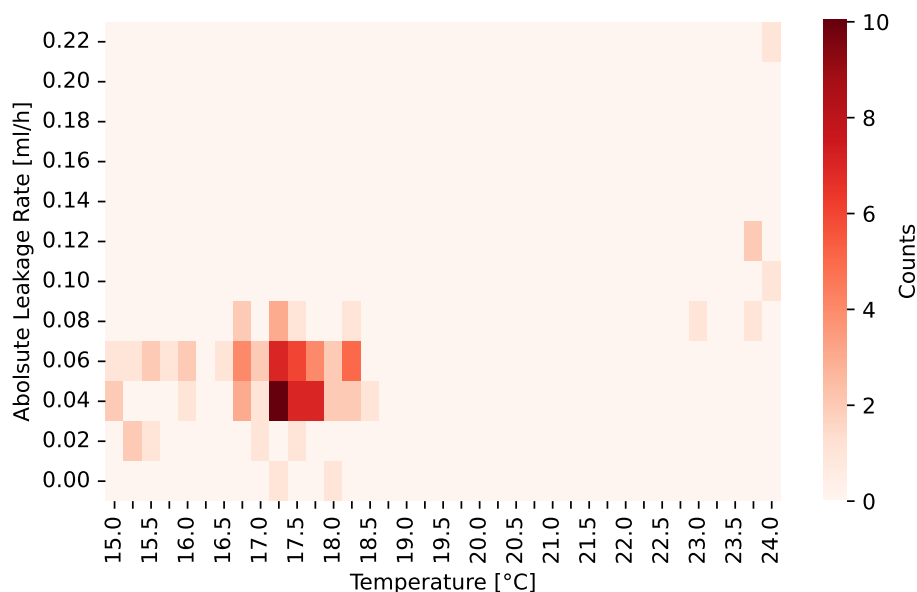
Figure A.14: The plot shown in fig. 4.20 as a heat map. Instead of the signed leakage rate, the absolute leakage rate is shown.

A.6 Leakage of the Investigated Prototype

The fit parameters of the exponential decay fitted to the data in section 4.5 are shown in fig. A.15, fig. A.16 and fig. A.18. Both, the determined offsets and the determined overpressures at the beginning of the measurement are in the expected range, as visible in fig. A.16 and fig. A.15. The overpressure at the start of the measurement is slightly lower than the minimum target of 0.95 mbar for the first forty measurement cycles. This is due to an over estimation of the overpressure by the differential pressure sensor, as can be seen in fig. A.16. For the cycles in question, the determined offset is in a positive range. Since this offset is defined by the pressure equilibrium reached at the end of a measurement cycle, this is to be interpreted as a true zero for the differential pressure. A positive offset therefore means the discussed overestimation, which leads to the lower overpressure actually reached and shown in fig. A.15.

The same is true for the remaining measurement cycles, but instead of an overestimation, the sensor underestimates the differential pressure, leading to higher differential pressures at the beginning of a measurement.

To account for these kinds of offset, a zero-differential-pressure measurement was conducted, as discussed in section 4.3.2. The reason this measurement does not compensate
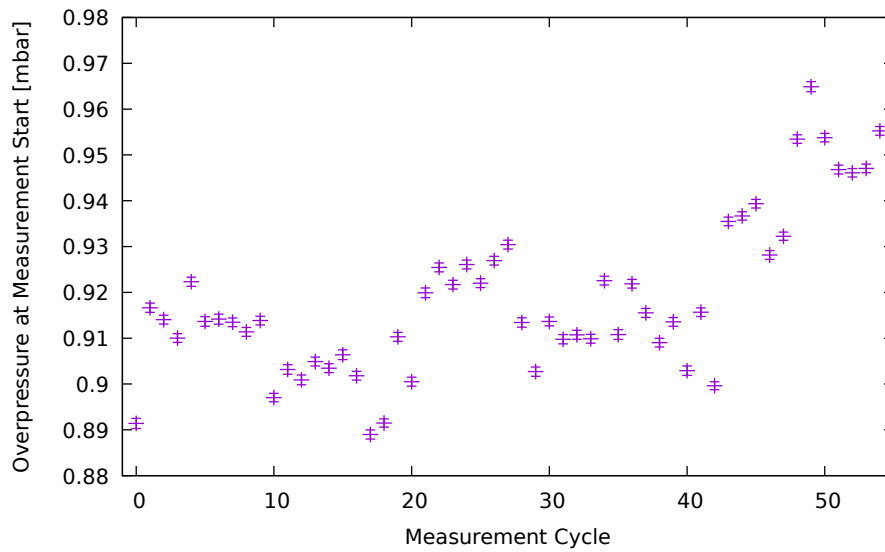
Figure A.15: The overpressures at the beginning of the measurement cycles determined by the exponential fit in eq. (4.18).
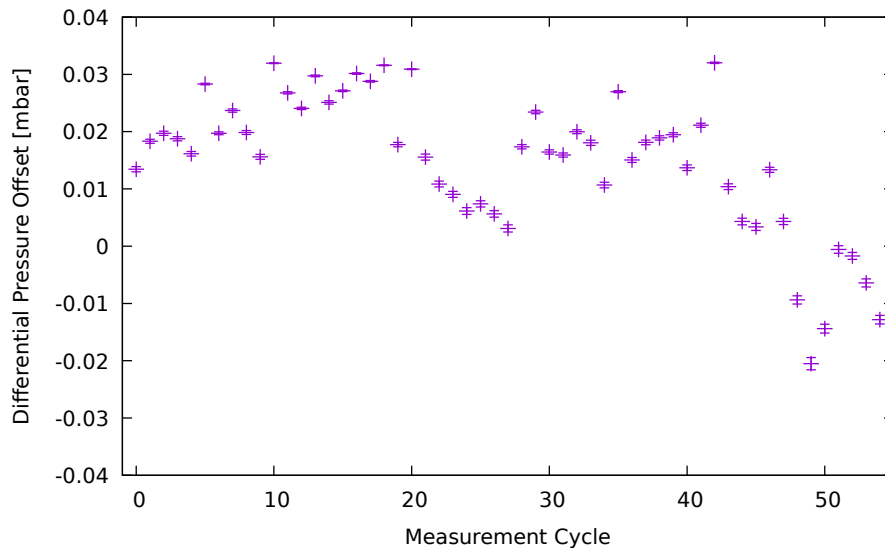
**Figure A.16:** The offset pressure reached towards the end of each measurement cycle determined by fit.
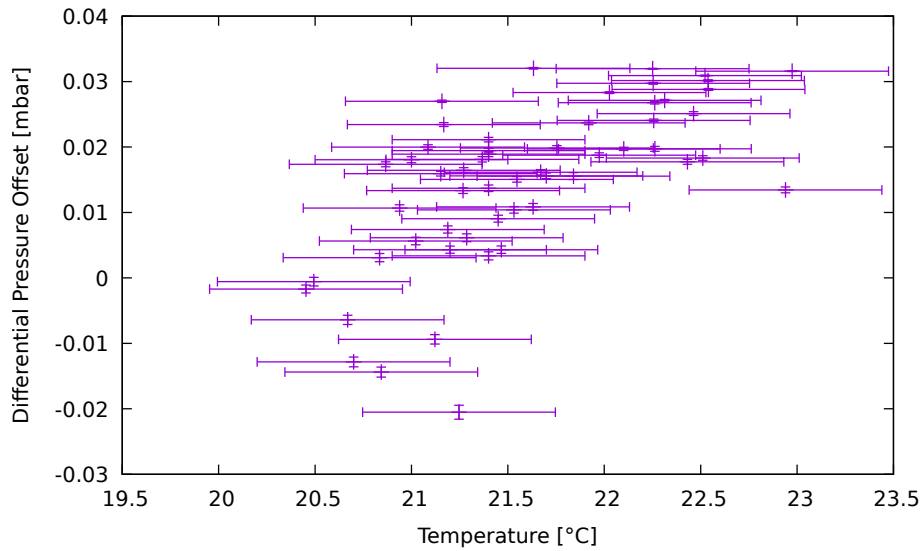
Figure A.17: The differential pressure offset as a function of the average temperature reading of the *Orbisphere*. The uncertainties of the temperature are calculated as discussed in section 3.13 and section 4.3.4. The systematic uncertainties predominate. The uncertainty of the offset is out put by *gnuplot*.

the offset for most measurement cycles most likely is the change in temperature. This is visible in fig. A.17. Regardless of the discussed dependency and differences between the cycles, the offset is smaller than the one ADC-unit corresponding to 0.04 mbar. The setup behaves as expected and the fit parameters reflect this fact. The determined decay rates shown in fig. A.18 are discussed in section 4.5 after conversion into leakage rates, using eq. (3.11).
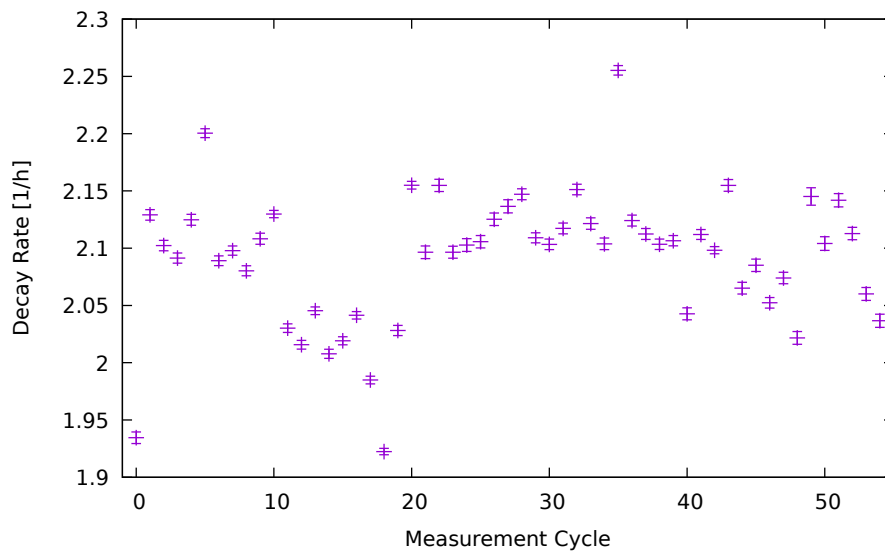
Figure A.18: The decay parameter λ for each measurement cycle. The uncertainties are output by *gnuplot*.

A.6.1 Temperature Dependencies
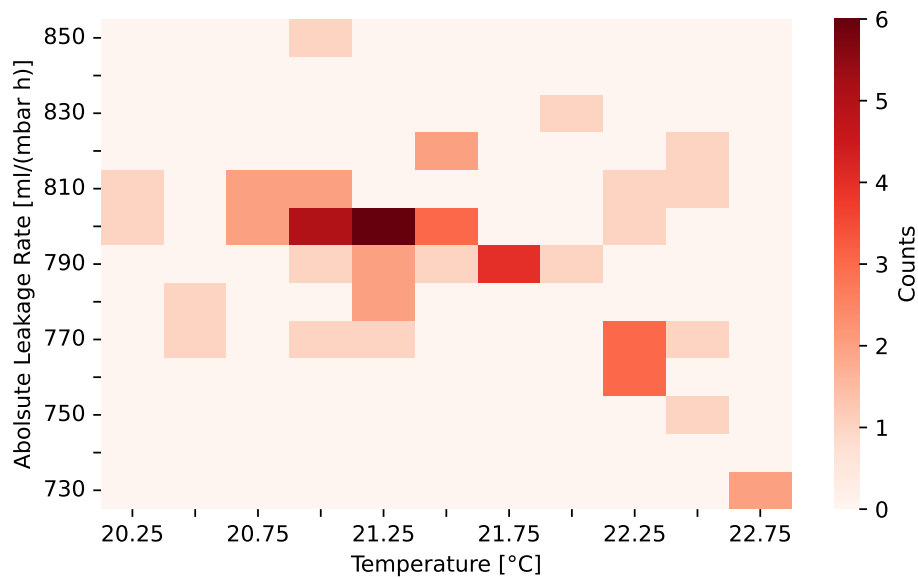
Figure A.19: Figure 4.24 as a heat map. The bin-width in y-direction is $10\,\frac{\mathrm{mL}}{\mathrm{mbar\cdot h}}$. The one in x-direction is $0.25\,°\mathrm{C}$. This figure changed due to the error discussed in chapter 1.

A.7 Tape(-Removal) Measurements

The fit parameters of the exponential fits applied to the data are shown in fig. A.20, fig. A.23, fig. A.21, fig. A.24, fig. A.22 and fig. A.25.
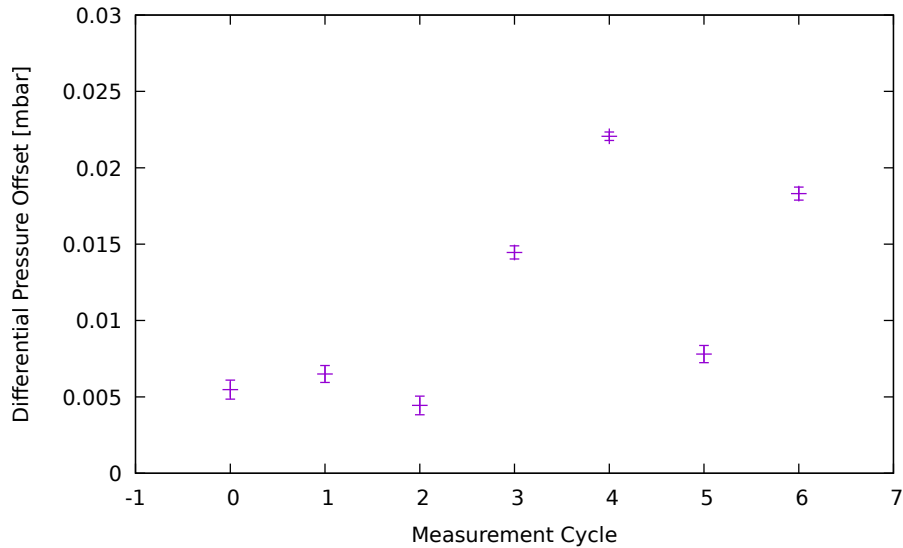
Figure A.20: The determined differential pressure offsets for each measurement cycle of the measurement without the *Kapton* tape in place. The uncertainties are output by *gnuplot*.
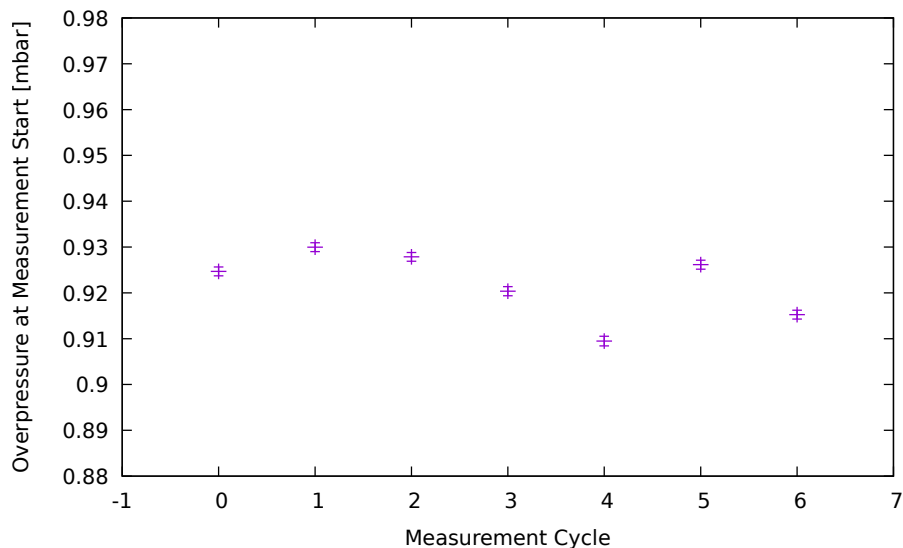
Figure A.21: The differential pressure at the start of each measurement cycle determined by the exponential fit for the measurement without the *Kapton* tape attached to the prototype. The uncertainties are output by *gnuplot*.
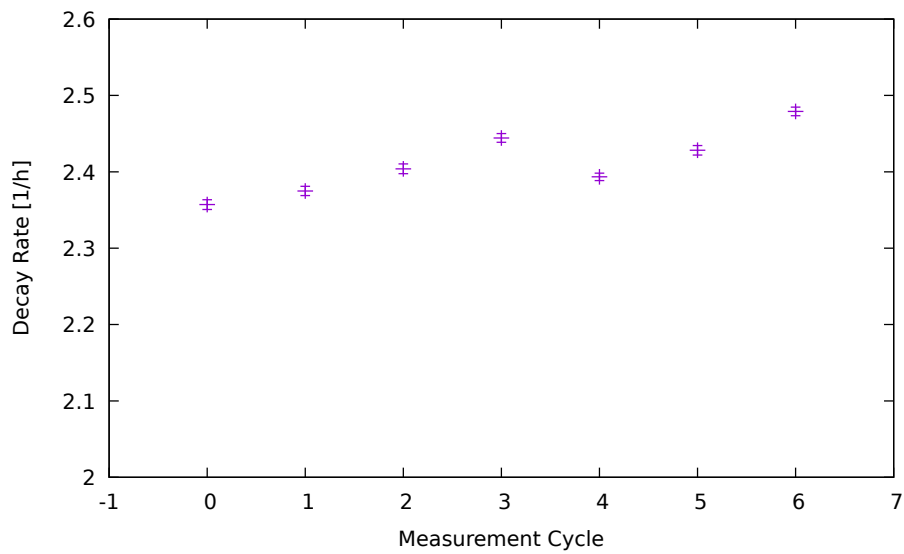
Figure A.22: The determined decay rates λ for each measurement cycle of the prototype measurement without the *Kapton* tape. The uncertainties are output by *gnuplot*.
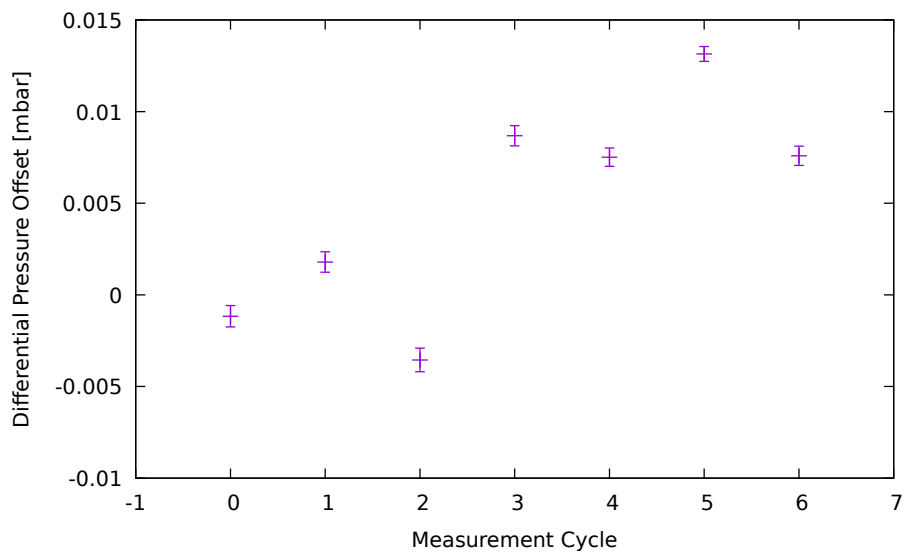
Figure A.23: The determined differential pressure offsets for each measurement cycle of the measurement with the residue free tape in place. The uncertainties are output by *gnuplot*.
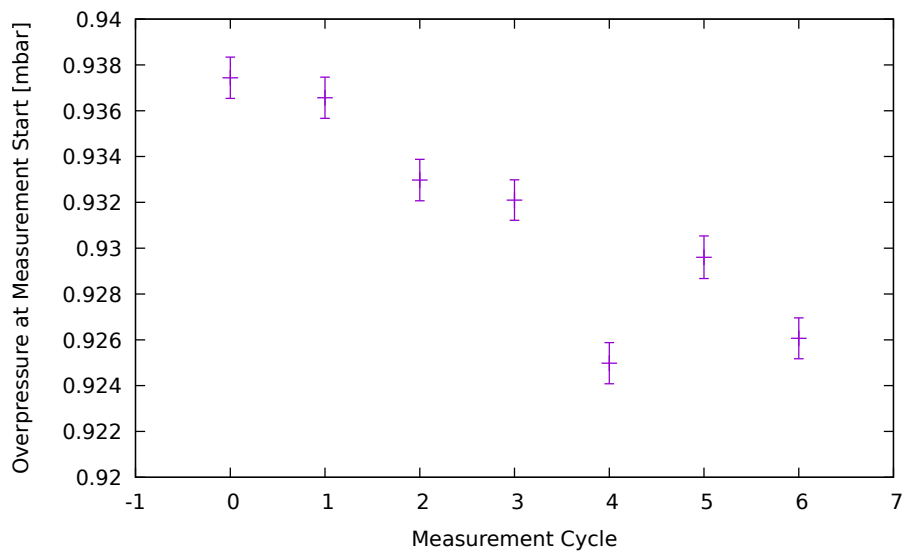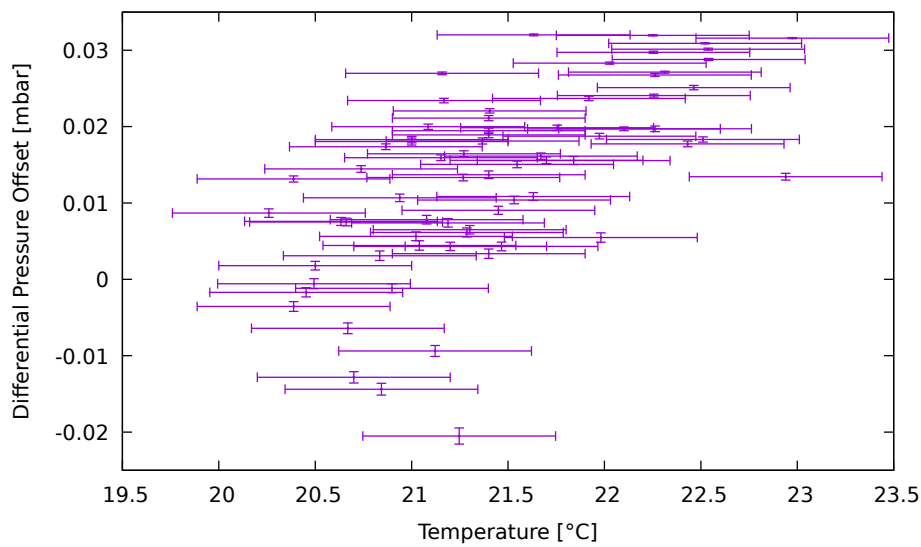
Figure A.24: The differential pressure at the start of each measurement cycle determined by the exponential fit for the measurement with the residue free tape attached to the prototype. The uncertainties are output by *gnuplot.*
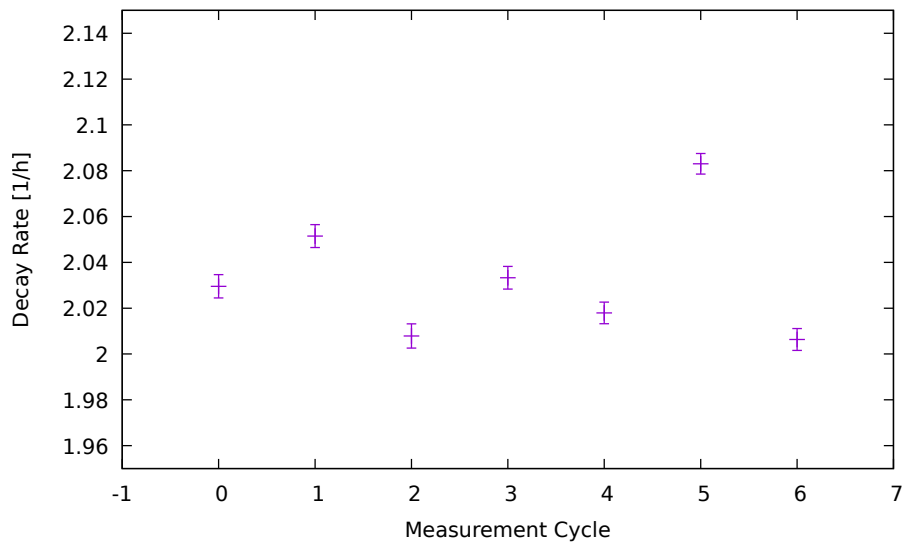

Figure A.25: The determined decay rates λ for each measurement cycle of the prototype measurement without the residue free tape. The uncertainties are output by *gnuplot.*

The results need no further discussion beyond the findings in appendix A.6 and section 4.6. The data obtained from the location measurement involving the removal and reapplying of plastic tape to the module fit in with the temperature dependency of the differential pressure offset shown in fig. A.17. The combined correlation plot is shown in fig. A.26.
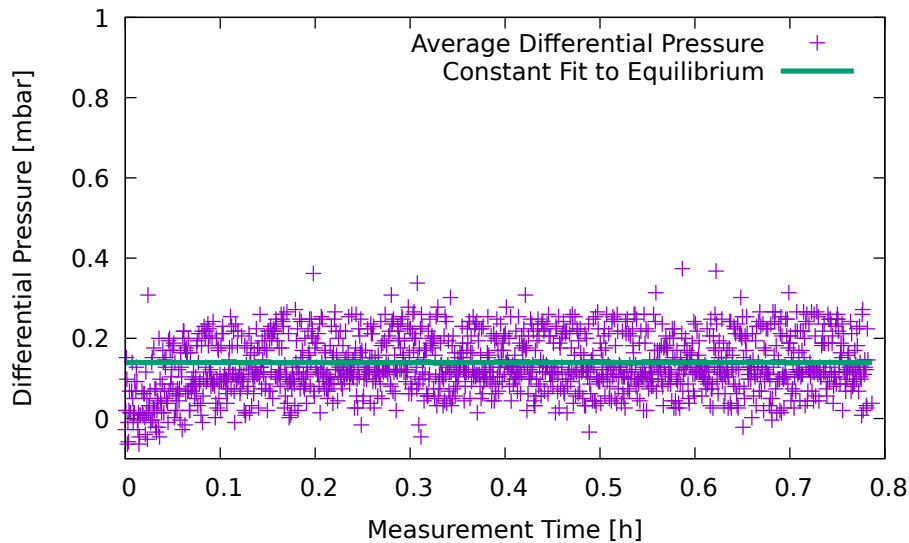
Figure A.26: The offset of the differential pressure sensor and the respective average temperature reading from the *Orbisphere* for each measurement cycle of all overpressure decay measurements conducted with the TRD prototype. A heat map of this plot is shown in fig. A.27.
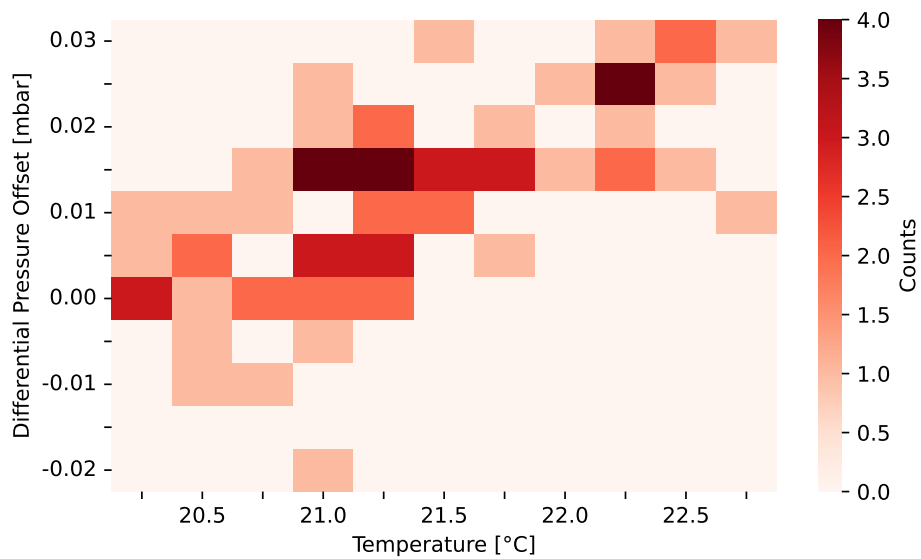

Figure A.27: Figure A.26 as a heat map. The bin-width in x-direction is $0.25\,°\text{C}$. The one in y-direction is $0.005\,\text{mbar}$.

A.8 Repairability of a TRD Test-Module

Figure A.28: The differential pressure over measurement time at a gas flow of $3\frac{\text{L}}{\text{h}}$. The displayed pressure is the average output of all four differential pressure sensors included in this setup. The readings are corrected by the measured offset for each sensor before averaging. The constant is fittet to the data points in the time interval between $0.3\,\text{h}$ and $1\,\text{h}$. Only every second measurement point is shown.
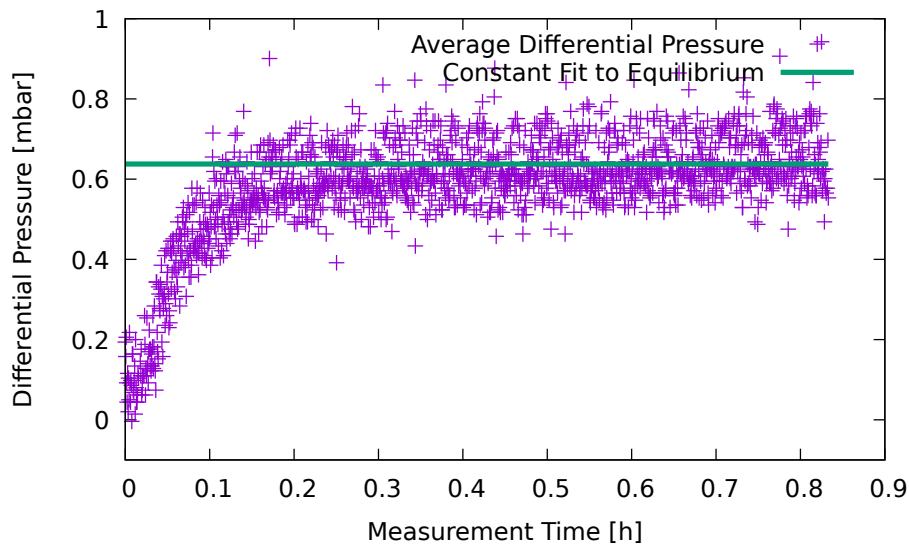
Figure A.29: The differential pressure over measurement time at a gas flow of $7\frac{\text{L}}{\text{h}}$. The displayed pressure is the average output of all four differential pressure sensors included in this setup. The readings are corrected by the measured offset for each sensor before averaging. The constant is fittet to the data points in the time interval between $0.3\,\text{h}$ and $1\,\text{h}$. Only every second measurement point is shown.
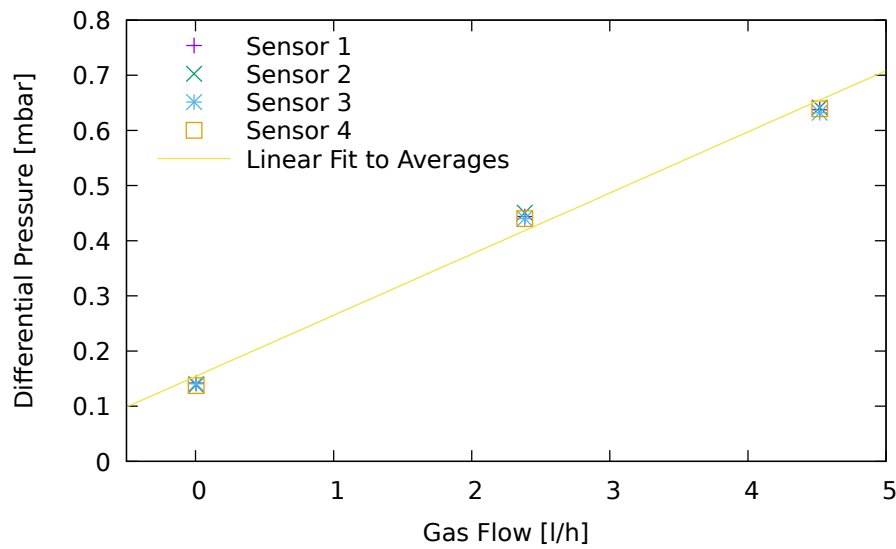
Figure A.30: Figure 4.36 with the individual sensor data instead of the average over all sensors. The equilibriums are determined by constant fits to the sensor readings in the time interval between $0.3\,$h and $1\,$h. The linear fit is taken from fig. 4.36. The sensor naming scheme is not necessarily the same as used in fig. 4.37. The difference in sensor readings observed in fig. 4.37 are not present in this measurement.

Abbreviations

QCD   *Quantum Chromodynamics*

FAIR   *Facility for Antiproton and Ion Research*

GSI   *GSI Helmholtzzentrum für Schwerionenforschung*

MVD   Micro-Vertex Detector

STS   Silicon Tracking System

RICH   Ring Imaging Cherenkov Detector

MUCH Muon Chamber System

TOF   Time-of-Flight System

PSD   Projectile Spectator Detector

MWPC Multi Wire Proportional Chamber

TRD   Transition Radiation Detector

TR   Transition Radiation

PCB   Printed Circuit Board

ADC   Analog-to-Digital Converter

CBM   *Compressed Baryonic Matter*

QGP   Quark Gluon Plasma

ALICE *A Large Ion Collider Experiment*

UHV   Ultrahigh Vacuum

PE   Polyethylene

Bibliography

[AYM75] X. Artru, G. B. Yodh, and G. Mennessier. "Practical theory of the multi-layered transition radiation detector". In: *Phys. Rev. D* 12 (5 Sept. 1975), pp. 1289–1306. DOI: `10.1103/PhysRevD.12.1289`. URL: `https://link.aps.org/doi/10.1103/PhysRevD.12.1289`.

[OBr+93] E. O'Brien et al. "A transition radiation detector which features accurate tracking and dE/dx particle identification". In: *IEEE Transactions on Nuclear Science* 40.2 (1993), pp. 153–157. DOI: `10.1109/23.212332`.

[96] *LM75 I2C Digital Temperature Sensor and Thermal Watchdog.* National Semiconductor Corporation. 1996.

[99] *Bedienungsanleitung GAS-CHECK 5000is.* User manual for the *GAS-CHECK 5000* gas detectors. ISM GmbH. 1999.

[Dea99] John A. Dean. *LANGE'S HANDBOOK OF CHEMISTRY*. 15th ed. McGraw-Hill, Inc., 1999. ISBN: 0-07-016384-7.

[Cor01] P Cortese. *ALICE transition-radiation detector: Technical Design Report.* Technical design report. ALICE. Geneva: CERN, 2001. URL: `https://cds.cern.ch/record/519145`.

[Kir06] James Kirchner. "Data Analysis Toolkit #12: Weighted averages and their uncertainties". Script of Prof. James Kirchner regarding weighted averages. 2006. URL: `http://seismo.berkeley.edu/~kirchner/Toolkits/Toolkit_12.pdf`.

[Lui08] Walter Blum Luigi Rolandi Werner Riegler. *Particle Detection with Drift Chambers.* 2nd ed. Springer Berlin, Heidelberg, 2008. ISBN: 978-3-540-76683-4. URL: `https://doi.org/10.1007/978-3-540-76684-1`.

[Heu09] Johann M. Heuser. "The Compressed Baryonic Matter Experiment at FAIR: Progress with feasibility studies and detector developments". In: *Nuclear Physics A* 830.1-4 (Nov. 2009), pp. 563c–566c. DOI: `10.1016/j.nuclphysa.2009.09.048`. URL: `https://doi.org/10.1016%2Fj.nuclphysa.2009.09.048`.

[09]   *ORBISPHERE Model 31xxx Electrochemical Sensors. INSTALLATION and MAINTENANCE MANUAL.* Revision H. Hach Company/Hach Lange GmbH. May 2009.

[AW12]   A. Andronic and J.P. Wessels. "Transition radiation detectors". In: *Nuclear Instruments and Methods in Physics Research Section A: Accelerators, Spectrometers, Detectors and Associated Equipment* 666 (Feb. 2012), pp. 130–147. DOI: `10.1016/j.nima.2011.09.041`. URL: `https://doi.org/10.1016%2Fj.nima.2011.09.041`.

[Nol12]   Wolfgang Nolting. *Spezielle Relativitätstheorie, Thermodynamik.* 8th ed. Vol. 4. Grundkurs Theoretische Physik. Springer-Verlag Berlin Heidelberg, 2012. ISBN: 978-3-642-24480-3.

[Pit12]   Nora Pitz. "Gas system, gas quality monitor and detector control of the ALICE Transition Radiation Detector and studies for a pre-trigger data readout system". PhD thesis. Goethe Universität Frankfurt am Main, 2012.

[Dem14]   Wolfgang Demtröder. *Kern-, Teilchen- und Astrophysik.* 4th ed. Vol. 4. Experimentalphysik. Springer-Verlag Berlin Heidelberg, 2014. ISBN: 978-3-642-21475-2.

[Pov+14]   Bogdan Povh et al. *Teilchen und Kerne. Eine Einführung in die physikalischen Konzepte.* 9th ed. Springer-Verlag Berlin Heidelberg, 2014.

[Dem15]   Wolfgang Demtröder. *Mechanik und Wärme.* 7th ed. Vol. 1. Experimentalphysik. Springer-Verlag Berlin Heidelberg, 2015. ISBN: 978-3-662-46414-4.

[Nor15]   Norgren. *V60 ... V63, 3/2, 2 x 3/2, 5/2 or 5/3 Solenoid and pilot actuated spool valves.* Technical data sheet for the used directional valves. Review en 5.3.100.01. 2015.

[Dem16]   Wolfgang Demtröder. *Atome, Moleküle und Festkörper.* 5th ed. Vol. 3. Experimentalphysik. Springer-Verlag Berlin Heidelberg, 2016. ISBN: 978-3-662-49093-8.

[Her16]   Norbert Wermes Hermann Kolanoski. *Teilchendetektoren. Grundlagen und Anwendungen.* 1st ed. Springer Spektrum Berlin, Heidelberg, 2016. ISBN: 978-3-662-45349-0. URL: `https://doi.org/10.1007/978-3-662-45350-6`.

[Mas17]   Silvia Masciocchi. "Gaseous detectors". 39th Heidelberg Physics Graduate Days, HGSFP Heidelberg. 2017. URL: `https://www.physi.uni-heidelberg.de/~sma/teaching/GraduateDays2017/sma_Detectors_2_Gaseous.pdf`.

[BBE18]   *The Transition Radiation Detector of the CBM Experiment at FAIR : Technical Design Report for the CBM Transition Radiation Detector (TRD)*. Tech. rep. FAIR Technical Design Report. ccby4 "This work was supported in part by the GSI Helmholtzzentrum für Schwerionenforschung, Darmstadt,its $F\&E-cooperation$ contracts with Frankfurt and Münster, the Facility for Antiproton andIon Research (FAIR), the German BMBF-Verbundforschung (05P15RFFC1 and 05P16PMFC1),the EU FP6 and FP7 projects HadronPhysics2 (WP18 "FutureGas") and HadronPhysics3 (WP19 "FuturePID"), the Romanian ANCSI/CAPACITATI Modul III Contract F02, the NUCLEU Project Contract PN 09370103, the Hessian LOEWE initiative HICforFAIR and the ExtreMe Matter Institute EMMI at GSI.". Darmstadt, 2018, 165 p. DOI: `10.15120/GSI-2018-01091`. URL: `https://repository.gsi.de/record/217478`.

[Tan+18]   M. Tanabashi et al. "Review of Particle Physics". In: *Phys. Rev. D* 98 (3 Aug. 2018), p. 030001. DOI: `10.1103/PhysRevD.98.030001`. URL: `https://link.aps.org/doi/10.1103/PhysRevD.98.030001`.

[18]   "The ALICE Transition Radiation Detector: Construction, operation, and performance". In: *Nuclear Instruments and Methods in Physics Research Section A: Accelerators, Spectrometers, Detectors and Associated Equipment* 881 (Feb. 2018), pp. 88–127. DOI: `10.1016/j.nima.2017.09.028`. URL: `https://doi.org/10.1016%2Fj.nima.2017.09.028`.

[Web18]   Ruben Weber. "Humidity in the Gas System of the Transition Radiation Detector in the CBM Experiment". Bachelor's Thesis. 2018.

[Ble19]   T. Blesgen. "Einführung in die Variationsrechnung". Introductory lecture into calculus of variations, Justus-Liebig-University, Gießen, Germany. 2019.

[Gar19]   Chilo Garabatos. "Gas and Kr". TRD commissioning meeting. 2019.

[19]   *Oils / Greases / Lubricants*. Excerpt from the Leybold vacuum full line catalog. Leybold. Sept. 2019.

[20]   *144S...-PCB series - Signal conditioned precision compensated pressure sensors.* Preliminary data sheet for the 144S...-PCB series, received via E-Mail. First Sensor AG. Aug. 2020.

[Bon21a]   Daniel Bonaventura. "TRD Folienfenster. Lecktest, Kurzübersicht". A presentation concerning the investiagtion into foil leakage and subsequent questions, Münster, Germany. 2021.

[Bon21b]   Daniel Bonaventura. "ZB-Sicherheitsventil_180821". Technical drawing of the bubbler, received via E-Mail. 2021.

[Fab21]   Luisa Faber. "Entwicklung und Inbetriebnahme eines Gassystems zu Untersuchung einer CBM-TRD Kammer unter Gasfluss". Bachelor's Thesis. 2021.

[Käh21]   Phlipp Kähler. "Private Conversations". Comments on a Draft of this Thesis. 2021.

[Pea21]   PeakTech. *PeakTech Data Logger: Temperature & Humidity 5185 DC-Voltage 5186 K-Type Temperature 5187 Operation Manual.* User manual for the *PeakTech 5185* data logger. 2021.

[Vac22]   Pfeiffer Vacuum. *HiPace 80 with TC 110, DN 63 ISO-K.* Data sheet for HighPace 80 turbopump. Pfeiffer Vacuum. 2022.

[AGa]   First Sensor AG. *CTE7000/CTU7000 Series Miniature pressure transmitters.* E / 11507 / D. First Sensor AG.

[AGb]   First Sensor AG. *The CTE7000 series.* URL: https://www.first-sensor.com/en/products/pressure-sensors/low-pressure-transmitters/cte-ctu7000/. accessed: 18.01.2021.

[Bun]   Physikalisch-Technische Bundesanstalt. *g-Extractor.* Physikalisch-Technische Bundesanstalt. URL: https://www.ptb.de/cms/ptb/fachabteilungen/abt1/fb-11/fb-11-sis/g-extractor.html. accessed 25.10.2021.

[Ley]   Leybold. *What is a leak and how to measure the leak rate in vacuum systems?* Leybold. URL: https://www.leybold.com/en-us/knowledge/vacuum-fundamentals/leak-detection/definition-and-measurement-of-vacuum-leaks. accessed: 11.04.2022.

[Niea]   Patrick Niedenführ. *Der piezoresistive Effekt und die Druckmessung.* First Sensor AG. URL: `https://blog.first-sensor.com/de/piezoresistiver-effekt`. accessed September 2019.

[Nieb]   Patrick Niedenführ. *Unterschied zwischen Absolut-, Relativ- und Differenzdrucksensoren.* First Sensor AG. URL: `https://blog.first-sensor.com/de/druckarten/`. accessed: October 2019.

Acknowledgements

Eigenständigkeitserklärung

Hiermit versichere ich, dass die vorliegende Arbeit über _____

_____ selbstständig von mir und ohne fremde Hilfe verfasst worden ist, dass keine anderen Quellen und Hilfsmittel als die angegebenen benutzt worden sind und dass die Stellen der Arbeit, die anderen Werken – auch elektronischen Medien – dem Wortlaut oder Sinn nach entnommen wurden, auf jeden Fall unter Angabe der Quelle als Entlehnung kenntlich gemacht worden sind. Mir ist bekannt, dass es sich bei einem Plagiat um eine Täuschung handelt, die gemäß der Prüfungsordnung sanktioniert werden kann.

Ich erkläre mich mit einem Abgleich der Arbeit mit anderen Texten zwecks Auffindung von Übereinstimmungen sowie mit einer zu diesem Zweck vorzunehmenden Speicherung der Arbeit in einer Datenbank einverstanden.

Ich versichere, dass ich die vorliegende Arbeit oder Teile daraus nicht anderweitig als Prüfungsarbeit eingereicht habe.

_____
(Datum, Unterschrift)